

A DYNAMIC-IMAGE COMPUTATIONAL APPROACH FOR MODELING THE SPINE

by

Md. Abedul Haque

BS, Bangladesh University of Engineering and Technology, 2005

MS, Bangladesh University of Engineering and Technology, 2008

MS, University of Pittsburgh, 2013

Submitted to the Graduate Faculty of
the Kenneth P. Dietrich School of Arts and Sciences in partial
fulfillment

of the requirements for the degree of

Doctor of Philosophy

University of Pittsburgh

2014

UNIVERSITY OF PITTSBURGH
DIETRICH SCHOOL OF ARTS AND SCIENCE

This dissertation was presented

by

Md. Abedul Haque

It was defended on

April 7th 2014

and approved by

Dr. G. Elisabeta Marai, Computer Science Department, University of Pittsburgh

Dr. Milos Hauskrecht, Computer Science Department, University of Pittsburgh

Dr. Jingtao Wang, Computer Science Department, University of Pittsburgh

Dr. Nancy Pollard, School of Computer Science, Carnegie Mellon University

Dissertation Director: Dr. G. Elisabeta Marai, Computer Science Department, University
of Pittsburgh

Copyright © by Md. Abedul Haque
2014

A DYNAMIC-IMAGE COMPUTATIONAL APPROACH FOR MODELING THE SPINE

Md. Abedul Haque, PhD

University of Pittsburgh, 2014

We propose a dynamic-image driven computational approach for the modeling and simulation of the spine. We use static and dynamic medical images, computational methods and anatomic knowledge to accurately model and measure the subject-specific dynamic behavior of structures in the spine. The resulting models have applications in biomechanical simulations, computer animation, and orthopaedic surgery.

We first develop a semi-automated motion reconstruction method for measuring 3D motion with sub-millimeter accuracy. The automation of the method enables the study of subject-specific spine kinematics over large groups of population. The accuracy of the method enables the modeling and analysis of small anatomical features that are difficult to capture in-vivo using existing imaging techniques. We then develop a set of computational tools to model spine soft-tissue structures. We build dynamic-motion driven geometric models that combine the complementary strengths of the accurate but static models used in orthopaedics and the dynamic but low level-of-detail multibody simulations used in humanoid computer animation. Leveraging dynamic images and reconstructed motion, this approach allows the modeling and analysis anatomical features that are too small to be imaged in-vivo and of their dynamic behavior. Finally, we generate predictive, subject-specific models of healthy and symptomatic spines. The predictive models help to identify, understand and validate hypotheses about spine disorders.

TABLE OF CONTENTS

1.0 INTRODUCTION	1
1.1 Anatomy Background	2
1.2 State of the art in the Spine Modeling	3
1.3 Modeling Challenges	6
1.4 Proposed Approach	7
1.5 Contributions	9
2.0 MOTION RECONSTRUCTION	11
2.1 Related Work	12
2.2 Methods	13
2.2.1 MDRR Generation	15
2.2.2 Image Processing	18
2.2.3 Similarity Metric	18
2.2.4 Hierarchical Optimization	19
2.2.5 Validation	23
2.3 Results	26
2.3.1 Accuracy	27
2.3.2 Robustness	35
2.3.3 Run Time	35
2.4 Discussion	36
2.5 Conclusion	38
3.0 LIGAMENT GEOMETRY MODELING	39
3.1 Related Work	40

3.2	Materials and Methods	42
3.2.1	Data Acquisition and Dynamic Motion Reconstruction	42
3.2.2	Bone Geometry Representations	44
3.2.3	Computing Constrained Ligament Paths	45
3.2.4	Model Analysis	46
3.3	Results and Validation	47
3.3.1	Ligament Length Analysis.	47
3.3.2	Comparative Analysis.	48
3.3.3	Feedback from Domain Experts.	51
3.4	Discussion and Conclusion	53
4.0	CARTILAGE MODELING	56
4.1	Related work	57
4.2	Materials and Methods	58
4.2.1	Data Acquisition	58
4.2.2	Bone Motion Reconstruction	59
4.2.3	Bone Geometry Representations	59
4.2.4	Identifying Cartilage Map	60
4.2.5	Cartilage Modeling and Analysis	63
4.3	Results and Validation	65
4.3.1	Disc Height	65
4.3.2	Disc Deformation	69
4.3.3	Disc Size	71
4.3.4	Validation	71
4.4	Discussion and Conclusion	72
5.0	SPINAL CANAL MODELING	74
5.1	Related Work	75
5.2	Materials and Methods	76
5.2.1	Data Acquisition and Motion Reconstruction	77
5.2.2	Bone Geometry Representations	78
5.2.3	Spinal Canal Geometry Reconstruction	78

5.2.4	Quantitative Analysis	81
5.3	Results	84
5.3.1	Volume analysis	84
5.3.2	Deflection Analysis	84
5.3.3	Spinal Canal Radius Analysis	86
5.3.4	Domain-Expert Feedback	86
5.4	Discussion and Conclusion	87
6.0	CONCLUSION	89
7.0	BIBLIOGRAPHY	93

LIST OF TABLES

1	Experiment data set specification	25
2	Bead-based tracking accuracy (bias and precision). All measurement units are in mm.	26
3	Bias of the hierarchical method and the operator-assisted method. All measurement units are in mm. We did not find any statistical significant difference in bias ($p > 0.01$) for any bone along any axis direction between the hierarchical and the operator-assisted method.	27
4	Precision of the hierarchical method and the operator-assisted method. All measurement units are in mm. We did not find any statistical significant difference ($p > 0.01$) in precision between the hierarchical and the operator-assisted method for any bone in any coordinate system direction.	29
5	Root-mean-squared error of the hierarchical method and the operator-assisted method. All measurement units are in mm. We did not find any statistical significant difference ($p > 0.01$) in rms error between the hierarchical and the operator-assisted method for any bone in any coordinate system direction. . .	30
6	Maximum error of the Hierarchical method and the operator-assisted method. All measurement units are in mm.	32
7	Translational (anatomical coordinates) bias and precision of the hierarchical method and the operator-assisted method. All measurement units are in mm. There was no statistically significant difference (Hotteling's T-Squared, $p > 0.01$) in bias and precision between the hierarchical and the operator-assisted method.	33

8	Rotational (anatomical coordinates) bias and precision of the hierarchical method and the operator-assisted method. All measurement units are in degrees. There was no statistically significant difference (Hotteling's T-Squared, $p > 0.01$) in bias and precision between the hierarchical and the operator-assisted method.	33
9	Average neutral ligament length computed from the mesh models against <i>in vitro</i> results from medical literature[76].	48
10	PLL mesh model comparison (normalized length and deflection variation) between the fusion and healthy datasets.	48
11	Disc height measurements from a cadaver study reported by Lu et. al. [42]	64
12	Disc height measurements from our reconstructed point cloud models.	65
13	Normalized disc height variation across motion. We noticed that the discs in the fusion subject goes through a greater range of height variation than the discs in the control subject specially in the posterior region and the C4-C5 disc shows greater difference than the other discs.	68
14	Maximum disc deformation with respect to the minimum height disc.	70
15	Normalized maximum disc deformation w.r.t. the minimum height disc	70
16	Disc diameters from our models in the lateral and anterior-posterior direction. The lateral diameter is greater than the anterior-posterior diameter for all C3-C7 segments.	71
17	Spinal canal volume in the cervical spine (C3-C7) for the healthy and the fusion subject (not normalized). The change in volume is due to subject variation. .	82
18	Normalized volume changes for the spinal canal segments. The subjects show different patterns due to the fusion surgery: The fusion subject has significantly lower volume change in C5-C6 region than the healthy patient. The analysis indicates that in the fusion subject the segments adjacent to C5-C6 are compensating for this difference.	82

LIST OF FIGURES

1	The proposed dynamic-image based approach for subject-specific modeling of the spine. We first reconstruct spine kinematics from captured dynamic images. Next, we infer the soft tissue geometry from bone models, dynamic motion information and anatomic knowledge. Finally, we perform analysis on the bone and the dynamic soft-tissue models.	8
2	Model-based tracking method for the spine. The method uses a three step process: 2D projection, image processing, and optimization. The process is repeated for all frames of a motion sequence.	15
3	Single-bone projection of C4 (a) and multi-bone projection of C4 (c). Notice how the presence of C3 and C5 (b) changes the signature of C4 (in (c)) in the adjacent region.	16
4	X-ray image processing for both cameras of a random trial. (a) Raw images. (b) Gaussian-filtered images. (c) Gaussian and Sobel filtered images. (d) Gaussian, Sobel and weighted averaged images. Snapshots (c) and (d) have been contrast-enhanced for printing purposes.	17
5	The local (a) and anatomical (b) coordinate systems defined for a vertebra	20
6	A conceptual 2D diagram of phase 1. r_1 and r_2 represent the bone in the previous two solved frames. p is the predicted point for current frame. Intermediate circles represent the additional intermediate points. The circle within the diamond represents the selected seed point. The cross points represent the surrounding regions which are going to be searched in the next phases.	21

7	System configuration of the bi-plane X-ray setup for cervical spine trials (a) and the schematic diagram of the setup (b). X-ray sources direct X-rays through the subject to image intensifiers.	23
8	Bias of the hierarchical method and the operator-assisted method. X, Y and Z denote the axes of comparison. We did not find any statistically significant difference ($p > 0.01$) in bias between the hierarchical and the operator-assisted methods for any bone along any axis direction. However, note that the bias for C5 and C6 is relatively higher than the bias for C3, C4 and C7 due to the hardware implant in C5 and C6. Still, the hierarchical multi-bone method has achieved sub-millimeter accuracy for C5 and C6 (max bias 0.62 mm) along with the other vertebrae. Results are averaged over 13 trials from 3 subjects, 60 ~ 100 frames per trial.	28
9	Precision for the hierarchical and the operator-assisted single-bone method. X, Y and Z denote the axes of comparison. We did not find any statistical significant difference ($p > 0.01$) in precision between the hierarchical and the operator-assisted method for any bone in any coordinate system direction. Results are averaged over 13 trials from 3 subjects, 60 ~ 100 frames per trial.	30
10	Root-mean-squared error (mm) for the hierarchical and the operator-assisted single-bone method. X, Y and Z denote the axes of comparison. We did not find any statistical significant difference ($p > 0.01$) in rms error between the hierarchical and the operator-assisted method for any bone in any coordinate system direction. Results are averaged over 13 trials from 3 subjects, 60 ~ 100 frames per trial.	31
11	Maximum error for the hierarchical and the operator-assisted single-bone method. X, Y and Z denote the axes of comparison. The automated hierarchical method is as accurate as the operator-assisted method. Please note that relatively higher values of maximum error (compared to rms error, bias and precision) indicate the presence of some outliers X-ray frames with poorer image quality than most other frames of a motion sequence. Results are summarized over 13 trials from 3 subjects, 60 ~ 100 frames per trial.	31

12	Comparison of tracking results between the single-bone method without operator assistance (top row) against the hierarchical approach without operator assistance (bottom row). In each row, the two camera views are shown, with the vertebra (green) superimposed on the X-ray image (red); dotted lines show the target location of the vertebra. Note the single-bone solution is off-track, while the hierarchical one is on target.	34
13	(a) Pipeline of the ligament modeling method. We compute dynamic motion information of vertebrae from 3D volume images and 2D dynamic radiographs. We select ligament insertion sites manually. We then compute constrained ligament meshes across motion using the bone geometry and the dynamic motion information. Finally, we compute features of the ligament geometry by analyzing the constrained geometries across motion. (b) Reconstructed Anterior Longitudinal Ligament (ALL) and Posterior Longitudinal Ligament (PLL) meshes of a subject.	41
14	Two frames of the high resolution (1024x1024) radiograph sequences which are captured during motion from the dynamic stereo X-ray system.	43
15	(a) The explicit mesh representation of the bone. (b) A 2D crosscut through the distance field representation. Red indicates points outside the bone surface and blue indicates points inside the bone surface. The distance from the surface is mapped to the color saturation level. (c) Visualization of the inter-bone joint space computed using the distance-field information; darker colors indicate shorter distance between the two adjacent bone surfaces.	44
16	Normalized length analyses across the dynamic motion range(from full extension to full flexion) for each segment of the spinal posterior ligament band for a fusion and a healthy subject. C5-C6 shows the most significant change in the length variation across the motion (c). Other segments of the spine compensate for the fusion.	49

17	Maximum deflection analyses across the dynamic motion range(from full extension to full flexion) for each segment of the spinal canal for a fusion and a healthy subject. Because of the fusion, C5-C6 ligament segment shows significant difference in the deflection. Deflection differences for the other segments are not significant.	50
18	In our model ligament fibers do not bundle together during motion indicating minimum interaction longitudinally among fibers.	52
19	Manually marked initialization region for the cartilage map location of a vertebra (a). An intervertebral disc is located between the superior and inferior cartilage region (b).	60
20	A manually marked region (Fig. 19) is filtered automatically using the joint space distance between two vertebrae. The resulting filtered point set for a single frame (a) denotes the region where the distance between the two bones are within a certain threshold. The union of filtered points from all frames approximates the final cartilage map location (b).	61
21	Reconstructed surface model of the minimum height disc space from the fusion patient. The image shows models of the C3-C4, C4-C5 and C6-C7 segments. C5-C6 segment is excluded due to the fusion surgery.	62
22	A reconstructed minimum height disc (a) in the joint space of two vertebrae. A minimum height disc color-mapped with the disc deformation (b).	64
23	Disc height measurements for the control subject ((a), (c) and (e)) and the fusion subject ((b), (d) and (f)). The first and the last frame corresponds to full extension and full flexion.	66
24	Normalized disc height measurements (in percentage w.r.t. to the neutral height) for the control subject ((a), (c) and (e)) and the fusion subject ((b), (d) and (f)). The first and the last frame corresponds to full extension and full flexion.	67

25	Disc deformation with respect to the minimum height disc colormapped on the minimum height disc for the control (a) and the fusion subject(b). Gray to red represents low to high deformation. From top to bottom, we show C3-C4, C4-C5 and the C6-C7 joint discs. From left to right, we show the colormapped disc in the full extension, neutral and the full flexion posture. For each disc, the lower part corresponds to the anterior and the upper part corresponds to the posterior region.	69
26	The spinal foramen region (marked in black) and the automatically placed landmarks within it.	76
27	The reconstructed spinal canal meshes at two extreme rotations of the neck—full flexion (a) and full extension (b)—during the captured motion sequence. To avoid visual clutter we only show three vertebrae—C3,C5 and C7.	79
28	Normalized volume analyses across the dynamic motion range(from full extension to full flexion) for each segment of the spinal canal for a fusion and a healthy subject. C5-C6 is the least changing volume segment in the fusion patient(a). In contrast, C5-C6 is the most changing segment in the healthy patient (b). Other spinal canal segments of the two subjects are affected differently by the motion.	83
29	The difference in the deflection region for the two subjects' spinal canals. For the fusion subject (a), the canal bends towards the top of the spinal column and for the healthy subject (b), the canal bends towards the middle of the spinal column. The change in the spinal canal radius is mapped to the hue (from blue to red; blue for increase and red for decrease in radius) on the canal surface.	85

1.0 INTRODUCTION

In the USA, back and neck pain are among the major causes of disability and high healthcare costs. In 2005, there were over 575,000 spine surgery discharges from US hospitals [55]. The direct and indirect cost of back disorders amount to billions annually. Despite the high socio-economic impact of spine diseases and the rapid rise in spine surgeries, the underlying causes of many of these conditions are not well understood. For example, disc degenerative changes due to aging are the most common diagnosis in patients with low back pain. We do not know, however, why these changes affect only a segment of population. We also do not know how these changes alter spine dynamics and why the same treatment has different outcomes for different patients. Subject-specific accurate modeling and simulation of the spine can help advance our knowledge in this respect.

Anatomically accurate modeling of the spine can help researchers and clinicians to understand the motion dynamics and to identify the actual causes of many spine related conditions. However, building such dynamic models poses significant challenges - for example, automated computing of the dynamic motion of the spine is necessary for automated dynamic modeling and analysis of the spine. However, building an automated and non-invasive method for computing 3D dynamic motion is a significant challenge for the spine due to its complex structure. Modeling a complex system like the spine also requires modeling constituent structures some of which may not be directly observable from medical images. For example, 3D dynamic geometry of small anatomical structures such as ligaments cannot be measured with the existing imaging techniques. As a result, to date, we do not have a subject-specific dynamic modeling technique for the spine that would include skeletal soft-tissues such as ligaments and cartilage.

The goal of this research is to develop a computing approach for subject-specific dynamic

modeling of the spine. The strength of our approach is that we capture medical images with static geometry and dynamic motion information and combine them to infer unobservable features of the joints. A combination of multimodal imaging, computational tools and geometric modeling techniques leads to a novel approach for accurate modeling of the spine. This approach serves as a significant advancement in biodynamic and orthopedics research too. Furthermore, these models can also be used in computer animation for generating realistic motion, in robotics and orthopedic implant design.

1.1 ANATOMY BACKGROUND

The basic musculoskeletal structure of the spine has four components: 1. muscles 2. ligaments 3. inter-vertebral discs (cartilage) and 4. bones. In addition, the spine contains the spinal cord. Muscles apply forces on the vertebrae. A combination of forces from different muscle groups makes complex spine movement possible. Ligaments are tough, passive bands of soft-tissue structures which tether bones together, restrict joint motion and stabilize the joint. The vertebrae are the hard elements of the spine, providing the load bearing capability. They also protect the spinal cord. The inter-vertebral discs are located between adjacent vertebral bodies and form a viscoelastic cushion. For understanding spine dynamics, dynamic modeling and analysis of spine musculoskeletal structures is essential because of their direct impact on joint functionalities and stability.

Muscles control the movement and the balance of the spine. Spinal muscles are attached to different vertebrae and to arms, legs, the head, the rib cage and the pelvis. Movements of the spine include flexion and extension (forward and back bending), lateral (left and right side) bending, and rotation (twisting). Muscle fibers are connected with bones through tendons. Muscles apply active and passive forces on bones through contraction and extension.

The ligaments of the spine tether the vertebrae together and provide support for the entire column. The spine has five ligaments: 1. Anterior longitudinal ligament 2. Posterior longitudinal ligament 3. Ligamentum flavum 4. Interspinous ligament and 5. Supraspinous ligament. The main ligaments are the anterior and the posterior longitudinal ligaments.

They run along the front (anterior) and the back (posterior) of the spinal column. Different ligaments play different roles in spine dynamics. These ligaments have different geometric and material properties and these properties vary between individuals. Accurate estimation of these properties without invasive dissection of the spine is practically impossible; this makes subject-specific modeling of the spine ligaments an extremely challenging problem.

The inter-vertebral discs are soft tissue structures situated between adjacent vertebral bodies. The size and shape of the inter-vertebral discs vary with the spinal level. The inter-vertebral disc act as a cushion and shock absorber between joint bones. The discs are susceptible degenerative disc disease which is considered to be one of the main reasons of back pain.

The spinal cord is the conduction pathway for nerve impulses between the brain and the rest of the body. Unlike the other soft tissue structures, the spinal cord does not have any mechanical role in the spine dynamics. The spinal cord is protected by the vertebral foramen and several layers of soft-tissues. However, it is still vulnerable to injury from disc bulging or swelling causing severe pain and other neurological conditions. Accurate modeling of the spinal canal is critical to understanding many spine related conditions and neurological disorders.

The spine comprises 24 vertebrae. They are divided into four regions: 1. cervical 2. thoracic 3. lumbar and 4. sacral. The cervical region has seven vertebrae, providing the maximum flexibility and range of motion for the head. The twelve thoracic vertebrae support ribs and the organs that hang from them. The lumbar region consists of the five largest and strongest vertebrae. These lumbar vertebrae are subjected to the highest forces and moments of the spine. The sacrum attaches the spine to the bones of pelvis.

1.2 STATE OF THE ART IN THE SPINE MODELING

Existing computer aided spine modeling approaches can be broadly classified in two categories based on model representation techniques: 1. finite element approach (FE) and 2. multibody system approach.

The finite element approach allows creating highly detailed, sophisticated and accurate models by dividing a complex structure into many small and simpler elements. However, the model complexity increases rapidly as new heterogeneous structures are added - eventually leading to a computationally infeasible to simulate model. The finite element method (FEM), originally developed for stress analyses in engineering mechanics, was introduced to biomechanics in 1972 by Brekelmans et. al. [13]. Since then FEM has been used extensively for modeling and analysis of bones, soft-tissue structures and complex articulations. Liu et. al. [40] first used the FEM for the spine modeling. A linear solution technique is generally used for small-strain simulations of a single vertebral body [37, 68]. For large-scale multisegmental simulations, nonlinear FE methods are used [14, 17]. The FE method has also been used to study the role of soft-tissues [76, 64] and implants [59] on the spine biomechanics.

The FE method is extensively used for joint modeling and simulations. However there are a few significant challenges for subject-specific modeling and simulation of articulations using the FE method. First, creating accurate geometric models requires estimating many parameters; this makes the process extremely cumbersome and time consuming. Generic structures and parameters are therefore used to build FE models. Second, significant geometric changes can happen to joint soft-tissues during a whole range of motion of an articulation. It is difficult to simulate this behavior with FE models due to their fixed geometric structures.

Two major steps for the finite element modeling are the geometry extraction and the material properties formulation. For the bone geometry, the most flexible and common source is subject-specific medical imaging, typically computed tomography (CT). For the soft-tissue geometry, automated methods are often used to infer simplified models based on joint bone models. Detailed and accurate models of the soft-tissue geometry can be created directly from the structure after invasively dissecting the articulation. Material properties are chosen either from existing literature which leads to a generic model or directly by dissecting and experimenting on an articulation which leads to a subject-specific model.

The FE modeling approach can be complementary to the soft-tissue modeling techniques that we will present in this dissertation. Our automated tools for geometrical modeling of the soft-tissues can provide the FE method with the required high accuracy geometric models

which would be challenging to construct manually for the FE method .

In the FE method, individual components of an articulation such as ligaments, bones and cartilages are modeled with fine details leading to a very complex model with even just a few components. In multibody system models, on the other hand, articulation components have much simpler representations such as a bone as a single rigid-body and a ligament as a single elastic fiber. Therefore, a large number of components can be added in the articulation model without making it too complex. Several multibody dynamics based software such as OpenSIMM [20] and AnyBody [19] have been specially designed for modeling biological systems and have gained wide popularity in recent years.

As mentioned above, in multibody system models, bones are modeled as rigid bodies. the bone geometry is usually extracted from volumetric images such as CT and MRI. Soft-tissue such as muscle and ligament geometries can be as simple as a one-dimensional line segment indicating the line of action or a piecewise linear curve with or without constraints [3]. To model the mechanical aspects of soft-tissues, several models [32, 71, 77] exist in the literature. Building multibody system models for the spine is time consuming due to the manual approach of modeling muscles and ligaments and the process requires significant expertise. Therefore, many studies take an existing generic model and modify it to acquire a subject-specific model. One common approach is scaling the generic model [63] based on external markers used during the motion capture.

Spine musculoskeletal models [18, 25] have been used to analyze the role of different muscle groups in spine motion and to simulate surgeries that affect the spinal musculature [25]. Generic models [18, 67, 78] are often built to enable further research with the models. Some models are built to analyze muscle activations for specific motion patterns such as standing or seated posture [21, 36].

However, lack of geometric details in representing soft-tissue structures is a major limitation for multibody system models. Geometrically accurate dynamic modeling of the soft-tissue structures can lead to a better understanding of how these soft-tissues deform during motion and influence the joint motion dynamics. To the best of our knowledge, no existing multibody system includes dynamic models of the cartilage or inter-vertebral discs. Ligaments - if included at all - have simplified geometric representation e.g. one-dimensional

linear segment or by a piecewise linear curve with a fixed geometric structure [3]. Muscles also have simplified geometric structures similar to ligaments. Accurate geometric representations of the soft-tissue during motion can elucidate many spine related injuries and diseases.

1.3 MODELING CHALLENGES

Subject-specific dynamic modeling of the spine poses several significant challenges. One of the challenges is to capture the dynamic behavior of the spine both for the soft and hard tissue structures. The task is more challenging for the soft-tissue structures because the soft-tissues deform during motion. Existing state of the 3D motion capture systems are often not accurate enough for detailed modeling purpose or require extensive manual labor for the motion reconstruction. An automated in-vivo method for capturing the 3D dynamic motion is a significant challenge for spine modeling.

Modeling the soft-tissue geometry of the spine is another challenge. The spine soft-tissue structures are complex and intricately surrounded by vertebrae and other soft-tissue structures. With the current imaging techniques some of the structures such as the ligaments are extremely difficult to capture. Limited resolution and high noise level make the geometric reconstruction extremely difficult. Furthermore current in-vivo 3D images such as MR and CT can capture the geometry only in a static posture. Therefore reconstructing subject-specific dynamic geometry of the soft-tissue structures from captured medical images is a significant challenge for spine modeling.

Automation is a key requirement for the overall modeling process. Automation will enable subject-specific large scale studies. However, existing state of the art subject-specific dynamic modeling techniques require significant manual labor making the modeling process impractical for medium to large scale studies. Achieving complete automation or restricting the manual intervention to a minimum level while maintaining the accuracy is another challenge for the spine modeling.

Another fundamental challenge is choosing anatomically relevant modeling elements

while keeping the models simple and computationally efficient. As we increase the modeling level of details, the complexity and the number of unknown parameters of the model also increase, making the model building and simulation infeasible. Simplifying assumptions such as representing bones as rigid bodies are necessary to keep the modeling process efficient and practical.

Designing anatomically relevant measurements for validation and comparison of models is another challenge for this research. Because the musculoskeletal structures of the spine can vary significantly between individuals, anatomically relevant normalized measurements are often necessary for inter-subject comparison of the models.

1.4 PROPOSED APPROACH

We propose a dynamic-image based approach for subject-specific modeling of the spine. We advance the state of the art spine modeling techniques by including dynamic soft-tissue structures such as ligaments and inter-vertebral discs despite the limitations of existing 3D imaging techniques. We show that the resulting models are adaptable, anatomically accurate and have predictive capabilities.

The key idea behind our approach is to use multi-modal medical images with complementary motion and geometry information to automatically reconstruct deformable soft-tissue geometry. We develop automated and semi-automated tools based on 3D static and 2D dynamic images to model the soft-tissue geometry of the spine whereas the state of the art modeling techniques are mainly static or manual. First, we develop an automated method to reconstruct accurate 3D motion of the vertebrae. The idea is using the motion information along with the 3D bone models and anatomy-book knowledge to reconstruct the soft-tissue geometry and dynamic behavior. Then we assemble the 3D vertebral models and the reconstructed soft-tissue models to visualize and analyze the dynamic behavior of the spine.

Figure 1 shows the three basic stages of our approach: 1. dynamic motion reconstruction 2. soft-tissue modeling and 3. model analysis. We use dynamic radiographs to capture

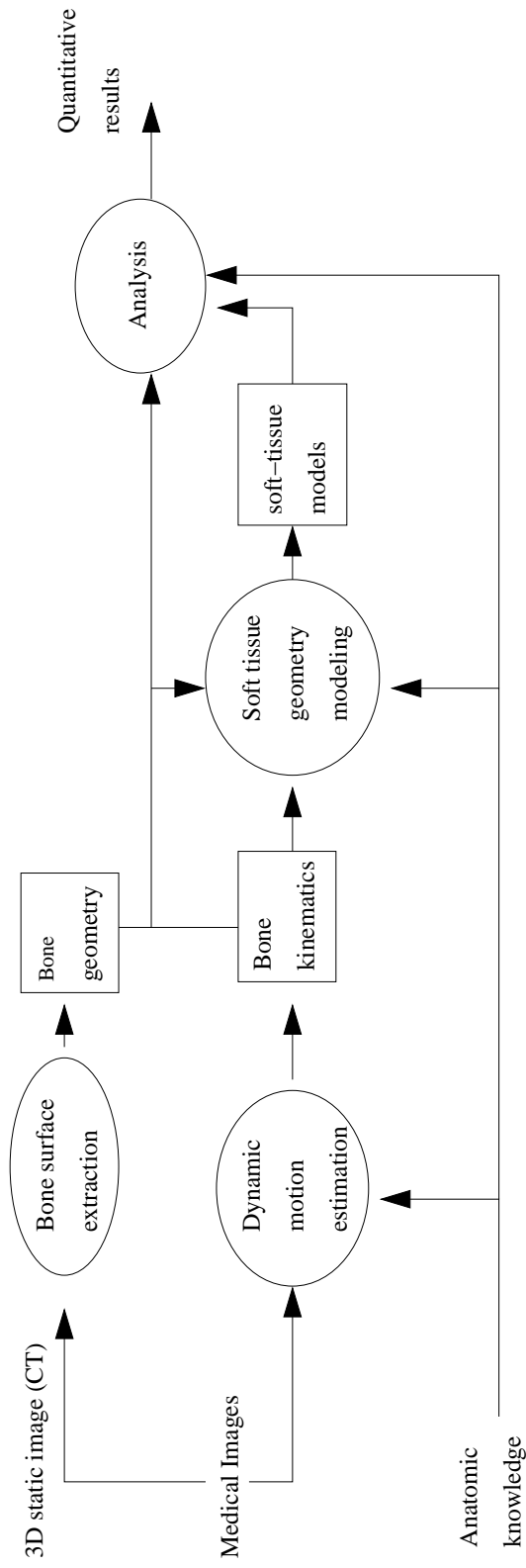


Figure 1: The proposed dynamic-image based approach for subject-specific modeling of the spine. We first reconstruct spine kinematics from captured dynamic images. Next, we infer the soft tissue geometry from bone models, dynamic motion information and anatomic knowledge. Finally, we perform analysis on the bone and the dynamic soft-tissue models.

motion information and CT images to capture the bone geometry. 2D radiographs capture the spine movement during motion and CT images capture the 3D structure of vertebrae in a static posture. Even though MRIs can also capture the 3D structure of bones, we use CT images due to the higher resolution and better quality.

We reconstruct dynamic motion of vertebrae automatically from the x-ray images. In order to compute the accurate 3D dynamic motion, we develop a hierarchical model-based approach where 3D bone models extracted from CT scan images are registered to 2D dynamic x-ray images using a 2D-3D registration technique (chapter 2). Accuracy and automation are the most important goals for motion reconstruction. Inaccurate motion information can cause inter-bone penetration or can influence the joint space measurements causing erroneous estimation of joint space soft-tissues such as inter-vertebral discs and ligaments. The automation keeps the accuracy of the process operator-independent and reduces manual labor for the overall modeling task.

Next we reconstruct the soft-tissue structures of the spine. In this study, we do not model spine muscles because of their complexity in connection to other skeletal structures. We reconstruct ligaments (chapter 3), inter-vertebral discs (chapter 4) and the spinal canal (chapter 5). We make necessary simplifying assumptions to keep the modeling process efficient while maintaining the accuracy. In each chapter we show the effectiveness of the reconstructed models and present quantitative analyses to explain the difference in the symptomatic and asymptomatic spine behavior.

1.5 CONTRIBUTIONS

The principal contribution of this research is an image-based computational approach for subject-specific dynamic modeling of the spine. This approach will advance the state of the art spine modeling techniques in terms of automation, accuracy and modeling level of details while keeping the model still efficient to simulate.

The second contribution is an automated method for reconstructing 3D motion of the spine with sub-millimeter accuracy in live individuals. The automation of the method enables

large scale studies for better understanding of spine kinematics.

The third contribution is a generic approach for subject-specific geometric modeling of the spine soft-tissue structures such as ligaments, inter-vertebral discs and the spinal cord. Our developed methods enable us to address the existing medical imaging limitation for capturing dynamic 3D structure of soft-tissues.

The fourth contribution is the design of anatomically relevant measurements based on the dynamic spine model for inter-subject comparative analysis and validation.

Finally, the developed tools through the resulting models and comparative analysis will serve to advance the study of pathology and injuries related to the spine.

2.0 MOTION RECONSTRUCTION

Motion reconstruction is the first step of the proposed spine modeling method. Accurate, automatic and 3D in-vivo motion reconstruction of the spine is extremely challenging. Many existing motion tracking methods for other joints cannot maintain similar accuracy for the spine due to the joint complexity.

Model-based methods have been developed to measure 3D bone motion with high accuracy at knee or shoulder joints [11, 5]; such methods employ 3D models of the bones, which they track through a sequence of dynamic x-ray images. Model-based methods are more accurate than skin marker-based methods, which suffer from errors as large as 10 mm in translation and 8° in rotation [33]. They can also capture dynamic motion, unlike existing three-dimensional techniques such as Computed Tomography (CT, which also features higher radiation exposure, depending on the anatomic location) or Magnetic Resonance Imaging (MRI). Finally, unlike dynamic three-dimensional techniques (Cine-PC MRI [10]), model-based methods do not require continuous movement for long periods of time during data collection, support in general large ranges of motion, and pose fewer restrictions during imaging, thus leading to loadings more similar to most everyday movements. Given the advantages of model-based tracking, systems implementing model-based methods are utilized in various forms at several different academic institutions and medical research centers; the basic imaging hardware required for biplane radiography setup costs less than one third of what a modern 3T MRI scanner costs.

However, existing implementations of 3D model-based tracking methods suffer from the same critical issues. The existing tracking processes are extremely labor-intensive, requiring many (up to 30 for the spine) hours of labor for every hour spent collecting data. Furthermore, a high level of expertise is required to generate trustworthy results. For this reason

the tracking task cannot be reliably delegated to a crowd-sourcing approach such as the mechanical turk. Accuracy and reliability, especially for the more automated algorithms, are inconsistent. Simultaneous acquisition of a pair of radiographic images is a prerequisite for all systems claiming high 3D accuracy, but this requirement creates significant image quality problems due to scatter radiation (a widely known issue for biplane radiographic imaging, which can become intractable for imaging the thicker parts of the body such as hips or the lumbar spine). It is also often difficult or impossible to obtain two radiographic views that avoid bone overlap in the images, which also degrades imaging matching performance using conventional tracking approaches. Surgically inserted hardware further decreases tracking accuracy and robustness. These limitations have thus far limited application of this technology to research studies, since the time and cost for data analysis is prohibitive for clinical use.

In this chapter, we propose and validate an *automated* intelligent, hierarchical model-based method to track spine motion from dynamic biplane radiographs. The specific goal of this work is automation while matching the accuracy of human expert operators.

2.1 RELATED WORK

Several marker-based methods have been developed to estimate 3D bone kinematics, both non-invasive (skin mounted markers [43]) and invasive. However, external markers suffer from errors as large as 10 mm in translation and 8° in rotation [33].

Existing three-dimensional techniques, such as Computed Tomography (CT) and Magnetic Resonance Imaging (MRI), allow assessing movement of the underlying bone directly [47, 62]. These methods can produce very accurate results. However, CT is unable to capture dynamic motion; also CT radiation exposure is high, which may become an issue depending on the anatomic location. In contrast, Cine-PC MRI [10] can capture dynamic motion. However, it can only support limited ranges of motion and the subject is required to perform the movement continuously for long periods of time while data is being collected. Furthermore, due to the restrictions imposed by the imaging environment, the loading that

occurs during data collection is different from most every day movements.

Unlike CT and MRI, single-plane radiograph-based techniques [9, 51] can capture dynamic motion with a high frame rate. However, this method cannot produce 3D motion accurately. Typically, motion is kept within a plane perpendicular to the direction of camera projection. A study on knee implant tracking [44] reported out of plane translation errors greater than 3 mm despite the fact that the movement was mainly in plane.

Biplane or stereo radiographic imaging enables accurate quantitative 3D motion assessment for both static [5] and dynamic bone motion analysis. Bone location and orientation can be precisely measured by beads (Radiostereometric analysis or RSA) implanted into the bones [6] or by matching the 2D projection (Digitally Reconstructed Radiograph or DRR) of a reconstructed bone model to the radiographic images [5]. Bead-based tracking has shown good accuracy and has been used to produce ground truth to validate other tracking methods [5, 6].

While the model-based tracking from stereographic images has the advantage of non-invasiveness (unlike bead-based tracking), the approach requires extensive human operator intervention. For the cervical spine, as many as 30 hours of labor are required for each hour spent collecting the data, leading to approximately one week of labor per human subject processed (considering 6 trials per subject). Furthermore, a high level of expertise is required to generate trustworthy results on data for which no ground-truth is available. For this reason the tracking task cannot be reliably delegated to a crowd-sourcing approach such as the mechanical turk. This lack of automation makes the existing model-based methods unsuitable for practical clinical application.

2.2 METHODS

The basic premise for tracking bone motion is a model-based tracking approach that matches radiographic images to a known bone shape. 3D models of the bones of interest are obtained using conventional imaging (CT or MRI scans). A virtual model of the stereo-radiographic imaging system is generated using the precise locations of the radiographic sources and image

detectors (which can be determined automatically by imaging a calibration object of known dimensions). Simulated x-rays are passed through the bone model to produce a pair of digitally reconstructed radiographs (DRRs) on the image plane. By manipulating the bone model within the virtual radiographic system, pairs of DRRs can be generated for any bone position. By calculating image similarity measures between the actual radiographic image pairs and the DRRs, the virtual bone position and orientation can be adjusted (manually or by an optimization algorithm) to identify the position that provides the greatest match, thus determining the position of the actual bone in space. This process is repeated for each pair of the images in the motion sequence, and repeated again for each bone of interest to yield the 3D position of the joint for the entire movement.

In conventional model-based tracking, the presence of overlapping bones (a common occurrence for the spine) reduces the quality of image matching and degrades tracking performance. Also, tracking each bone independently ignores the known characteristics of joints that constrain the relative bone movements. We introduce a hierarchical multi-bone model approach, in which multiple bones are combined in a single 2D projection and simultaneously matched with the radiograph images. This approach takes advantage of the rich detail present in regions of radiographic bone overlap, which can therefore enhance, rather than degrade, tracking performance. By incorporating hierarchical, anatomically aware, multi-articular models of joints, as well as temporal coherence, tracking reliability can be further enhanced by exploiting known constraints that are defined across space and time.

The method uses a new digitally reconstructed radiograph generation procedure (MDRR), a standard image processing step, and a novel hierarchical optimization procedure. For each X-ray frame in the motion sequence, a 2D projection (MDRR) is generated from the multiple reconstructed bone models. Next, both the X-ray and the 2D projection images are processed to reduce noise and enhance edges. Finally, an optimization method searches through different positions and orientations of the bone models to find the best match between the MDRR and the X-ray image. The process is repeated for all frames of a motion sequence (Fig. 2).

While a variety of imaging hardware setups can be used in practice to acquire dynamic radiograph images, for our experiments high-resolution X-ray images were captured using a

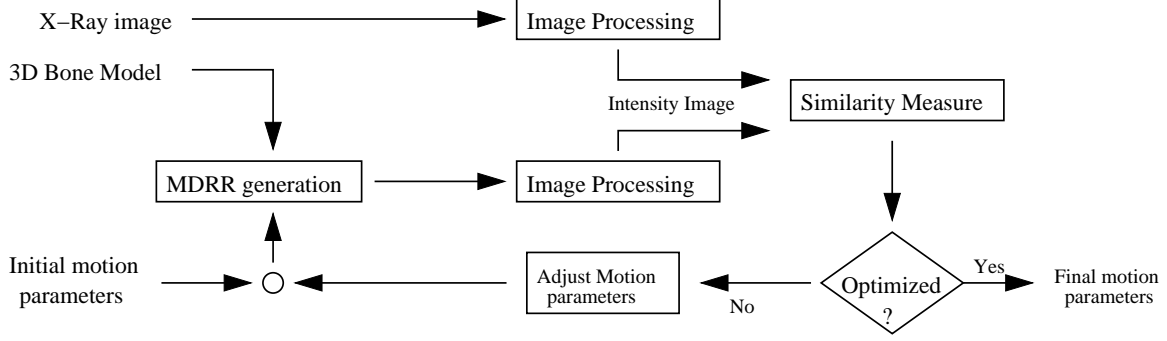


Figure 2: Model-based tracking method for the spine. The method uses a three step process: 2D projection, image processing, and optimization. The process is repeated for all frames of a motion sequence.

dynamic stereo X-ray (DSX) system, and 3D volumetric images of the bones of interest were acquired with a high-resolution static computed tomography scanner (see subsection 2.2.5).

2.2.1 MDRR Generation

Model-based tracking [5] is based on the idea that an X-ray image can be computationally produced using a simplified X-ray generation model [73]:

$$I(\mathbf{p}) = \int_L \mu(r) dr \quad (2.1)$$

where $I(\mathbf{p})$ is the intensity of the X-ray detector pixel \mathbf{p} , $\mu(r)$ is the X-ray attenuation coefficient, and L is the projection beam from source to point \mathbf{p} . This model assumes that the X-ray system corrects for beam divergence and that the sensors have logarithmic response.

$I(\mathbf{p})$ can be estimated using ray casting of the CT image and the resulting image is known as the Digitally Reconstructed Radiograph (DRR). The segmented CT image serves directly as the 3D bone model.

However, in reality the intensity of a pixel $I(\mathbf{p})$ not only depends on the bone of interest, but also on any other structure the beam L passes through. Thus, $I(\mathbf{p})$ can be thought of as integration of contributions from several different sources:

$$\begin{aligned}
I(\mathbf{p}) = & I_c(\text{bone of interest}) + I_c(\text{neighboring bones}) \\
& [+I_c(\text{metallic implants}) + I_c(\text{other bones})] \\
& [+I_c(\text{soft tissue}) + I_c(\text{random noise})]
\end{aligned} \tag{2.2}$$

where $I_c(O)$ represents contribution to pixel (x, y) due to object O .

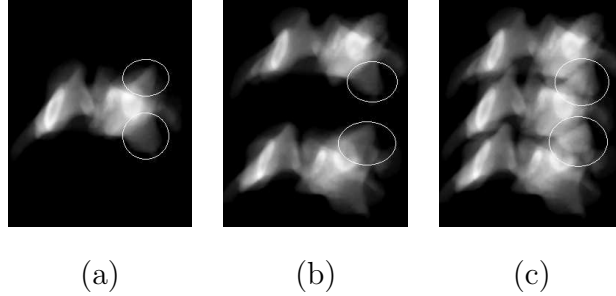


Figure 3: Single-bone projection of C4 (a) and multi-bone projection of C4 (c). Notice how the presence of C3 and C5 (b) changes the signature of C4 (in (c)) in the adjacent region.

Existing conventional bone-tracking methods assume that the contribution to a pixel intensity from all the sources except the bone itself is negligible or constant [5]. This assumption does not hold for spine data (and other joints) where neighboring bones and implants overlap significantly. A single-bone DRR (SDRR) is nonetheless generated using only the model of the bone being tracked, and accounts only for the first term, $I_c(\text{bone of interest})$.

To account for contributions from neighboring bones and surgical implants, we propose the following model for multi-bone DRR (MDRR) generation:

$$\begin{aligned}
I_{MDRR}(\mathbf{p}) = & I_c(\text{bone of interest}) + I_c(\text{neighboring bones}) \\
& + I_c(\text{metallic implants})
\end{aligned} \tag{2.3}$$

In this approximation, it is assumed that contribution due to non-neighboring bones (e.g. shoulder, skull) can usually be avoided by careful positioning of X-ray sources and detectors. Any contribution due to soft tissue and random noise is assumed negligible here. Although still an approximation, the resulting MDRRs have a more realistic signature in adjacent regions than the SDRRs (Fig. 3).

We use ray-casting volume rendering through multiple neighboring bones to generate MDRRs. On a single 2.0 GHz processor, each MDRR generation requires on average 100ms. However, during bone position and orientation optimization more than 500 MDRRs may need to be generated for each motion frame. A sequential implementation would require approximately 6 hours of computation time to track 6 vertebrae over 60 frames. To reduce the computation time, we use a parallel implementation of the MDRR generation process.

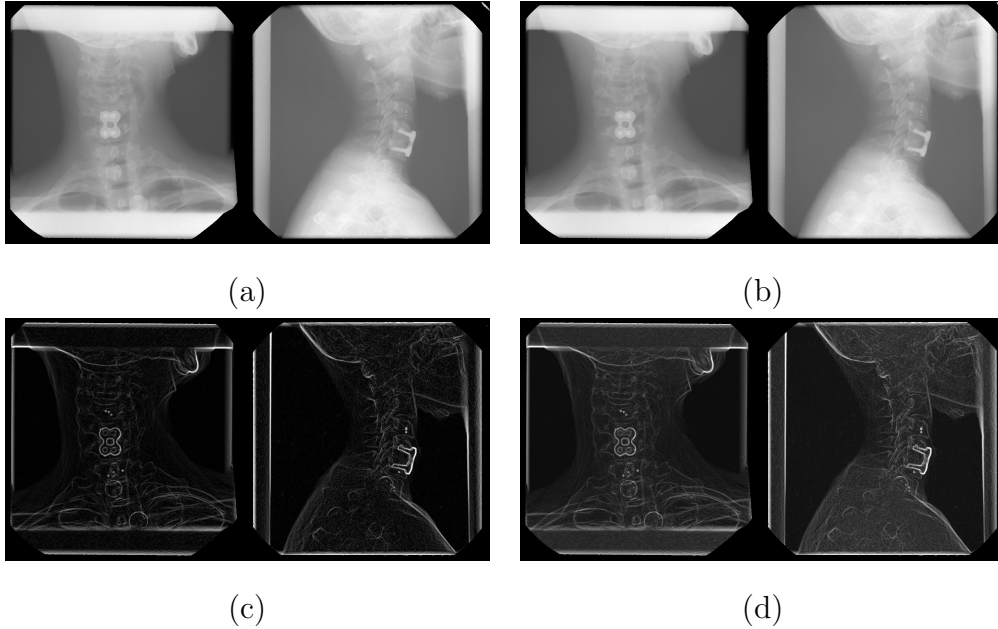


Figure 4: X-ray image processing for both cameras of a random trial. (a) Raw images. (b) Gaussian-filtered images. (c) Gaussian and Sobel filtered images. (d) Gaussian, Sobel and weighted averaged images. Snapshots (c) and (d) have been contrast-enhanced for printing purposes.

2.2.2 Image Processing

The image processing steps and the similarity metric are similar to earlier studies [11, 5] enabling us to isolate and investigate the effect of MDRRs and hierarchical optimization. The MDRRs and the X-ray images are passed through several standard image processing steps to reduce noise and enhance edges of the images. Summarizing [11], a 3x3 discrete Gaussian filter is first applied to reduce noise (Fig. 4a and b), then a 3x3 Sobel filter is applied to extract edges (Fig. 4c) from the smoothed images. Finally, an edge-enhanced image (Fig. 4d) is produced by taking the weighted average of the smoothed image g and the edge-extracted image h :

$$k(x, y) = w_0 * g(x, y) + w_1 * h(x, y)$$

w_0 and w_1 are empirically determined to be 0.1 and 0.9 for DRRs and 0.15 and 0.85 for X-ray images.

2.2.3 Similarity Metric

The similarity between edge-enhanced X-ray and MDRR images is measured using normalized correlation (r) which has been reported as one the best performing similarity metrics [60] for high-resolution, real clinical data.

$$r_{(j=1,2)} = \frac{\sum (I_{Xray_j}(x, y) - \bar{I}_{Xray_j})(I_{MDRR_j}(x, y) - \bar{I}_{MDRR_j})}{\sqrt{\sum (I_{Xray_j}(x, y) - \bar{I}_{Xray_j})^2} \sqrt{\sum (I_{MDRR_j}(x, y) - \bar{I}_{MDRR_j})^2}} \quad (2.4)$$

for all pixels (x, y) such that $I_{MDRR}(x, y) \neq 0$. Here, j denotes the X-ray camera number of the bi-plane X-ray system. Following Bey et. al. [11], correlations for two sets of X-ray and MDRR images are multiplied to get the final matching score.

$$corr(I_{Xray_1}, I_{Xray_2}, I_{MDRR_1}, I_{MDRR_2}) = r_1 * r_2$$

2.2.4 Hierarchical Optimization

While MDRRs have the potential to increase the accuracy and robustness of tracking, they also pose challenges in terms of the optimization of search space. We use a quasi-Newton optimization method for finding the point of the maximum matching score. Each bone i has 6 degrees of freedom, expressed in matricial form as: $M_i = (T_x, T_y, T_z, R_x, R_y, R_z)$, the concatenation of 3 translations and 3 rotations. Translations and rotations are specified with respect to a local coordinate system. The origin (CT_x, CT_y, CT_z) of the local coordinate system (shown in Fig. 5a) is the center of mass of a CT object:

$$CT_{(X=x,y,z)} = \frac{\sum X * f(x, y, z)}{\sum f(x, y, z)}$$

where f denotes the CT image.

The objective function for the optimization method is:

$$\max_{T_x, T_y, T_z, R_x, R_y, R_z} \prod_{j=1,2} \text{corr}[I_{Xrayj}, I_{MDRR_j}(T(CTObject))]$$

where

$$T = T_x.T_y.T_z.R_x.R_y.R_z.T_{-CT_x}.T_{-CT_y}.T_{-CT_z}$$

is the composite transformation matrix and j denotes the two cameras of a DSX system. The equation shows optimization of a single bone; however, it can be expanded for multiple bones as necessary. The search is initialized by a human operator for the first two frames. For the remaining frames, initialization is done by exploiting temporal coherence.

Ideally, all bones of the spinal column would be present in the MDRR and the optimization algorithm would tackle all bones simultaneously. However, such an approach becomes computationally intractable due to the large, relatively unorganized search space and to the large number of degrees of freedom ($6n$ where n is the number of the bones). In contrast, employing temporal coherence, inter-frame and inter-bone motion priors, and a systematic hierarchical technique can reduce the search space significantly. At the same time, a hierarchical approach should allow sufficient degrees of freedom between bones to capture joint motion accurately.

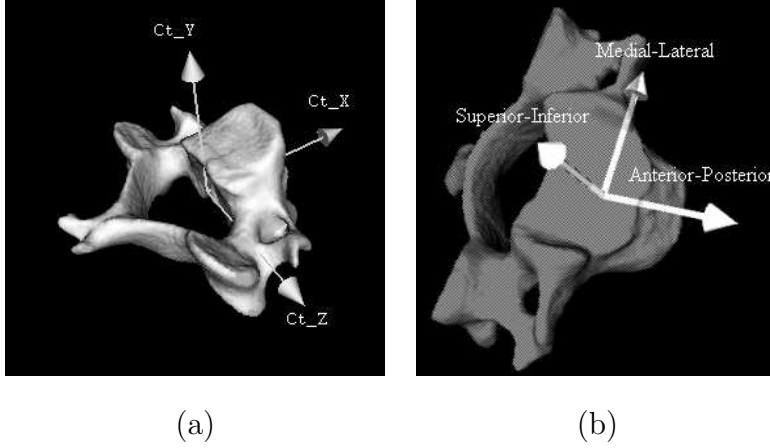


Figure 5: The local (a) and anatomical (b) coordinate systems defined for a vertebra

Based on the above observations we chose a coarse-to-fine, multi-pass strategy. The first two passes correspond to a coarse search for the bone location and orientation. Due to the fewer degrees of freedom and more constraints, phases 3 and 4 correspond to a fine tuning stage; phase 4 imposes more constraints on the searching than phase 3.

In terms of relative contribution, early experiments showed that phase 1 and 3 significantly impact the registration robustness. The exclusion of phase 1 in the search method produced off-track solutions and the exclusion of phase 3 produced very poor quality solutions. Phase 2 and 4 contribute primarily to tracking accuracy. Together, the four phases complement each other and lead to a robust and accurate solution, as demonstrated in Section 2.2.5.

Below we describe each phase in detail using an example linear hierarchy consisting of n bones, B_1 (first) through B_n (last). Let K_i be the set of bones which are used to generate MDRR at the i^{th} round of a given phase and $L_i = (B_j | F_k)$ be the subset of bones B_j in K_i which are optimized during the i^{th} round of the given phase, given the fixed position and orientation of the F_k bones.

Phase 1: Temporal Coherence The first phase uses temporal coherence to find a good starting position for each bone (Fig. 6). Using the position and orientation of a bone in the most recent two frames, we predict the most likely area in the current frame to search for the

optimal position and orientation. We extrapolate the positions of the previous two solved frames ($r1$ and $r2$ in Fig. 6) to predict the position in the current frame. Then we generate intermediate positions (intermediate circles in Fig. 6) between the predicted position and the position of the closest solved frame. Finally, we find the best-match position among all these potential positions. The rationale of multiple intermediate points is that a bone can change its direction and speed of movement. Multiple intermediate points help to compensate for this variation in speed and direction. Subsequent phases thoroughly search the region surrounding a selected seed location (cross points in Fig. 6) in order to capture accelerated and decelerated motion. The intermediate seed points are generated uniformly so that the translation difference or the angle difference between two consecutive seed points are at most 0.5 mm or 0.5° .

The sets K_i and L_i for this phase are: $K_i = \{B_i\}$ and $L_i = K_i$ where $i = 1 : n$.

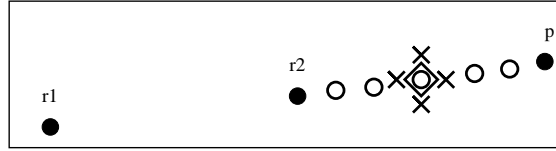


Figure 6: A conceptual 2D diagram of phase 1. $r1$ and $r2$ represent the bone in the previous two solved frames. p is the predicted point for current frame. Intermediate circles represent the additional intermediate points. The circle within the diamond represents the selected seed point. The cross points represent the surrounding regions which are going to be searched in the next phases.

Phase 2: Pairwise Optimization The purpose of phase 2 is to refine the seed location from phase 1 with the help of adjacent bone location information. To this end, we optimize each pair of adjacent bones (e.g. $B1 - B2$, $B2 - B3$ and so on) in the hierarchy by optimizing over 12 degrees of freedom. Optimizing two adjacent bones simultaneously helps adjust their position and orientation with respect to each other. This optimization step is computationally tractable while providing the necessary and sufficient degrees of freedom between neighboring bones in order to adjust their relative position and orientation.

$$K_i = \{B_i, B_{i+1}\} \text{ and } L_i = K_i$$

where $i = 1 : n - 1$.

Since bone kinematics are temporally smooth, we further constrain the search space by including motion priors into the optimization. The search range is restricted within twice (empirically determined) the magnitude of the bone motion in the most recent two frames. This motion prior allows sufficient freedom for bone movement but prevents sudden large movement. Theoretically, the search space could be further reduced by incorporating the fact that different bones cannot penetrate each other. However, the computational cost of detecting 3D inter-penetration makes such an approach less desirable.

Phase 3: Biased Singleton Refinement The purpose of this phase is to refine the position and orientation for each bone by searching in the region chosen by phase 2. We note that the bones of a hierarchy are unequally easy to track. For example, bones at the top (e.g. cervical vertebra C3 in a hierarchy of C3-C7) are easier to track due to less soft tissue and less interference from surrounding bones. The hierarchical search method takes advantage of this prior information by biasing the order in which individual bones are optimized. In the spine case, we optimize each bone of the chain sequentially (starting from the top of the chain and moving towards the bottom) in the presence of the previous bone in the hierarchy. Since we optimize one bone at a time, the optimization is over 6 degrees of freedom.

$$K_i = \{B_1, \dots, B_i\} \text{ and}$$

$$L_i = \{B_i | B_1, \dots, B_{i-1} \text{ are kept fixed}\}$$

where $i = 1 : n$.

Phase 4: Neighbor-Constrained Refinement This is a refinement phase that works similarly to phase 3, but takes into account both predecessor and successor bones in the hierarchy. The movement of each bone during the optimization is restricted by the presence of all the surrounding bones of the hierarchy. This helps to find the optimal position and orientation for the whole hierarchy.

$$K_i = \{B_1, \dots, B_n\} \text{ and}$$

$$L_i = \{B_i | B_1, \dots, B_{i-1}, B_{i+1}, \dots, B_n \text{ are kept fixed}\}$$

where $i = 1 : n$.

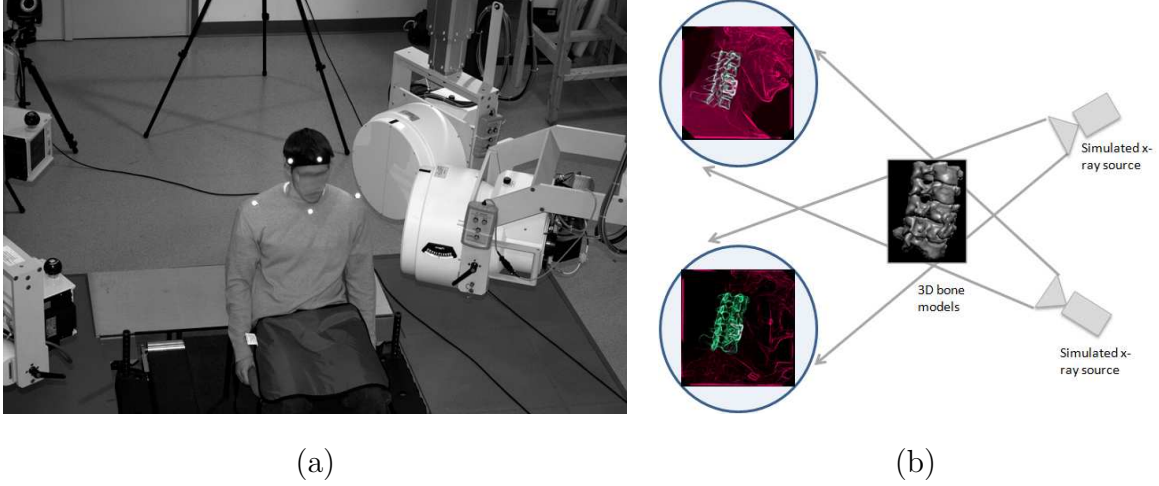


Figure 7: System configuration of the bi-plane X-ray setup for cervical spine trials (a) and the schematic diagram of the setup (b). X-ray sources direct X-rays through the subject to image intensifiers.

2.2.5 Validation

Datasets. To validate and evaluate the hierarchical, multi-bone approach we used in vivo conditions and real clinical data. 3D volumetric images of the bones of interest were obtained from a high resolution static computed tomography (CT) scanner (LightSpeed 16, GE Medical Systems, Waukesha, WI). CT images were segmented using 3D medical imaging software (Mimics, Materialize Inc, Leuven, Belgium) to extract individual bone geometry.

A Dynamic Stereo X-ray (DSX) system was used to capture high resolution X-ray images at a high frame rate. DSX utilizes two frame-synchronized imaging systems, specifically designed for dynamic measurement and mounted in a custom-designed, flexible positioning system to optimize viewing angles and provide freedom of subject movement. Each imaging system includes a 100 kW constant-potential high-frequency cardiac cine-radiographic generator (CPX-3100CV, EMD, Quebec, CA), a 0.3/0.6 mm focal spot size X-ray tube (G-1582; Varian, Salt Lake City, UT), a 40 cm image intensifier (TH9447QX; Thales, France), and a high-speed camera providing 1800x2400 pixel resolution at up to 500 frames/sec with 14-bit dynamic range (Phantom V10; Vision Research, Inc., Wayne, NJ). The EMD X-ray gen-

erators included upgraded software (provided by the manufacturer) to provide 1 ms pulses at repetition rates up to 180 Hz, providing blur-free images and a dose reduction of 4-16X (relative to continuous operation). A calibration object (a cube) is used to calibrate the camera system. Figure 7 shows the system configuration for a flexion-extension trial; X-ray beams are approximately 50 degrees apart. For twist trials, the subject is rotated to face one X-ray source, and the X-ray sources are lowered and tilted up 15 degrees, while the image intensifiers are raised and tilted down 15 degrees.

Following approval from our Institutional Review Board (Pitt IRB), 13 trials were acquired from 3 human subjects (1 male, 2 female, aged between 35 - 40) — 3 flexion/extension and 3 axial rotation trials from subject 1 and 2 and 1 flexion/extension trial from subject 3. Two of the test subjects have single-level anterior fusion in C5 and C6 and the remaining subject has single-level anterior fusion in C4 and C5. A fusion is performed by attaching a metal plate with two vertebral bodies using 4 screws. Trials from the subjects were taken between 6 and 7 months post surgery.

Tantalum beads were implanted into the fused cervical vertebrae and their adjacent bones during the fusion surgery so that a high accuracy ground truth solution could be produced by tracking the beads [5]. The subject with C4-5 fusion had beads into cervical vertebrae C3, C4, C5 and C6. Subjects with C5-6 fusion had beads into cervical vertebrae C4, C5, C6 and C7. Bead signatures were manually removed from the CT slices prior to MDRR generation by replacing voxels containing bead signatures with the average of the neighborhood voxels which do not belong to beads. In this way the beads did not influence the hierarchical and the operator-assisted tracking methods. For validation purposes, the center of each bead was also manually identified in the CT scans.

For these subjects and trials we tracked 5 cervical vertebrae (C3 - C7) and the fusion hardware. In the clinical study that generated this data cervical vertebrae C1 and C2 were not tracked, and so they did not have beads implanted into them to produce a ground truth solution. Table 1 shows additional specifications of our datasets.

Ground Truth. We obtain the ground truth by tracking the implanted beads in the distortion-corrected radiographs as described previously [5]. To validate this ground truth, we measure bias and precision [1]. Summarizing these references, first inter-bead distances

Bone	Cervical Spine ($C3 - C7$)
Motion	Flexion/extension, axial rotation
Total trials	13
Original CT Resolution(mm)	0.23x0.23x1.25
Interpolated CT resolution (mm)	0.23x0.23x(0.23~0.5)
X-ray image resolution	1024x1024
Number of frames per trial	60 ~ 100
Frame capturing rate	30 frames/sec
Pixel size of x-ray image (mm)	0.30x0.30

Table 1: Experiment data set specification

(d_i where i is the frame number) are calculated per bone over an entire trial from the bead tracking (i.e. ground truth) results. True inter-bead distance (D) is measured by manually detecting the beads in the CT image. Next, differences between the inter-bead distance computed from the CT data and the bead tracking based solution ($D - d_i$) are calculated for each frame over an entire trial. Bias and precision are defined as the mean and standard deviation of the differences over the entire trial and are summarized over all trials to report in the form mean \pm standard deviation. Bead-based tracking is used as the “gold standard” to calculate the accuracy of the operator-assisted single-bone and hierarchical multi-bone tracking.

Analysis. Performance of the operator-assisted single-bone and the hierarchical multi-bone methods are compared for each bone and each axis in terms of bias, precision [5, 1] root-mean-squared (rms) error, and maximum error. These performance metrics are computed with respect to the bead-based ground truth solution. For each method (operator-assisted, ground truth and hierarchical) the bead centroid locations are computed as the average of the three known bead coordinates of a bone over all frames of a trial. The differences between estimated bead centroid (hierarchical or operator-assisted method) and the ground truth bead centroid locations are computed for each bone and for each axis across all frames of a trial. Bias, precision, rms error and maximum error are defined as the mean, standard deviation, rms value and maximum value of this time-history of differences. Finally, bias, precision and rms error are summarized as the mean, standard deviation and maximum error over all trials. To compare the performance of the operator-assisted and the hierarchical

method for a bone along all three axes simultaneously, Hotteling’s T-squared tests ($\alpha = 0.05$) are performed for the three axes on bias, precision and also rms error of the bone.

To further compare the accuracy of both methods in clinically relevant terms, an anatomical coordinate system was defined at the center of each vertebra [49]. The axes of the anatomical coordinate system are Anterior-Posterior (AP) axis, Superior-Inferior (SI) axis and Medial-Lateral (ML) axis, and correspond to the main axes of the vertebral body (Fig. 5.b). Translations and rotations of each pair of vertebrae with respect to the three axes are computed from the bead-based, the assisted single-bone and the hierarchical multi-bone method solutions. Error (in terms of bias and precision) in the assisted single-bone method and the hierarchical method with respect to the bead-based ground truth is computed and then tested using a Hotteling’s T-squared test ($\alpha = 0.05$).

In our experiments, the operator-assisted single-bone method was guided by an expert operator and the solution was checked and refined manually. The hierarchical method did not require any human assistance after initialization. We compare the solutions from these two methods in terms of accuracy, robustness and run time.

2.3 RESULTS

There was no bias in the implanted bead tracking solution (Table 2) i.e. in the ground truth. Average precision over all bones is 0.11 mm which is very similar to results published earlier [5, 6].

Bone	Bias	precision
C3	0.05±0.03	0.11±0.02
C4	0.04±0.03	0.10±0.03
C5	-0.04±0.10	0.12±0.02
C6	0.04±0.07	0.12±0.04
C7	0.02±0.05	0.08±0.03

Table 2: Bead-based tracking accuracy (bias and precision). All measurement units are in mm.

2.3.1 Accuracy

We compare the accuracy of the operator-assisted single-bone and the hierarchical multi-bone methods in terms of bias, precision, rms error and maximum error for each bone along each axis direction.

Mean \pm standard deviation of bias over all trials						
	Hierarchical multi-bone method			Operator-assisted single-bone method		
Axis	X	Y	Z	X	Y	Z
C3	0.04 \pm 0.12	0.01 \pm 0.17	0.08 \pm 0.05	-0.04 \pm 0.17	-0.04 \pm 0.22	0.03 \pm 0.08
C4	0.07 \pm 0.08	0.02 \pm 0.15	0.18 \pm 0.16	-0.03 \pm 0.13	0.05 \pm 0.09	0.21 \pm 0.14
C5	0.19 \pm 0.20	0.06 \pm 0.39	-0.07 \pm 0.31	0.22 \pm 0.18	0.11 \pm 0.29	-0.07 \pm 0.42
C6	-0.08 \pm 0.25	-0.04 \pm 0.10	0.07 \pm 0.14	0.00 \pm 0.49	0.12 \pm 0.22	0.04 \pm 0.14
C7	-0.18 \pm 0.14	-0.27 \pm 0.06	-0.12 \pm 0.18	-0.13 \pm 0.06	-0.16 \pm 0.10	0.02 \pm 0.07

Table 3: Bias of the hierarchical method and the operator-assisted method. All measurement units are in mm. We did not find any statistical significant difference in bias ($p > 0.01$) for any bone along any axis direction between the hierarchical and the operator-assisted method.

Figure 8 shows the bias in the hierarchical multi-bone method and the operator-assisted single-bone method. We did not find any statistically significant difference ($p > 0.01$) in bias between the hierarchical and the operator-assisted methods (Table 3) for any bone in any coordinate system direction. This finding indicates that the hierarchical multi-bone method has similar accuracy to the operator-assisted single-bone method. C5 and C6 have relatively higher bias than C3, C4 and C7 along the X and Y axes both for the operator-assisted single-bone and the hierarchical methods. Maximum bias of C3, C4 and C7 using the operator-assisted single-bone method along the X and Y axes are approximately 7 and 3 times higher than the maximum bias of C5 and C6 using the same method along X and Y axes. In contrast, maximum bias of C3, C4 and C7 using the hierarchical multi-bone method along the X and Y axes is approximately 3 and 4 times higher than the maximum bias of C5 and C6 using the same method along the X and Y axes. C5 and C6 tracking results show relatively higher bias than other bones because C5 was fused in all three of our subjects and C6 was fused in two of our three subjects. Fused vertebrae are typically harder to track due to relatively inaccurate CT-scan models of the fused bones (extracting a CT bone model from fused vertebrae is more difficult than extracting a bone model from non-

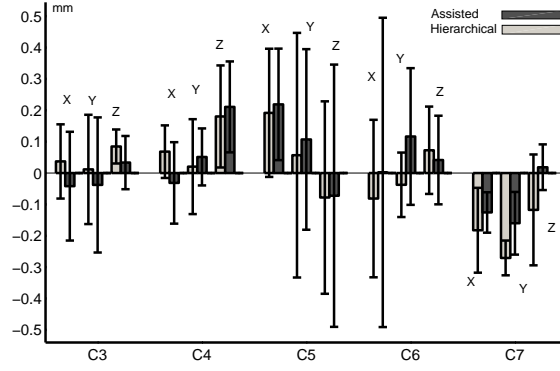


Figure 8: Bias of the hierarchical method and the operator-assisted method. X, Y and Z denote the axes of comparison. We did not find any statistically significant difference ($p > 0.01$) in bias between the hierarchical and the operator-assisted methods for any bone along any axis direction. However, note that the bias for C5 and C6 is relatively higher than the bias for C3, C4 and C7 due to the hardware implant in C5 and C6. Still, the hierarchical multi-bone method has achieved sub-millimeter accuracy for C5 and C6 (max bias 0.62 mm) along with the other vertebrae. Results are averaged over 13 trials from 3 subjects, 60 ~ 100 frames per trial.

fused vertebrae), interference from hardware during tracking etc. However, the bias for the hierarchical method for C5 and C6 along any axis was less than 0.62 mm; for the operator-assisted single-bone method it was less than 1.07 mm which indicates that the hierarchical multi-bone method has sub-millimeter accuracy for all vertebrae, including the ones which have been affected by fusion surgery.

Mean \pm standard deviation of precision over all trials						
	Hierarchical multi-bone method			Operator-assisted single-bone method		
Axis	X	Y	Z	X	Y	Z
C3	0.20 \pm 0.05	0.16 \pm 0.09	0.12 \pm 0.02	0.21 \pm 0.08	0.16 \pm 0.04	0.14 \pm 0.05
C4	0.09 \pm 0.03	0.09 \pm 0.03	0.07 \pm 0.02	0.12 \pm 0.07	0.12 \pm 0.05	0.09 \pm 0.04
C5	0.13 \pm 0.04	0.14 \pm 0.04	0.09 \pm 0.02	0.22 \pm 0.11	0.16 \pm 0.05	0.12 \pm 0.05
C6	0.14 \pm 0.07	0.13 \pm 0.07	0.07 \pm 0.02	0.19 \pm 0.10	0.19 \pm 0.13	0.12 \pm 0.08
C7	0.09 \pm 0.02	0.11 \pm 0.05	0.07 \pm 0.03	0.10 \pm 0.02	0.15 \pm 0.09	0.07 \pm 0.04

Table 4: Precision of the hierarchical method and the operator-assisted method. All measurement units are in mm. We did not find any statistical significant difference ($p > 0.01$) in precision between the hierarchical and the operator-assisted method for any bone in any coordinate system direction.

Figure 9 compares precision of the hierarchical multi-bone method and the operator-assisted single-bone method. Hierarchical multi-bone method precision ranged from 0.03 mm to 0.34 mm depending on axis direction. Operator-assisted single-bone method precision ranged from 0.04 mm to 0.55 mm depending on axis direction. We did not find any statistically significant difference ($p > 0.01$) in precision between the hierarchical and the operator-assisted methods (Table 4) along any coordinate system direction. Precision was bone-independent for both of the methods. The last bone to track (C7) shows slightly worse accuracy in the hierarchical method than in the operator-assisted single-bone method. A possible explanation is that C7-s have more soft tissue surrounding them compared to other bones in the dataset. Therefore, the assumption of negligible contribution in pixel intensity due to surrounding soft tissue for MDRR generation (Eq. 2.3) may no longer hold for C7, making human intervention particularly valuable. We note that for the operator-assisted single-bone method C5 and C6 show slightly lower precision (statistically not significant) than C3, C4 and C7.

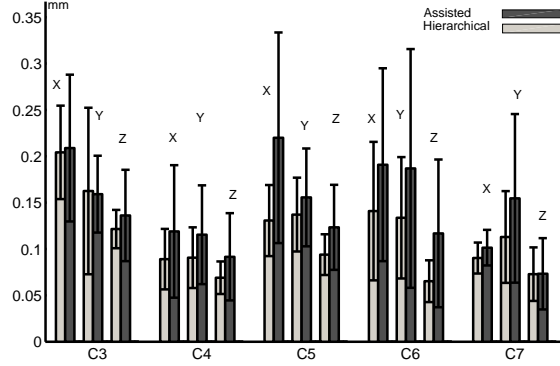


Figure 9: Precision for the hierarchical and the operator-assisted single-bone method. X, Y and Z denote the axes of comparison. We did not find any statistical significant difference ($p > 0.01$) in precision between the hierarchical and the operator-assisted method for any bone in any coordinate system direction. Results are averaged over 13 trials from 3 subjects, 60 \sim 100 frames per trial.

Mean \pm standard deviation of root-mean-squared error over all trials						
	Hierarchical multi-bone method			Operator-assisted single-bone method		
Axis	X	Y	Z	X	Y	Z
C3	0.23 \pm 0.05	0.23 \pm 0.07	0.15 \pm 0.03	0.26 \pm 0.10	0.25 \pm 0.08	0.16 \pm 0.04
C4	0.14 \pm 0.04	0.16 \pm 0.08	0.23 \pm 0.10	0.17 \pm 0.09	0.15 \pm 0.05	0.26 \pm 0.10
C5	0.26 \pm 0.16	0.35 \pm 0.21	0.29 \pm 0.13	0.37 \pm 0.16	0.30 \pm 0.16	0.32 \pm 0.30
C6	0.24 \pm 0.18	0.17 \pm 0.07	0.15 \pm 0.07	0.42 \pm 0.31	0.26 \pm 0.20	0.17 \pm 0.11
C7	0.21 \pm 0.12	0.30 \pm 0.05	0.16 \pm 0.16	0.17 \pm 0.05	0.24 \pm 0.08	0.10 \pm 0.05

Table 5: Root-mean-squared error of the hierarchical method and the operator-assisted method. All measurement units are in mm. We did not find any statistical significant difference ($p > 0.01$) in rms error between the hierarchical and the operator-assisted method for any bone in any coordinate system direction.

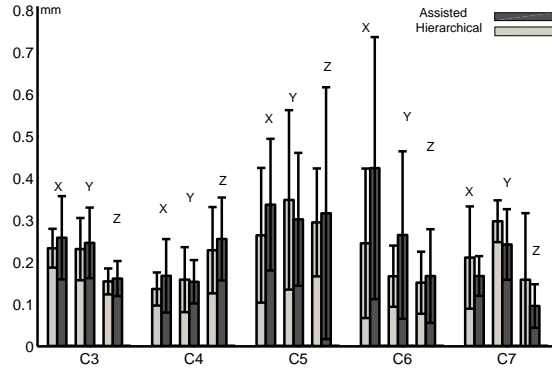


Figure 10: Root-mean-squared error (mm) for the hierarchical and the operator-assisted single-bone method. X, Y and Z denote the axes of comparison. We did not find any statistical significant difference ($p > 0.01$) in rms error between the hierarchical and the operator-assisted method for any bone in any coordinate system direction. Results are averaged over 13 trials from 3 subjects, 60 ~ 100 frames per trial.

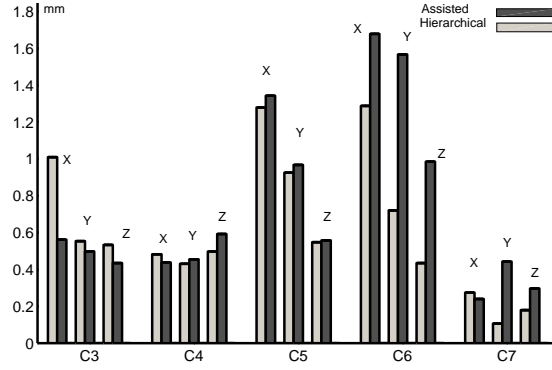


Figure 11: Maximum error for the hierarchical and the operator-assisted single-bone method. X, Y and Z denote the axes of comparison. The automated hierarchical method is as accurate as the operator-assisted method. Please note that relatively higher values of maximum error (compared to rms error, bias and precision) indicate the presence of some outliers X-ray frames with poorer image quality than most other frames of a motion sequence. Results are summarized over 13 trials from 3 subjects, 60 ~ 100 frames per trial.

Figure 10 shows the root-mean-squared (rms) error of the hierarchical and the operator-assisted methods. Root-mean-squared error indicates no statistically significant difference ($p > 0.01$) between the hierarchical and the operator-assisted methods (Table 3) for any bone in any coordinate system direction. From Fig. 10, we can see that vertebrae C5 and C6 show slightly higher rms error than the vertebrae C3, C4 and C7 for the operator-assisted single-bone method. For the operator-assisted single-bone method, the maximum rms error is 1.11 mm for C5 and C6, and 0.44 mm for C3, C4 and C7. For the hierarchical multi-bone method, the maximum rms error is 0.70 mm for C5 and C6, and 0.51 mm for C3, C4 and C7. The rms error result again indicates that the hierarchical multi-bone method is as accurate as the operator-assisted single-bone method even for the vertebrae with fusion hardware.

Figure 11 shows the maximum error of the hierarchical and the operator-assisted method. It is interesting to see that for both of the methods the maximum error is often greater or close to 1 mm (especially for C5 and C6). Considering the sub-millimeter level values found in bias, precision and rms error analysis, these high values in maximum error analysis indicate the presence of outliers X-ray frames where the image quality is relatively poorer than most other frames. According to our expert operators, this is often the case and the operator-assisted single-bone method fails mainly for these outliers frames.

Maximum error						
	Hierarchical multi-bone method			Assisted single-bone method		
Axis	X	Y	Z	X	Y	Z
C3	1.01	0.55	0.53	0.56	0.50	0.43
C4	0.48	0.43	0.50	0.43	0.45	0.59
C5	1.28	0.93	0.55	1.34	0.97	0.56
C6	1.28	0.72	0.43	1.68	1.57	0.99
C7	0.27	0.11	0.18	0.24	0.44	0.30

Table 6: Maximum error of the Hierarchical method and the operator-assisted method. All measurement units are in mm.

Table 7 and Table 8 summarize the translation and rotation analysis with respect to anatomical coordinates. For the hierarchical approach, the average precision in measuring 3D joint kinematics is 0.27 mm for translations (compared to 0.37 mm using the operator-assisted method) and 1.09° for rotations (compared to 1.10° for the operator-assisted method). Hotelling’s T-Squared testing ($p > 0.01$) found no statistically significant difference between the

two methods.

Translation accuracy in anatomical coordinate system over all trials						
	Hierarchical multi-bone method			Operator-assisted single-bone method		
Axis	LM	SI	AP	LM	SI	AP
Bias	0.46 ± 0.67	0.22 ± 0.33	0.85 ± 1.10	0.47 ± 0.59	0.09 ± 0.32	0.69 ± 0.75
Precision	0.25 ± 0.06	0.20 ± 0.12	0.35 ± 0.17	0.32 ± 0.09	0.40 ± 0.34	0.41 ± 0.17

Table 7: Translational (anatomical coordinates) bias and precision of the hierarchical method and the operator-assisted method. All measurement units are in mm. There was no statistically significant difference (Hotteling’s T-Squared, $p > 0.01$) in bias and precision between the hierarchical and the operator-assisted method.

Rotation accuracy in anatomical coordinate system over all trials						
	Hierarchical multi-bone method			Operator-assisted single-bone method		
Axis	LM	SI	AP	LM	SI	AP
Bias	-0.31 ± 2.80	-0.17 ± 1.59	0.31 ± 1.49	-0.08 ± 1.71	-0.14 ± 1.65	0.32 ± 1.55
Precision	1.26 ± 0.46	0.95 ± 0.26	1.08 ± 0.47	1.37 ± 0.51	0.94 ± 0.24	0.97 ± 0.19

Table 8: Rotational (anatomical coordinates) bias and precision of the hierarchical method and the operator-assisted method. All measurement units are in degrees. There was no statistically significant difference (Hotteling’s T-Squared, $p > 0.01$) in bias and precision between the hierarchical and the operator-assisted method.

A quantitative analysis of the implant hardware motion could not be performed due to the lack of a bead-based ground truth solution. However, two human expert operators manually checked the hierarchical method tracking solution of the implant hardware. According to the expert operators, the hierarchical method tracking solution of implant hardware was accurate and those experts often commented that the hierarchical tracking solution seemed better than the operator-assisted method tracking solution.

To further analyze the effect of implant hardware on method accuracy, we used the hierarchical method to track a trial (subject 1, flexion-extension trial 1) without including the implant hardware in the MDRR generation process. This approach produced very poor quality solution for the fused vertebra C5, while the other fused vertebra C6 went off track around frame 15.

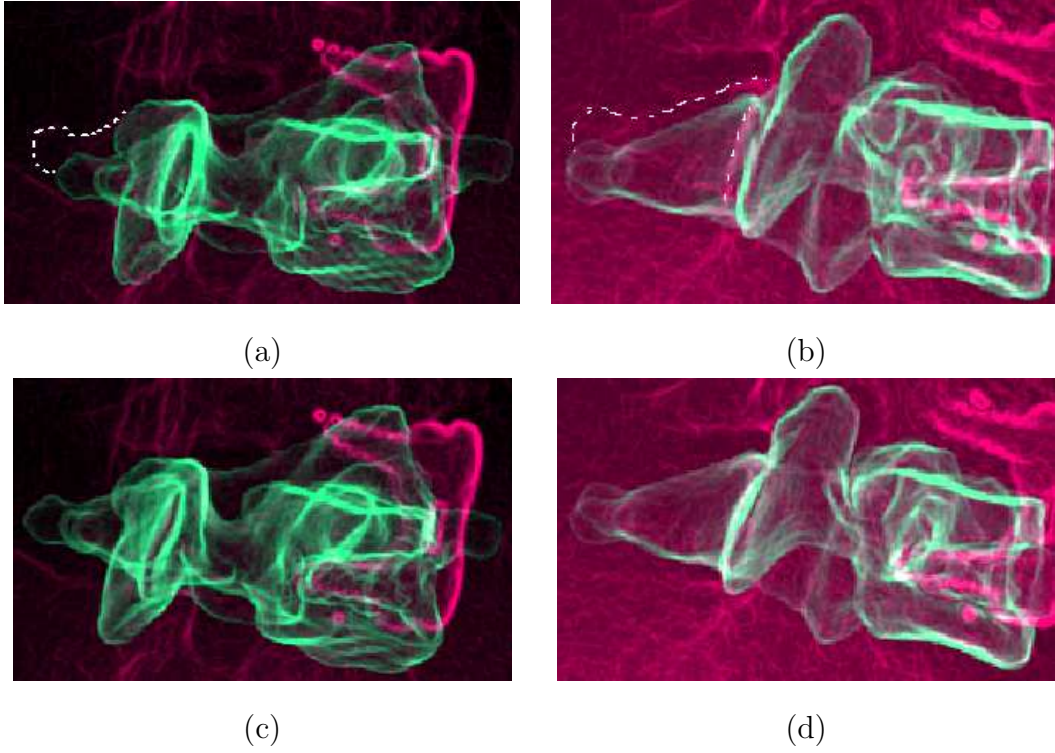


Figure 12: Comparison of tracking results between the single-bone method without operator assistance (top row) against the hierarchical approach without operator assistance (bottom row). In each row, the two camera views are shown, with the vertebra (green) superimposed on the X-ray image (red); dotted lines show the target location of the vertebra. Note the single-bone solution is off-track, while the hierarchical one is on target.

2.3.2 Robustness

The hierarchical multi-bone approach was significantly more robust than the operator-assisted method. We tracked 13 trials from the 3 subjects. To compare the robustness of the hierarchical method with the single-bone method, we tracked these trials using the single-bone method without human operator assistance after initialization of the reference frames. The single-bone method failed to track 5 trials (3 flexion/extensions and 1 axial rotation from subject 1, 1 flexion/extension from subject 3). In all these trials, either vertebra C5 or C6 went significantly off track. For example, in the flexion/extension trial from subject 3, vertebra C6 went visibly off track around frame 6 and the bone remained off track for the rest of the frames. C6 also went off track in all 3 flexion/extension trials from subject 1 approximately around frame 10. C5 went off track in one axial rotation trial from subject 1 around frame 15. Although the single-bone method was able to complete tracking the remaining 8 trials, the tracking results required significant manual correction through human operator intervention.

2.3.3 Run Time

We used a Windows based cluster with 24 Intel Xeon (2.0 GHz) processors to run both the operator-assisted and the hierarchical tracking methods. The operator-assisted single-bone method required approximately 1 hour to track a single cervical vertebra in a single trial of 60 \sim 90 frames, leading to a total of 6 hours for the five cervical vertebrae and the metallic implant. 96% of the time was spent on human interaction during the tracking (to keep bones on track) and the manual refinement phase. The hierarchical method tracked five cervical vertebrae and the metallic implant on average in approximately 25 minutes, i.e., it attained a speedup factor of 12. While having a faster solution is not the main contribution of this work, these run times indicate the hierarchical method is cost-effective, which is essential for clinical application.

2.4 DISCUSSION

The experimental results show that the hierarchical multi-bone method matches the sub-millimeter accuracy of the state-of-the-art operator-assisted single-bone. At the same time, the hierarchical method is superior to the single-bone method in terms of robustness and runtime. Notably, the hierarchical approach dramatically reduces the labor required for imaging studies, while making the accuracy and robustness of the method operator-independent.

An advantage of the hierarchical method is that it is able to track bones that change both direction and speed within each camera view during a specific trial, a task significantly more difficult than tracking a bone that moves in the same direction at a constant speed. In our experiments, no restrictions were imposed on the subjects during motion. The maximum range of motion was approximately 20 mm translation and 32° rotation; bone motion direction and speed had variations in all datasets.

In our experiments, we used post-operative CT scan data to extract a model of each hierarchy component to be tracked, be they vertebrae or additional hardware. However, a pre-operative CT scan can also be used with this approach. The pre-operative scan would be used to extract models of the bones; while the implant model can be acquired either through scanning or directly thanks to CAD designs.

We followed an incremental approach in developing the four step hierarchical searching process. For example, the initial searching process included only two steps (Phase 1 and 3) and produced a poor solution for the first node of the hierarchy. We tried several other structures for the hierarchical searching e.g. different orderings of the phases, and different orderings of the bones. These approaches did not produce any improvements over the approach described in this chapter.

To evaluate the relative contribution of a phase in the overall search accuracy and robustness, we performed experiments by excluding each phase. Experiments showed that phase 1 and 3 significantly impact the registration robustness. The exclusion of any of these phases in the search method often produced off-track solutions. Phase 2 and 4 contribute primarily to the tracking accuracy. Exclusion of these phases reduced accuracy. Accuracy reduction depended on the quality of the solution produced by the remaining phases. However, these

phases were required to produce the best quality solution for all the trials.

Furthermore, the hierarchical multi-bone method assumes that noise in X-ray images due to surrounding soft-tissue structure of cervical spine is negligible. However, it is often very challenging to avoid soft-tissue interference and get high quality noise-free X-ray images from both cameras of a DSX system due to restrictions imposed by a subject’s motion and body structure. Current model-based techniques, including the one reported in this chapter, frequently employ image filters as a pre-processing step to reduce noise due to soft tissue. Many of these image processing techniques [69] require manual tuning even for a single dataset, primarily due to overall intensity variation from frame to frame. Adjusting these parameters for different datasets (or for different frames within the same dataset) requires significant human effort, outweighing the benefits of the pre-processing step. Robust and automatic image pre-processing remains a direction of future work.

In our experiments we compare the performance of the hierarchical multi-bone method against the operator-assisted single-bone method which is to the best of our knowledge the current state of the art in the field [49]. Other model-based methods are primarily single-2D to 3D matching (i.e. they only collect one x-ray view [9, 51]). Banks [9] compares the accuracy of his method to others. To summarize, all matching that is done using only one X-ray view has large errors perpendicular to the imaging plane. This class of methods is highly unlikely to produce higher accuracy results than the biplane radiographic approach. Several groups do collect 2 X-ray views [12, 38]. They build bone models from MRI/CT and either manually match the model to the 2 X-ray views or use invasively implanted beads for the matching process. Given the fundamentally manual, respectively invasive matching processes used, these approaches are not preferable to either the expert-assisted method or the hierarchical method described here.

While our experiments use data acquired through a stereo-radiographic imaging system and a CT scanner, a variety of imaging hardware setups, including single-plane radiography, can be used in practice to acquire dynamic radiograph images. Stereo-imaging is more likely than single-plane radiography to suffer from image quality problems due to scatter radiation and thus tracking motion from stereo images is likely to benefit more from our approach. However, radiographic bone overlap and temporal coherence are traits of both single-plane

and stereo-imaging; our hierarchical tracking algorithm may enhance the accuracy and robustness of single-plane dynamic tracking. A major advantage of our approach is that in the long run it could eliminate the requirement for simultaneous image acquisition, thus leading to dramatic improvements in radiographic image quality.

2.5 CONCLUSION

In this chapter, we have introduced and validated an intelligent, hierarchical algorithm which improves the accuracy, reliability, and/or flexibility of the dynamic radiograph tracking process. The two significant innovations proposed – 1) multibone projection (MDRR); and 2) temporally-aware constrained hierarchical optimization – can be applied in combination to enable rapid, automated, accurate bone motion tracking and to facilitate clinical application.

When applied to cervical spine data, the new algorithm matched the sub-millimeter accuracy of the expert-operator existing tracking process, while being automated and operator-independent. The approach was also more robust in the presence of implanted hardware than the previous state-of-the-art tracking process. Finally, the approach sped up the total tracking time by a factor of 12. Preliminary evaluation indicates similar improvements on *in vitro* lumbar spine data [27].

Our automated process decreases the labor cost associated with human operators, which facilitates practical clinical application. Considering the relatively low levels of radiation involved by the imaging system (approximately half the amount of one cervical CT scan), the moderate hardware costs and the proliferation in recent years of biplane DSX systems, the automation of the tracking procedure shows promise for large-scale clinical application. Since the approach showed also good performance in the presence of implanted hardware, it can be used to study post-surgery cases and evaluate the effectiveness of a surgical intervention. Applications for this technology include (but are not limited to) assessment and diagnosis of musculoskeletal disorders, bone, ligament and joint injury, derangements of the spine and osteoarthritis.

3.0 LIGAMENT GEOMETRY MODELING

Ligaments constrain the movement of the human spine by anchoring together the adjacent vertebrae in the spine. Understanding the role of these ligaments can provide important insights into joint mechanics and lead to better understanding of spine related injuries and diseases. An automated, *in vivo* and dynamic modeling technique is essential to understand the role of the spine ligaments during everyday normal functionalities. Such a technique is also necessary for large scale experimentation with spine ligaments.

However, due to limitations in existing imaging technologies, no *in vivo* non-invasive method exists for dynamic modeling of spine ligaments. Ligament modeling techniques based on Computed Tomography (CT) or Magnetic Resonance (MR) images have been proposed for modeling soft-tissues in larger joints like the shoulder or the knee [29, 75]. However, such techniques do not transfer to the spine due to the complexity of the spine joints and small ligament structures.

We propose a semi-automated computational method for dynamic modeling the 3D surface of spine ligaments using computed tomography medical volumes and bone motion information. The key contributions of the proposed technique are the automation of the modeling process while maintaining geometric accuracy and enabling dynamic analysis for the spine ligaments which cannot be observed directly in non-invasive spine images. The idea behind our approach is that because ligament structures are directly constrained by bone motion, bone geometry, position and orientation over time can be used to compute geometric features of ligaments. This approach builds on recent advances in motion tracking technology, which enable us to reconstruct bone motion from *in vivo* images automatically. The resulting subject-specific dynamic ligament mesh models can help us to observe ligament deformation during motion. These models can also be used as inputs to joint simulation methods such

as Finite Element (FE) analysis.

3.1 RELATED WORK

Based on the nature of the generated models, ligament modeling techniques can be classified in the following three categories: 1. Static 2. Quasi-static techniques and 3. Dynamic.

Static or quasi-static mesh models [29, 75, 8] of large soft-tissue structures such as knee ligaments and cartilage have been generated from CT and MR images. However, the limited resolution of these imaging techniques and the complexity of spine joints make it practically impossible to apply these techniques for spine ligament modeling.

Manually generated spine ligament models have been used extensively in Finite Element (FE) analysis. However, the manual approach is labor intensive and time consuming which makes it impractical for real clinical application. Mesh morphing based techniques [7, 65, 66] have been developed to automate the mesh generation process of bones for FE analysis. However, these techniques cannot be applied to ligament modeling directly due to the large deformation of ligaments and the constrain imposed on ligaments by bones.

Ligament models with linear or piecewise linear mesh elements have been used in dynamic simulation of joints [20]. This method can represent more complex geometries by using analytical wrapping structures such as cylinders or spheres. Even though this method enables dynamic simulations and reduces the modeling complexity significantly, these oversimplified models cannot provide anatomically accurate insights into the ligament geometry and geometric deformations of ligaments that happen due to motion.

A quasi-static method [46] has been proposed for distal-radioulnar ligaments in the human forearm. The method generates one-dimensional ligament fiber models and uses motion information which is based on multiple static-postures over a motion sequence. In this chapter, we extend this approach to use dynamic motion information for creating 3D surface models of spine ligaments.

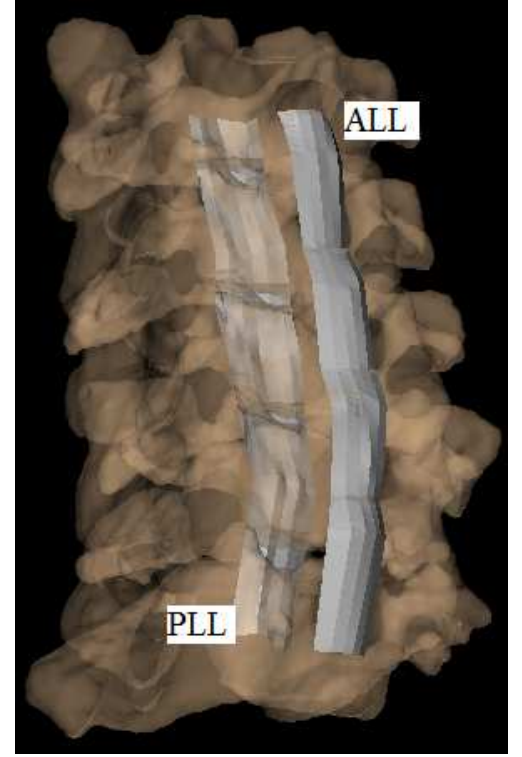
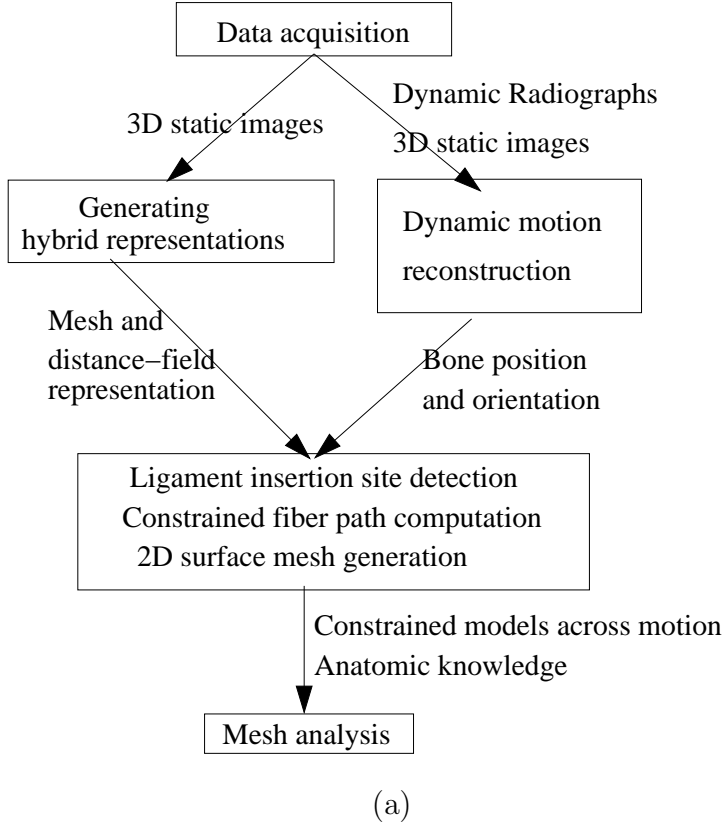


Figure 13: (a) Pipeline of the ligament modeling method. We compute dynamic motion information of vertebrae from 3D volume images and 2D dynamic radiographs. We select ligament insertion sites manually. We then compute constrained ligament meshes across motion using the bone geometry and the dynamic motion information. Finally, we compute features of the ligament geometry by analyzing the constrained geometries across motion. (b) Reconstructed Anterior Longitudinal Ligament (ALL) and Posterior Longitudinal Ligament (PLL) meshes of a subject.

3.2 MATERIALS AND METHODS

We propose a semi-automatic computational approach to reconstruct spine ligaments from captured dynamic images. Because the ligament tissue is geometrically constrained by the bone, we use the bone geometry and dynamic motion information to reconstruct the ligament geometry. The motion information allows us to capture the deformation of the ligament during motion.

Figure 13 shows the proposed method. We first capture 3D geometry of vertebrae using a static imaging technique. We then reconstruct the dynamic motion of vertebrae using an accurate and automatic method. The method uses dynamic X-ray images and the vertebrae models from the volumetric images to reconstruct the dynamic motion of vertebrae. We then compute two representations (mesh and distance-field) of the 3D bone geometry to facilitate faster computation of inter-vertebrae joint space measurements. Using the hybrid representations and the motion information of vertebrae, we compute the constrained ligament geometry over a complete movement sequence. We then analyze the constrained models to gain insight into the ligament geometry. We describe each step of the pipeline below.

3.2.1 Data Acquisition and Dynamic Motion Reconstruction

For data acquisition we use the system described in chapter 2. We obtain 3D volumetric images of the spine with a high-resolution computed tomography (CT) scanner (Light-Speed 16, GE Medical Systems, Waukesha, WI). We then segment the CT images using 3D medical imaging software (Mimics).

To obtain 3D motion information, we capture high-resolution radiographs (Fig. 14) with a dynamic stereo X-ray (DSX) system (Fig. 7a). DSX utilizes two frame-synchronized imaging systems each including a 100 kW cardiac cine-radiographic generator, a 0.3/0.6 mm focal spot size X-ray tube, a 40 cm image intensifier and a high-speed camera providing 1800x2400 pixel resolution at up to 500 frames/sec with 14-bit dynamic range. Please see section 2.2.5 for farther details of the system.

Next, we reconstruct 3D dynamic motion of vertebrae by applying a highly accurate

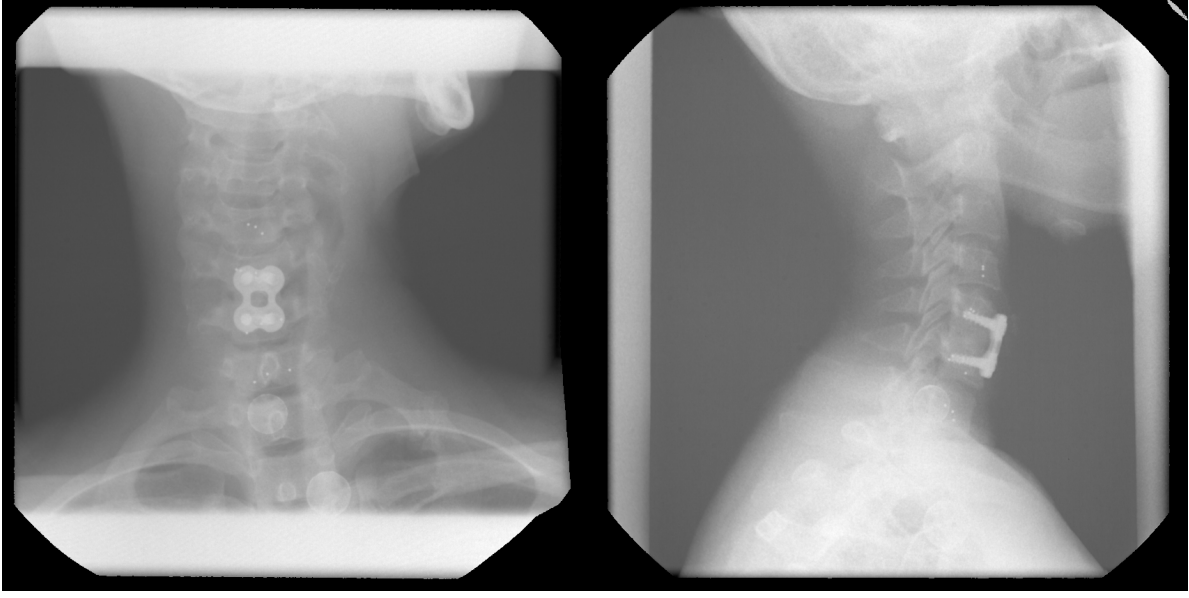


Figure 14: Two frames of the high resolution (1024x1024) radiograph sequences which are captured during motion from the dynamic stereo X-ray system.

model-based method [28] which has been shown to achieve sub-millimeter accuracy (average precision 0.3mm translation and 1° rotation) for in-vivo spine data. The basic premise for reconstructing bone motion is a model-based approach that matches radiographic images to a known bone shape (3D bone models obtained from the CT scans). A virtual model of the DSX imaging system is generated using the precise locations of the radiographic sources and image detectors. Simulated X-rays are passed through the bone models to produce a pair of digitally reconstructed radiographs (DRRs) on the image plane. By manipulating the bone model within a virtual radiographic system, pairs of DRRs can be generated for any bone position. By calculating image similarity measures between the actual radiographic image pairs and the DRRs, the virtual bone position and orientation can be adjusted (manually or by an optimization algorithm) to identify the position that provides the greatest match, thus determining the position of the actual bone in space. This process is repeated for each pair of the images in the motion sequence, and repeated again for each bone of interest to yield the 3D position of the joint for the entire movement.

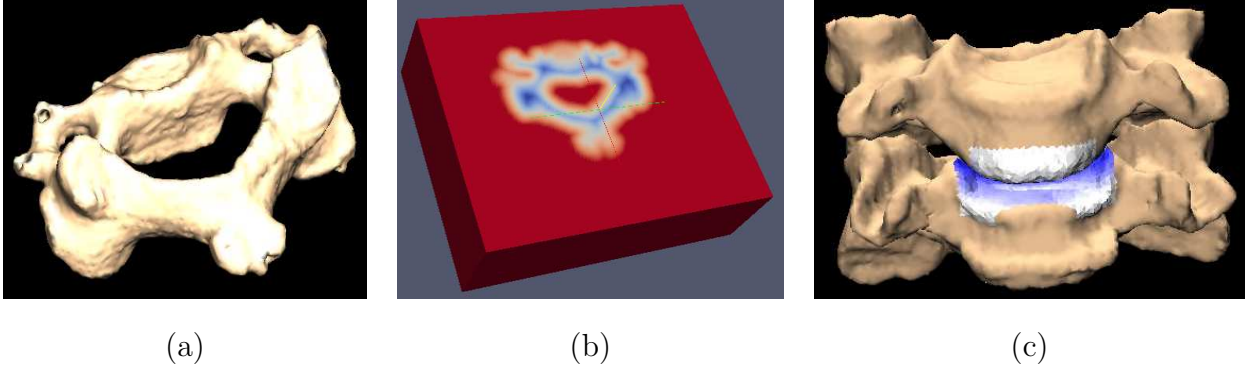


Figure 15: (a) The explicit mesh representation of the bone. (b) A 2D crosscut through the distance field representation. Red indicates points outside the bone surface and blue indicates points inside the bone surface. The distance from the surface is mapped to the color saturation level. (c) Visualization of the inter-bone joint space computed using the distance-field information; darker colors indicate shorter distance between the two adjacent bone surfaces.

3.2.2 Bone Geometry Representations

Our proposed computational modeling method utilizes two representations of the bone geometry to reconstruct the geometric model of the ligament. The first representation is the mesh representation constructed from the segmented CT volumetric image using the standard computer graphics technique such as the marching cube algorithm [41]. The bone models are segmented semi-automatically by domain experts using a combination of segmentation techniques (e.g. region growing, thresholding) and the resulting models are manually corrected to obtain highly accurate bone models. The resulting mesh models have between 10k \sim 20k vertices and 20k \sim 50k faces per vertebra. The mesh representation (Figure 15a) is used for manual identification of ligament insertion sites as discussed in the next section and to visually confirm the correctness of the generated models.

To enable faster distance computation in the joint space, we use another representation of the bone geometry — implicit distance field representation [48]. The distance field representation is stored as a discrete 3D array. The value at each point of the 3D array indicates

the distance to the closest point on the bone surface. The distance-field representation allows us to compute the closest point on a bone surface from any arbitrary point efficiently.

3.2.3 Computing Constrained Ligament Paths

Using the bone representations and dynamic motion information, we reconstruct 3D surface models of ligament path constraints. The models represent the minimum-length ligament paths wrapped around the bone surface and constrained by the bone geometry and position.

The 3D surface model creation begins with the ligament insertion site (the points where the ligament is attached to the bone) identification. Because, the ligament insertion site can vary between subjects and joints, we rely on human expertise for insertion site identification. We manually identify an array of points (~ 10 per vertebra) as ligament insertion sites for each bone. Insertion sites of a ligament contain the same number of points for all bones. Each insertion point on a bone has a corresponding insertion point on the connected bones. The insertion points are evenly distributed ($\sim 2\text{mm}$ apart) in the anterior (for the anterior longitudinal ligament) and the posterior (for the posterior longitudinal ligament) side of the vertebral body. The number of manually selected landmarks is approximately $1\% \sim 2\%$ of the total number of computed vertices of the entire ligament model.

To compute a ligament mesh, we first connect a single ligament fiber between the corresponding points of two insertion sites. The minimum length path of a single fiber is the shortest path between its two insertion points constrained by the bone structures. As in [46], the constrained path is computed using an optimization method that exploits the distance field representations of the bones for computational efficiency.

The optimization algorithm first computes a linear segment between the two insertion points (p_0 and p_n) of a fiber. We then generate intermediate points ($p_1 \dots p_{n-1}$) at uniform intervals between the two insertion points. The algorithm optimizes the intermediate points to minimize the length of the path through all intermediate points under the constraint that no point is inside any bone model. To ensure efficient computation of the constraints, we use the implicit distance field representation. For any point ($p_{x,y,z}$), the distance-field representation (f) gives the distance (positive if the point is outside the bone surface and

negative if the point is inside the bone surface) between the point and the nearest point on the bone surface. The optimization routine minimizes the following cost function (equation 3.1 in [46])

$$\min_{x_i, y_i, z_i} \sum_{i=0}^{n-1} \sqrt{(x_{i+1} - x_i)^2 + (y_{i+1} - y_i)^2 + (z_{i+1} - z_i)^2} \quad (3.1)$$

subject to $f(x_i, y_i, z_i) > 0, i = 1 \dots n - 1$. Since we keep the intermediate points equally spaced along the path, $(x_{i+1} - x_i)$ is constant. Therefore, the optimization problem reduces to

$$\min_{y_i, z_i} \sum_{i=0}^{n-1} \sqrt{const + (y_{i+1} - y_i)^2 + (z_{i+1} - z_i)^2} \quad (3.2)$$

subject to $f(x_i, y_i, z_i) > 0, i = 1 \dots n - 1$.

We use a sequential quadratic programming (SQP) method (from the high performance NAG library [70], implemented in C/C++) to solve the optimization problem. However, the optimization method is prone to converging towards local minima. To tackle this challenge, we take advantage of temporal coherence and use the computed geometry of a frame to initialize the optimization process of the neighboring frames. We found that this method converged to the correct solution successfully (on average 150 iterations required per fiber per segment of the ligament) for all frames of the motion sequences. The resulting ligament mesh consists of approximately 1400 vertices.

To generate a 3D mesh surface model, we first construct multiple interconnected fibers. Individual fiber paths are computed following the approach described above. We then generate uniformly distributed equal number of points along all computed fiber paths. We perform a custom triangulation on the points to generate the 3D mesh of the ligament (Figure 13b).

3.2.4 Model Analysis

The 3D ligament meshes generated using our method could be used as input geometries to joint simulation methods such as the FEM. However, even this simple mesh representation has further uses. We show how a quantitative analysis on the 3D surface meshes can be used to gain insights into the underlying ligament geometry and to extract useful measurements for comparative analysis.

We compute average length and average deflection of the 3D surfaces for all frames. Average length of a 3D surface model gives us a lower bound on the ligament length in that posture. Similarly, deflection analysis of ligaments during motion may indicate a potential unhealthy condition of the joint. We also analyze the distance between fibers of the surface meshes to see if the fiber paths bundle together along the width of the ligament models.

To compensate for subject-specific variation across subjects, we designed normalized measurements. We manually identify a set of frames from the motion sequences which resemble most a neutral posture. Measurements of all the remaining frames are normalized with respect to the measurements of these reference frames. These normalized measurements indicate changes in the ligament geometry in percentage rather than absolute values, and thus enable comparative analysis among subjects.

3.3 RESULTS AND VALIDATION

Following approval from our Institutional Review Board (Pitt IRB), we applied our method on real clinical data captured from two subjects - one with healthy cervical spine and the other with a single level anterior fusion in vertebrae C5-C6. The fusion patient was tested between 6 and 7 months post surgery. We selected one healthy and one fusion patient. We selected the two major ligaments [34] of the spine: Anterior Longitudinal Ligament (ALL) and Posterior Longitudinal Ligament (PLL) for our modeling. These continuous ligaments provide the main support in the anterior and the posterior of the spinal column. We extract geometric features from our models and validate the result against literature data. We also compare the ligament models of the two subjects to see how the surgery affects the ligaments.

3.3.1 Ligament Length Analysis.

To compare our models with the literature data, we compute the average ligament length from the reference frames. Because the reference frame is manually chosen to be close to the neutral posture, the average ligament length over the reference frames is an approximation of

the neutral ligament length. In Table 9 we compare the average ligament length over the reference frames with the previously published neutral lengths of ligaments computed through experimental methods on cadavers [76]. Ligament length from our models is in agreement with previously published results (within the first standard deviation of our measurements for both ligaments).

Ligament	Avg. neutral length from our models	<i>in vitro</i> avg. length from literature
ALL	19.7±1.11	18.8±1.04
PLL	17.69±2.27	19.0±1.04

Table 9: Average neutral ligament length computed from the mesh models against *in vitro* results from medical literature[76].

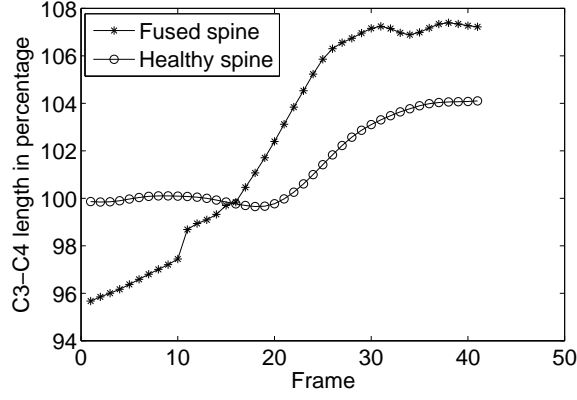
Segment	Normalized length variation range(%)		Deflection variation range(mm)	
	Fusion	Healthy	Fusion	Healthy
C3-C4	12%	4%	0.9mm	0.8mm
C4-C5	12%	10%	0.5mm	0.9mm
C5-C6	4%	9%	0.2mm	1.1mm
C6-C7	9%	3%	0.1mm	0.05

Table 10: PLL mesh model comparison (normalized length and deflection variation) between the fusion and healthy datasets.

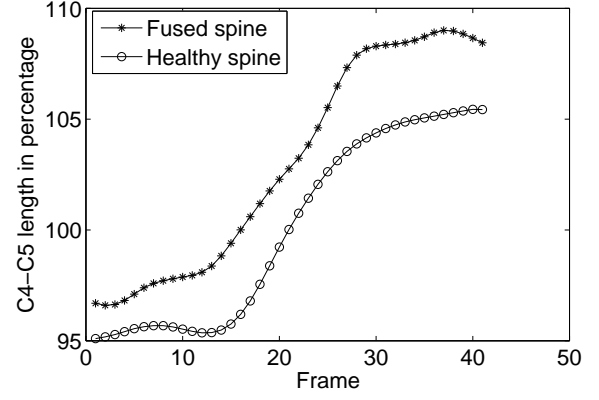
3.3.2 Comparative Analysis.

Normalized length and deflection of ligaments per segment (i.e. C3-C4, C4-C5, C5-C6 and C6-C7) were used to compare the models generated for the two subjects.

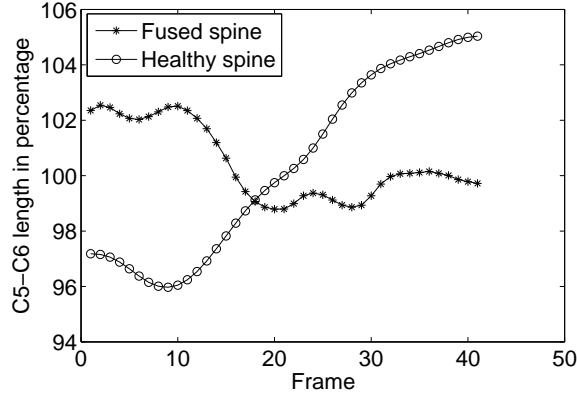
Anterior Longitudinal Ligament (ALL). Comparison on ALL can be done for one segment (C3-C4) because the fusion surgery removed ALL from the fused bones. We found that the ligament features of the two subjects vary similarly. For both subjects, normalized



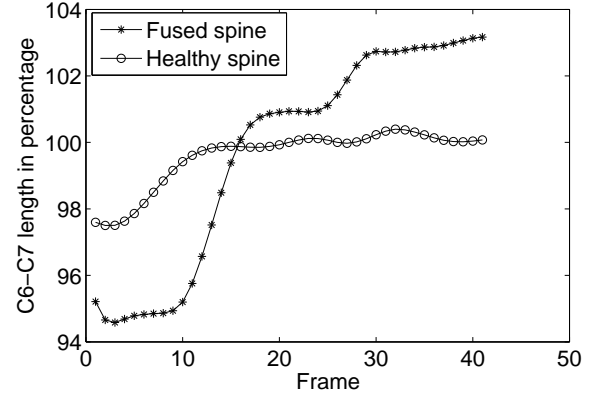
(a)



(b)



(c)



(d)

Figure 16: Normalized length analyses across the dynamic motion range(from full extension to full flexion) for each segment of the spinal posterior ligament band for a fusion and a healthy subject. C5-C6 shows the most significant change in the length variation across the motion (c). Other segments of the spine compensate for the fusion.

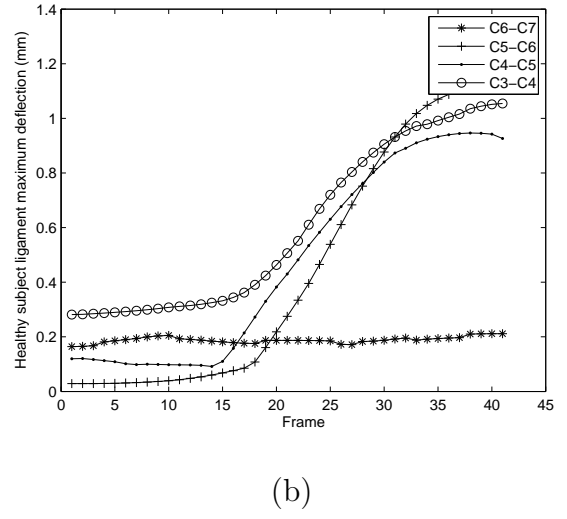
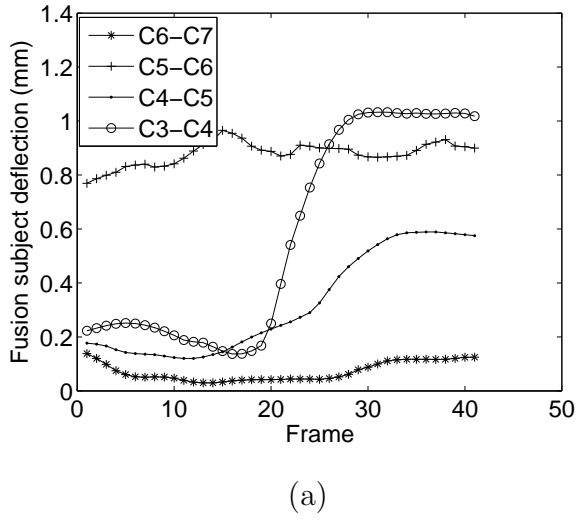


Figure 17: Maximum deflection analyses across the dynamic motion range (from full extension to full flexion) for each segment of the spinal canal for a fusion and a healthy subject. Because of the fusion, C5-C6 ligament segment shows significant difference in the deflection. Deflection differences for the other segments are not significant.

length variation is within 18% of the reference frame length and the deflection variation is within 0.2 mm range.

Posterior Longitudinal Ligament (PLL). Normalized length analysis and deflection measurements show an interesting pattern for PLL ligament segments (Table 10). We found a significant difference between the two subjects in normalized length variation and deflection over the range of motion for the C5-C6 fusion segment (Figure 16c). For the fusion subject, other segments (i.e. C3-C4, C4-C5 and C6-C7) show increased length variation indicating more movement in these segments to compensate for the fusion in C5-C6 (Figure 16). In a healthy spine, C4-C5 and C5-C6 segments account for more motion than the C3-C4 and C6-C7 segments. Deflection variations of the segments other than C5-C6 cannot be considered significant because our bone models are created from CT images with resolution 0.3mm~0.5mm (Figure 17).

Inter-fiber Distance Analysis. We computed the inter-fiber distances for the longitudinal ligaments across the motion sequence. Change in inter-fiber distances is an indication of interaction of ligament fibers perpendicular to the fiber direction. We did not observe any bundling of fibers (Figure 18) and significant change in inter-fiber distances (0.05% ~ 3.5% of the average width). This agrees with the anatomic knowledge that longitudinal ligament fibers are mostly oriented parallel to the length of the spine and provide almost no mechanical support perpendicular to the fiber direction.

3.3.3 Feedback from Domain Experts.

We presented our models and the result analysis to two spine surgeons and one bio-mechanical engineer. We asked about the clinical significance and potential applications of the our method. The experts commented that our tool has potentials for designing better diagnosis measurements for spine related conditions such as cervical radiculopathy (ligaments pinching into the spinal cord and causing pain and neurological disorders). As a future work, the experts suggested modeling the interaction between ligaments, spinal cord and the intervertebral discs. The experts are looking forward to applying the tool in a large-scale experiment on both healthy and symptomatic spine joints.

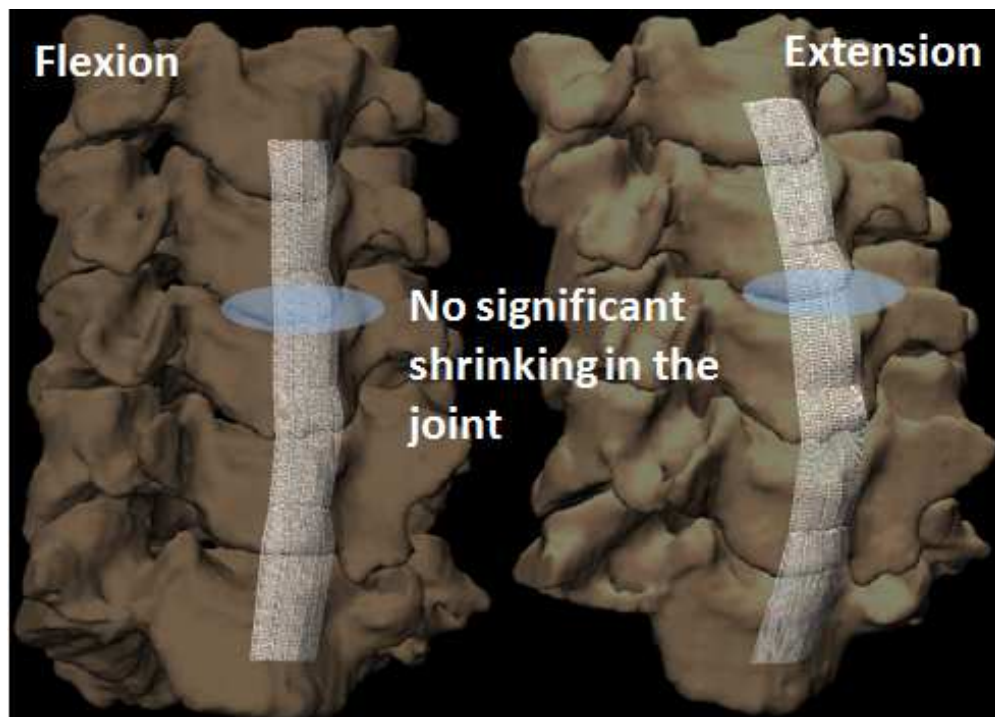


Figure 18: In our model ligament fibers do not bundle together during motion indicating minimum interaction longitudinally among fibers.

3.4 DISCUSSION AND CONCLUSION

In this chapter we have presented a semi-automated technique for dynamic modeling and analysis of the spine ligaments. The proposed method is unique to achieve significant automation in the modeling process while enabling dynamic analysis to gain insight into the spine dynamics.

The results show that our image-to-mesh models are in agreement with measurements from experimental *in vitro* methods. Comparative analyses between a healthy and a fusion patient show smaller variation of ligament lengths in the fusion segment and larger variations in the surrounding segments. This indicates that our method can capture anatomically significant subject-specific features of ligaments. The automation of the method (98% reduction in landmark point selection) is a big advantage compared to a manual method. Because of the automation and non-invasiveness, the method can be applied in control group studies to get insights into ligament related diseases and injuries.

Note the measurements are in general agreement with reports from *in vitro* studies, despite anatomical variation, as well as variation in procedural length definition across studies; for example, Przybylski et al. [58] define lengths as the span over inter-vertebral discs, resulting in shorter reported lengths.

The optimization algorithm of our tool is fully automatic and requires approximately 5 minutes per frame in a standard PC (2 GHz processor, 4.00 GB RAM). The ligament geometries are pre-computed and then loaded for real-time visualization and analysis. Using parallel computation can significantly reduce the runtime of the optimization.

Our modeling pipeline requires the identification of insertion points and reference frames. This step requires less than an hour per subject (less than 50 minutes for locating insertion sites of all bones and less than 5 minutes for identifying neutral frames within the motion sequence). Please note that these manual steps are performed to the best of the user's capability. No *in vivo* approach exists today for accurate identification of these features for spine.

Our method successfully handles geometric variations of different vertebral bodies and the geometric changes due to fusion. In terms of limitations, ligament insertion sites may

vary across human subjects and thus influence our mesh reconstruction. This type of insertion data, respectively ligament geometry cannot be currently acquired non-invasively for the spine. Furthermore, validation of the reconstructed meshes against *in vitro* data is challenging because ligament loading conditions and their properties change significantly when the ligaments are removed from the joint.

Our ligament models are 3D surfaces rather than 3D structures. We made this assumption because the thickness of longitudinal ligaments is not directly constrained with bone geometries and positions. In addition, limited resolution of the bone geometry and the accuracy level of motion information used in our method would make the small measurements of the ligament thickness (generally < 1.5 mm) insignificant.

In our approach, we have used a hierarchical model-based motion reconstruction method which has been previously reported to have sub-millimeter accuracy for *in vivo* cervical spine studies. Using alternative, lower accuracy motion reconstruction methods may affect the quality of the mesh model reconstruction.

In future, we would like to validate our method using cadaver data or by applying the method to larger joints like the knee, where MR images can capture the joint ligaments. However, validation of the reconstructed models against in-vitro data would be problematic because the ligament soft-tissue deforms significantly when dissected due to the change in loading conditions. Thus, in-vitro validation would lead to inaccurate measurements.

We would also like to analyze the uncertainty due to the identification of insertion sites and the references frames manually. Another direction of future work would be developing an automated technique to estimate the ligament insertion sites and the reference frames using anatomical features. This approach would further reduce the manual labor required for the tool.

Currently the mesh optimization run-time is a hindrance for the tool to be clinically relevant. However, the issue can be easily resolved by using more processors or parallel implementation of the algorithm or a better optimization scheme.

In conclusion, we have designed and developed a semi-automatic method to reconstruct 3D ligament meshes from captured multimodal images of joints. The method is *in vivo* and non-invasive, and it allows subject-specific dynamic analysis of spine ligaments. The method

generates anatomically accurate models and enables comparison between different subjects.

Because the method uses *in vivo* data, it can be applied in large scale experiments for validating hypotheses related to spine ligament injuries and diseases. The generated mesh models can be used as geometry inputs to FE analyses of spine. Because the manual processing is not significant, the tool has potentials for real clinical scenarios. The tool can also be very useful for biodynamics and orthopedic research.

4.0 CARTILAGE MODELING

Due to the mechanical and pathological significance, it is important to include the cartilage for accurate modeling and simulation of articulations. The cartilage acts as a shock absorber, force distributor and a cushioning surface allowing low-friction gliding of bones in the joint space during motion. Damage to the cartilage tissues caused by injuries or diseases is the main reason of osteoarthritis. In-vivo dynamic analysis of articular cartilage can help us to correlate different diseases with the cartilage and thus can significantly improve our understanding of the diseases and their treatment methodologies.

However, modeling the cartilage tissues poses several significant challenges. Soft cartilage tissues deform during motion. Accurate geometric modeling of the deforming structure poses a significant challenge mainly due to two reasons 1. 3D imaging techniques such as CT/MRI cannot capture soft-tissue geometry dynamically during motion and 2. cartilage structures are often very thin and may not be captured by the CT/MR images. Existing cartilage modeling techniques are mainly manual which oversimplifies the geometric structure e.g. fixed size extrusion of the bone surface. Therefore, an automated and dynamic modeling technique for cartilage is a significant challenge for modeling of articulations.

In this chapter, we propose an image-based semi-automated computational approach for dynamic modeling of the articular cartilage. The key contribution of our method is the automation of the modeling process while maintaining high anatomic accuracy for dynamic analysis of the inter-vertebral discs. Our method infers the cartilage geometry computationally from multimodal images. The method also quantifies the deformation of the cartilage during motion. Finally, we propose several subject-independent measurements of the cartilage geometry for inter-subject comparison. Comparison between a healthy and a fusion subject shows that the reconstructed models can successfully capture subject-specific features

of the cartilage and the impact of the fusion surgery with respect to a control subject.

4.1 RELATED WORK

A simple approach of cartilage modeling is a fixed height extrusion of bones in the joint space. This approach is widely used in the finite element analysis of cartilaginous soft-tissues [50]. Essentially, cartilage is represented as a fixed height volumetric mesh in this approach. The simplified geometrical structure allows more details analysis of material properties. However, the lack of accuracy in the geometric structure and the inability to model the large deformation that can happen during motion to cartilaginous tissues such as intervertebral discs are the two major limitations of this approach.

Computational approaches based on the bone geometry and inter-bone joint spacing can produce a variable height cartilage model [15, 46]. Existing such methods produce cartilage models from 3D images captured either in a static [15] or in a quasi-static [46] manner. However, both approaches have the limitation that the generated models will be biased by the postures of the captured images. Image-based approaches [61] have been developed to model cartilaginous intervertebral discs. In this approach, the intervertebral disc surface is extracted from 3D images such as MRI and then modeled as a mesh. However, the approach has been used only for the static modeling.

Cartilage behavior can be modeled either as a rigid solid [50, 35] or as a deformable solid [74, 24]. A rigid body representation cannot simulate the cartilage deformation that happens during motion in the joint contact space.

An array of methods [22] exist for modeling deformable solid behavior. Techniques developed in computer graphics such as mass-spring systems and particle systems are computationally efficient. However, modeling complex characteristics such as volume preservation can be difficult using these methods. Simulation methods from continuum mechanics such as finite element methods (FEM), finite difference methods and finite volume methods can be used to model a deformable solid [22]. However, these approaches are computationally expensive for modeling complex articulations. For efficient computation, Muller et. al. [52]

proposed the domain embedding technique in which the object surface is embedded into a cuboid element voxelization. However, maintaining topological changes specially with heterogeneous elements can be challenging in this approach [53, 54].

In recent works [46, 57], quasi-rigid contact through local and analytic models have been proposed. Both approaches used a mesh-free representation of the volume. The idea is to preserve the overall volume by preserving the local volume surrounding the contact region. Cartilage is assumed to be incompressible here.

4.2 MATERIALS AND METHODS

We propose a semi-automatic computational approach based on dynamic motion information and geometry of vertebrae for the geometric modeling of inter-vertebral discs. Vertebral bodies directly constrain the inter-vertebral disc from the superior and the inferior direction. Therefore we propose to reconstruct the inter-vertebral disc geometry using bone position, orientation and geometric structure. First, we infer the 3D geometry of the disc for each posture of the bones across the entire range of motion. We then analyze the deformation of the reconstructed models to extract and infer geometric features of the cartilage. Finally, we obtain anatomically relevant measurements for subject-specific and inter-subject analysis of the joint cartilage.

4.2.1 Data Acquisition

The method we propose for inter-vertebral disc modeling utilizes vertebrae geometry and motion information. We use the data acquisition system described in chapter 2 to acquire both vertebrae geometry and 3D dynamic motion. To obtain 3D images of the spine, we use a CT scanner. The CT images are then segmented by domain experts using 3D medical imaging software. We capture high-resolution dynamic radiographs with a stereo X-ray (DSX) system (Fig. 7a). The dynamic radiographs are captured at a certain angle during motion. The DSX system allows high resolution imaging (1800x2400 pixel resolution) at up

to 500 frames/sec with 14-bit dynamic range. Please see section 2.2.5 for farther details of the system.

4.2.2 Bone Motion Reconstruction

we reconstruct 3D dynamic motion of vertebrae by applying a highly accurate model-based method 2. The method uses the segmented volumetric images of the bones of interest and the dynamic radiographs captured in the biplane x-ray system. In this motion extraction method, we reconstruct computationally a virtual model of the DSX imaging system and then we simulate X-rays through the bone models to produce a pair of digitally reconstructed radiographs (DRRs). By manipulating the bone models within the virtual DSX system, we can generate pairs of DRRs for any bone position and orientation. Using image similarity a 85/15 weighted average of cross-correlation and gradient correlation between the actual radiographic image pairs and the DRRs, we then optimize the position and orientation of each bone to identify the configuration that provides the best match, thus determining the position of the actual bone in the space. The hierarchical model-based method leverages spatial and temporal coherence and the hierarchical overlapping structure of vertebrae to reconstruct the motion automatically and accurately. The method has shown to achieve sub-millimeter accuracy (average 0.3mm translation and 1° rotation) for in-vivo spine data. Please see chapter 2 for the details of the method.

4.2.3 Bone Geometry Representations

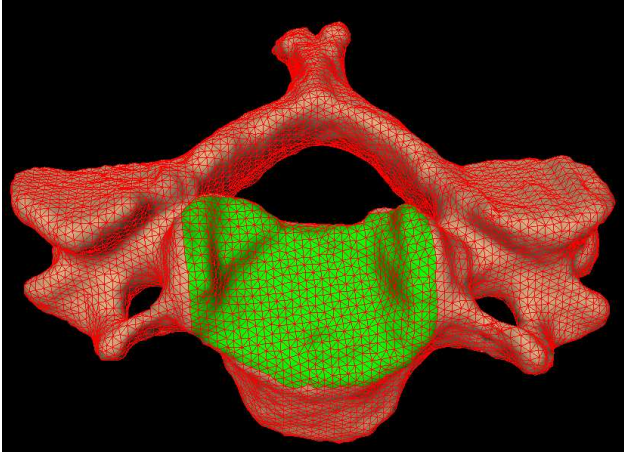
We use two representations for the geometry of the bones: a distance-field representation for faster computation in the inter-bone joint space and an explicit mesh representation visualization. First, the bone models are segmented with high accuracy by domain experts, and no smoothing or simplification is applied to the models. The resulting mesh models (10k-20k vertices and 20k-50k faces per vertebra) represent the bone surface with high accuracy. The mesh representation (Fig. 15a) is used for manually selecting the region of interest as discussed in the next section and for visualization. The implicit distance-field (Fig. 15b) representation (**DFS**) of the bone surface enables fast computation of joint-space distances

(Fig. 15c) such as the distance between an arbitrary point in the joint and the nearest bone surface. The distance-field representation allows us to find the closest point (\mathbf{y}) and the distance ($\pm d$) on a bone surface from any arbitrary point (\mathbf{x}) efficiently.

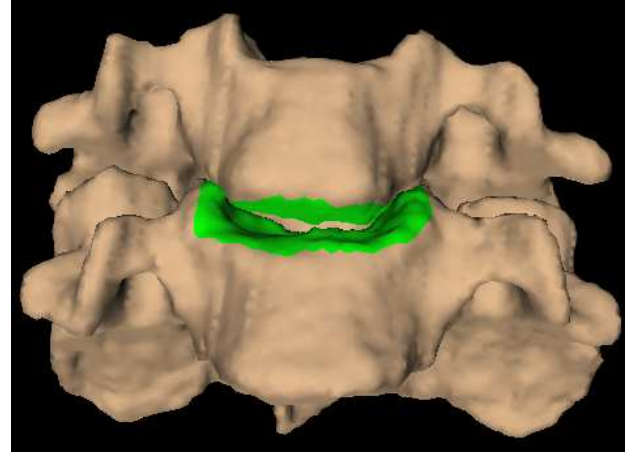
$$cp(\mathbf{x}, \mathbf{DFS}) = \mathbf{y}$$

$$cpd(\mathbf{x}, \mathbf{DFS}) = \pm d$$

cp and cpd denotes the closest point and the distance to the closest point function. Using the distance field representation (\mathbf{DFS}), these function return the closest point and its distance very efficiently. A positive value indicates that the point is outside the bone surface and a negative value indicates that the point is inside the bone surface.



(a)



(b)

Figure 19: Manually marked initialization region for the cartilage map location of a vertebra (a). An intervertebral disc is located between the superior and inferior cartilage region (b).

4.2.4 Identifying Cartilage Map

To reconstruct the 3D cartilage geometry, we need to identify the cartilage map location—the bone surface where cartilage is located. We define cartilage map as the bone surface in the joint space where two bones come close to each other below a certain threshold across the range of motion.

We introduce a semi-automated technique to reconstruct the cartilage map location. First, we interactively identify the joint surface of each bone using mouse click and drag in a custom software. Figure 19.b shows the manually marked region in green for both the superior and the inferior vertebrae of the joint. These manually marked regions serve as an initialization for the cartilage map location.

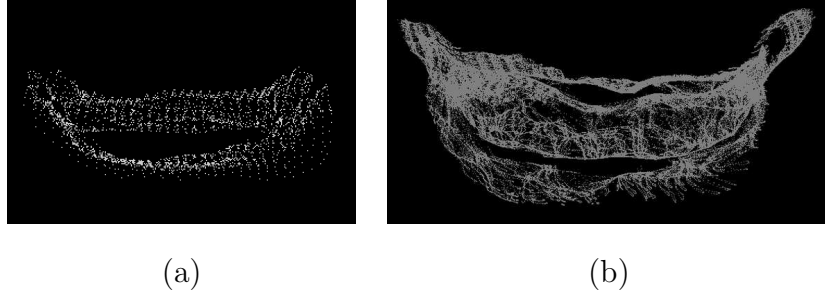


Figure 20: A manually marked region (Fig. 19) is filtered automatically using the joint space distance between two vertebrae. The resulting filtered point set for a single frame (a) denotes the region where the distance between the two bones are within a certain threshold. The union of filtered points from all frames approximates the final cartilage map location (b).

Next, we reconstruct the cartilage map location based on inter-bone distance by applying an automated method on the two selected regions. For each region we find the set of points (P_{sup}, P_{inf}) belonging to the region. For each point set we compute the closest points on the other bone surface using the distance-field information. We filter the closest points by selecting only those which are within a certain distance threshold. Figure 20a shows the computed set of closest points for a single frame of the motion range. We apply the same procedure for all the frames of the motion range and take union of all the closest point sets. Figure 20b shows such a union of all closest points (Sup_{cp} and Inf_{cp} for the superior and the inferior plane).

$$Sup_{cp} = \bigcup_{i=1}^n cp_i(P_{inf}, \mathbf{DFS}_{sup})$$

$$Inf_{cp} = \bigcup_{i=1}^n cp_i(P_{sup}, \mathbf{DFS}_{inf})$$

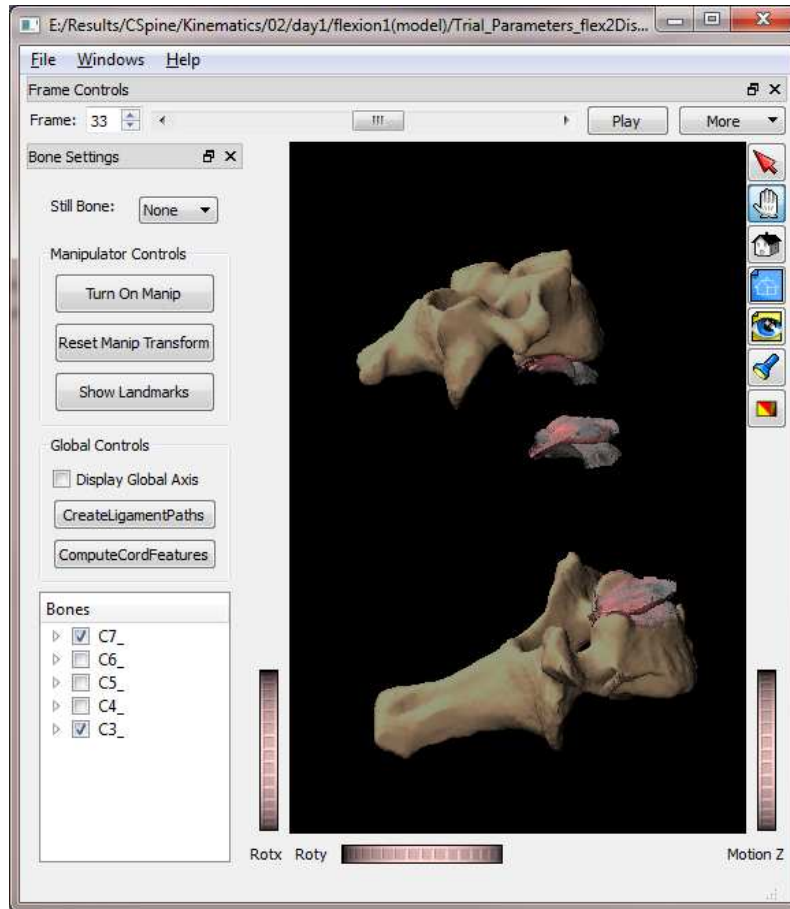


Figure 21: Reconstructed surface model of the minimum height disc space from the fusion patient. The image shows models of the C3-C4, C4-C5 and C6-C7 segments. C5-C6 segment is excluded due to the fusion surgery.

These sets of closest points (Sup_{cp} and Inf_{cp}) defines the cartilage map location. The distance threshold is empirically determined based on the dataset.

4.2.5 Cartilage Modeling and Analysis

The superior and the inferior closest point sets (Sup_{cp} and Inf_{cp}) define the two end plates of an inter-vertebral disc. They work as a point cloud model of the intervertebral disc. We use these point sets to estimate geometric features of the cartilage and to extract a minimum constraint disc model. The purpose of the minimum height disc (Fig. ??) is to quantify the height of the disc that is present across the entire motion range and to measure the deformation of the disc with respect to this minimum height. Therefor, the minimum disc height at any point (\mathbf{x}) is defined as the minimum distance of all the closest points across the entire motion range

$$MinDiscHeight(\mathbf{x}) = Min_i^n(cpd_i(\mathbf{x}, \mathbf{DFS}))$$

We reconstruct the geometry of a minimum height disc by extruding the bone surface along the closest point direction. The amount of extrusion for any frame (i) is the difference between the closest point distance and minimum disc height distance.

$$Extrusion_i(\mathbf{x}) = cpd_i(\mathbf{x}, \mathbf{DFS}) - MinDiscHeight(\mathbf{x})$$

The extrusion at any frame quantifies the amount of deformation in that frame.

From the point cloud model of the disc plates, we extract the following geometric features of the disc across the entire motion range: 1. disc height in the anterior, center and posterior regions (add references and a picture if possible identifying these regions), 2. normalized disc height and 3. disc radius. For the disc height computation, we automatically identify the three regions. First, we compute the three principal axes (lateral, anterior-posterior and superior-inferior shown as X, Y and Z axes in Fig. 22) direction and the geometric center from the point cloud. Then we select the points into the anterior-posterior direction and divide them in three equal regions - anterior, center and posterior. We compute the average distance between the selected points in the superior and inferior plane region.

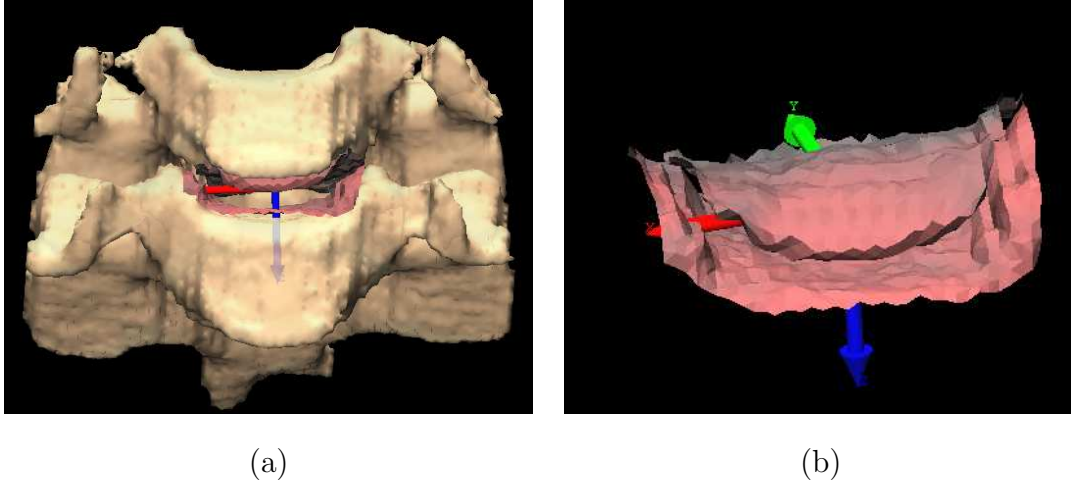


Figure 22: A reconstructed minimum height disc (a) in the joint space of two vertebrae. A minimum height disc color-mapped with the disc deformation (b).

The disc height measurement can significantly vary between subjects. For inter-subject comparison we develop a subject-independent normalized disc height measurement. We manually identify a set of frames from the motion sequences which resemble a neutral posture. Disc-height of all the remaining frames are normalized with respect to the disc-height of these reference frames.

Disc Height in mm (mean, std. dev)		
	Anterior	Posterior
C3-C4	(4.34, 1.18)	(2.78, 0.93)
C4-C5	(3.94, 1.37)	(2.45, 0.79)
C6-C7	(3.55, 0.76)	(2.46, 0.59)

Table 11: Disc height measurements from a cadaver study reported by Lu et. al. [42]

Disc Height in mm(mean,stdDev)				
	Control Subject		Fusion Subject	
	Anterior	Posterior	Anterior	Posterior
C3-C4	(5.06, 0.07)	(2.48, 0.01)	(4.32, 0.05)	(2.82, 0.11)
C4-C5	(4.92, 0.01)	(3.1, 0.02)	(4.9, 0.06)	(2.69, 0.05)
C6-C7	(5.03, 0.03)	(2.71, 0.01)	(4.09, 0.04)	(2.79, 0.1)

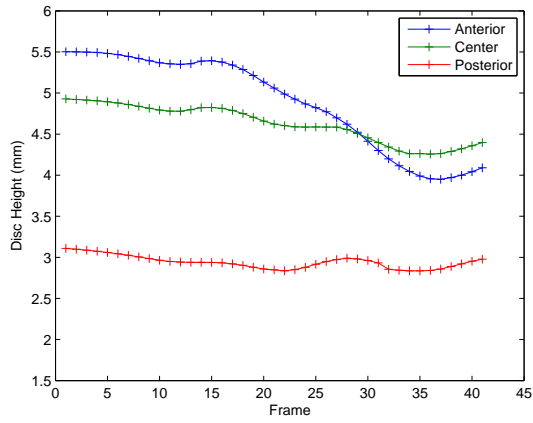
Table 12: Disc height measurements from our reconstructed point cloud models.

4.3 RESULTS AND VALIDATION

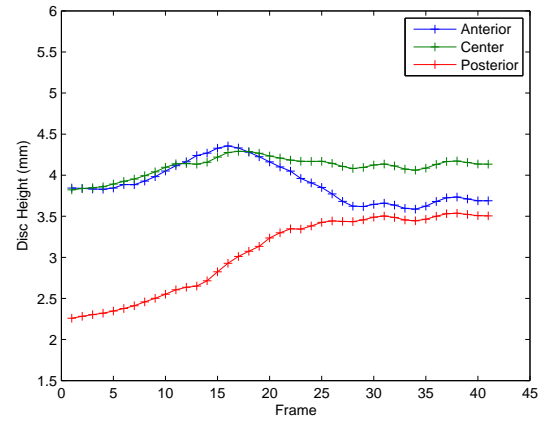
We applied our method on real clinical data captured from two subjects - one with healthy cervical spine and the other with a single level anterior fusion in vertebrae C5-C6. The fusion patient was tested between 6 and 7 months post surgery. We selected one healthy and one fusion patient to see how the surgery affects the inter-vertebral disc and to validate that our method is applicable for inter-subject comparison. We built and analyzed cartilage models for three joints C3-C4, C4-C5 and C6-C7. C5-C6 was excluded due to the fusion surgery. We analyze the cartilage models with respect to disc height, normalized disc height, minimum disc height, disc deformation and disc radius.

4.3.1 Disc Height

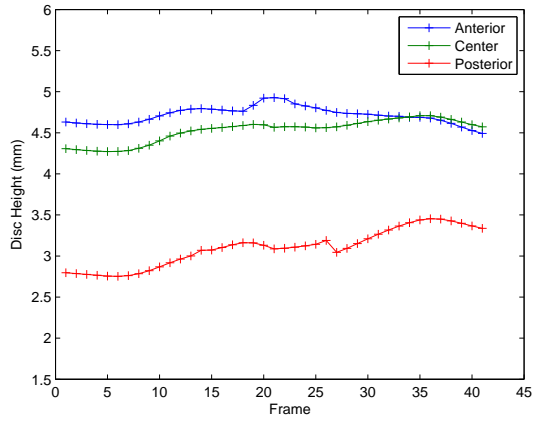
To validate our results, in Table 11 and Table 12 we show disc height measurements from the literature and our models. Lu et. al. reported average disc height in a neutral position from a study based on 20 cadavers. We report the average of disc height in the selected neutral frames for each subject. Our computed disc heights for both subjects are within the first standard deviation of the literature data. In addition, both the literature and our computed results show the pattern that the average anterior disc height is greater than the posterior disc height.



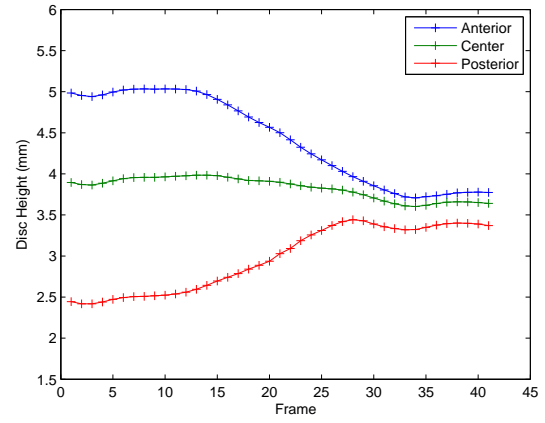
(a)



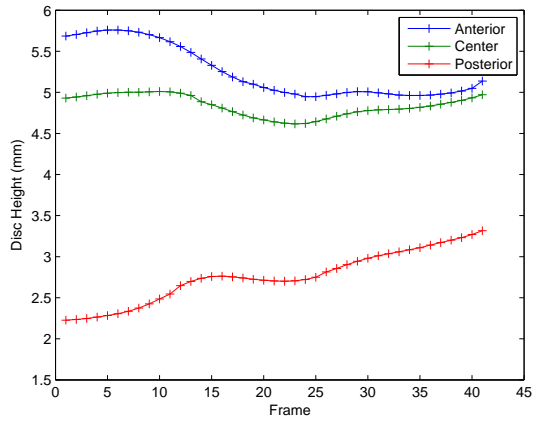
(b)



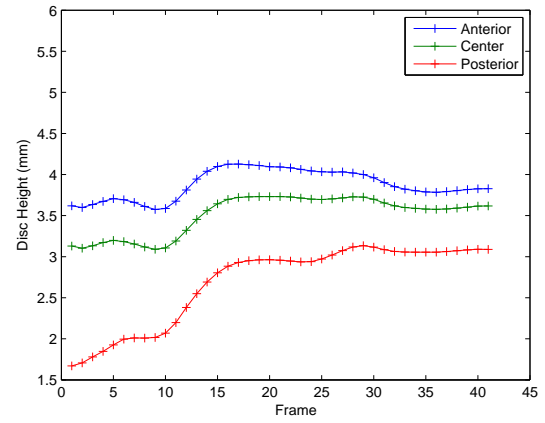
(c)



(d)

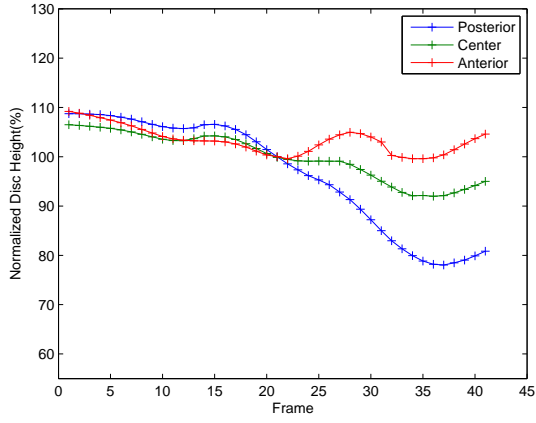


(e)

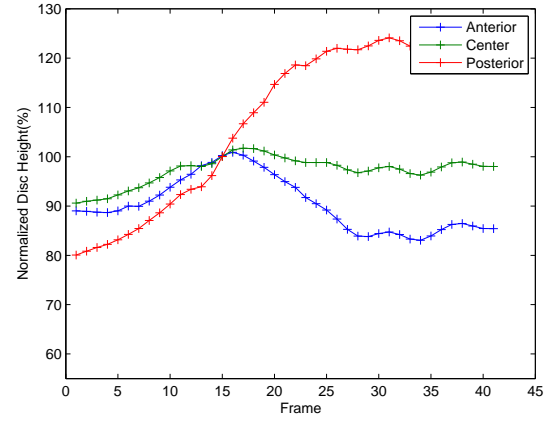


(f)

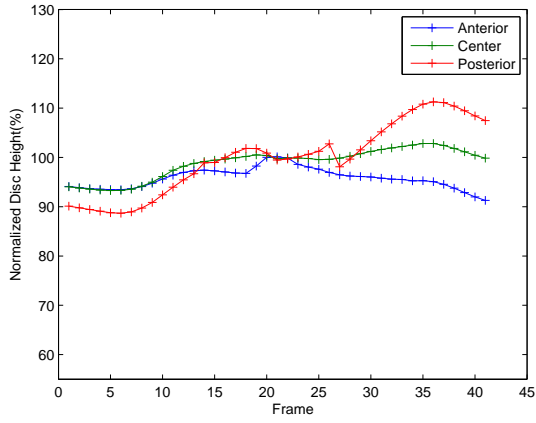
Figure 23: Disc height measurements for the control subject ((a), (c) and (e)) and the fusion subject ((b), (d) and (f)). The first and the last frame corresponds to full extension and full flexion.



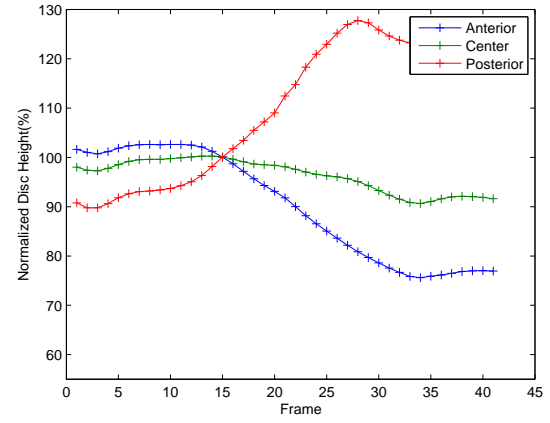
(a)



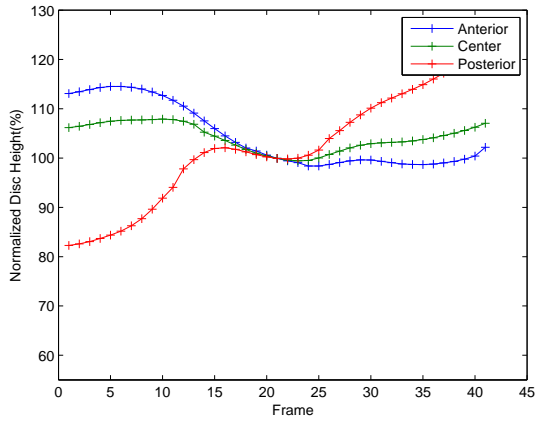
(b)



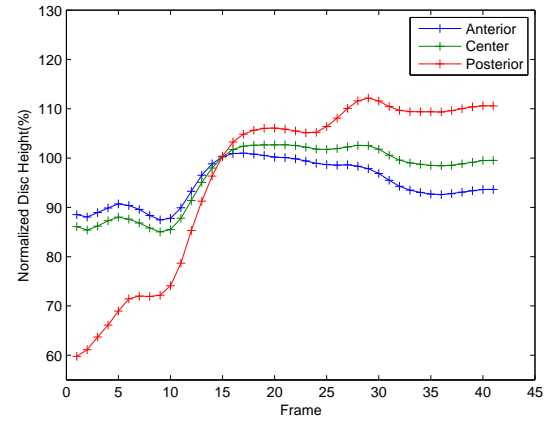
(c)



(d)



(e)



(f)

Figure 24: Normalized disc height measurements (in percentage w.r.t. to the neutral height) for the control subject ((a), (c) and (e)) and the fusion subject ((b), (d) and (f)). The first and the last frame corresponds to full extension and full flexion.

To analyze the disc height variation during motion, in Fig. 23 and Fig. 24 we plot the disc height against the frame sequence. Figure 23 shows the absolute disc height in mm and Fig. 24 shows the normalized disc height with respect to the average neutral frame height. Absolute disc height is a good measurement to see how the disc height changes during motion and the regional difference for a specific disc. For example, from Fig. 23c we see that the posterior disc height (red curve) is smaller than the anterior disc height (blue curve) for the entire motion range. From the full extension to the full flexion, the anterior disc height decreases while the posterior disc height increases.

The range of disc height variation w.r.t. the neutral frame disc height						
	Control Subject			Fusion Subject		
	Anterior	Center	Posterior	Anterior	Center	Posterior
C3-C4	31%	15%	10%	18%	11%	45%
C4-C5	9%	10%	23%	27%	10%	38%
C6-C7	16%	8%	40%	14%	18%	52%

Table 13: Normalized disc height variation across motion. We noticed that the discs in the fusion subject goes through a greater range of height variation than the discs in the control subject specially in the posterior region and the C4-C5 disc shows greater difference than the other discs.

However, it is difficult to compare between two different subjects or joints with the absolute disc height measurement. We compute the normalized disc height (in percentage with respect to the neutral frame disc height) measurement for inter-subject comparison. From Fig. 24c (control subject, C4-C5) and Fig. 24d (fusion subject, C4-C5), we see that the disc of the fusion subject goes through a greater range of height change (variation along the y axis) than the disc of the control subject. We summarize the range of the normalized disc height variation across motion in Table 13. From the table, we see that the discs in the fusion subject goes through a greater range of height variation than the discs in the control subject specially in the posterior region. For example, the range of disc height variation for the C4-C5 disc in the anterior space for the control subject are 9% and 23% whereas for the

fusion subject 27% and 38% respectively. We think that the C4-C5 discs which is adjacent to the fused C5-C6 joint, goes through a larger range motion to compensate for the lack of motion in the C5-C6 joint. C3-C4 and C6-C7 discs also show greater motion range however, not as much as the C4-C5 disc.

4.3.2 Disc Deformation

To quantify the deformation of the disc during motion, we use the minimum height disc as our baseline. The minimum height disc is a lower bound on the disc height i.e. the disc height during motion at all points is always greater than the minimum height disc. Therefore, deformation with respect to the minimum height disc represents the upper bound of disc deformation.

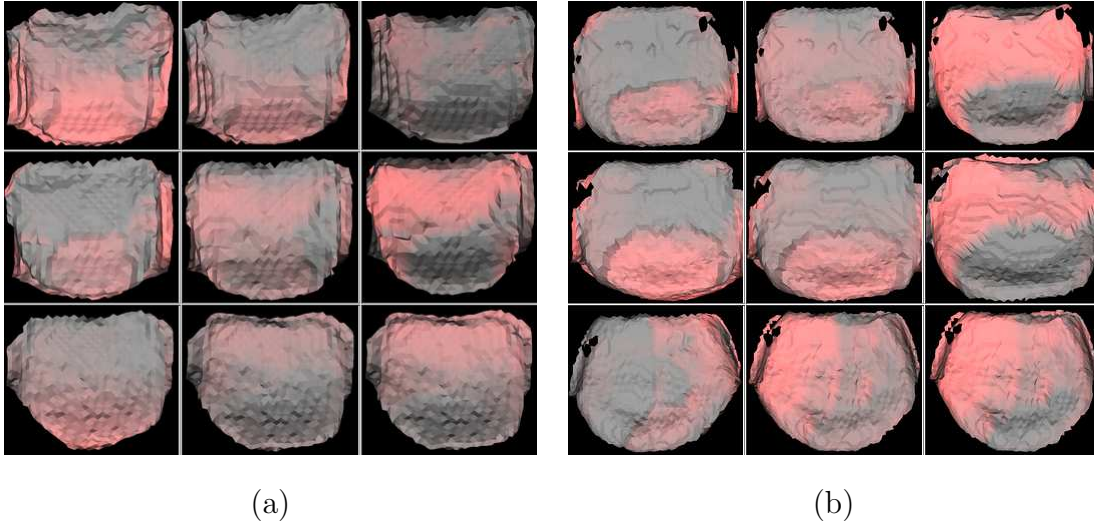


Figure 25: Disc deformation with respect to the minimum height disc colormapped on the minimum height disc for the control (a) and the fusion subject(b). Gray to red represents low to high deformation. From top to bottom, we show C3-C4, C4-C5 and the C6-C7 joint discs. From left to right, we show the colormapped disc in the full extension, neutral and the full flexion posture. For each disc, the lower part corresponds to the anterior and the upper part corresponds to the posterior region.

In Fig. 25 we show the disc deformation as a colormap on the minimum height disc. The figure shows the deformation in the full extension, neutral and full flexion posture for the

the C3-C4, C4-C5 and the C6-C7 joints. Gray indicates low deformation and red indicates high deformation. A quick overview of the image reveals that the discs of the fusion patient (Fig. 25b) shows much more red regions than the discs of the control subject (Fig. 25a). This visualization therefore effectively demonstrates that the fusion subject’s disc go through more deformation than the control subject’s discs during motion.

Maximum disc deformation w.r.t. the minimum height disc (mm)						
	Control Subject			Fusion Subject		
	Anterior	Center	Posterior	Anterior	Center	Posterior
C3-C4	1.37	0.63	0.13	0.86	0.89	1.19
C4-C5	0.39	0.55	0.94	1.36	0.58	0.92
C6-C7	0.56	0.45	0.68	0.43	0.85	1.26

Table 14: Maximum disc deformation with respect to the minimum height disc.

Normalized disc deformation w.r.t. the minimum height disc						
	Control Subject			Fusion Subject		
	Anterior	Center	Posterior	Anterior	Center	Posterior
C3-C4	33.23%	14.15%	3.88%	25.52%	24.69%	45.65%
C4-C5	8.96%	12.40%	29.64%	37.05%	16.47%	33.16%
C6-C7	11.15%	8.86%	20.25%	11.57%	28.70%	60.32%

Table 15: Normalized maximum disc deformation w.r.t. the minimum height disc

In Table 14 and Table 15 we summarize the disc deformation data. Table 14 reports the maximum disc deformation with respect to the minimum height disc over the entire range of motion in the anterior, center and posterior regions. The absolute value of deformation is important to gain insight about the scale of the deformation e.g. from Table 14 we can say that the upper bound of disc deformation for all regions is 1.5mm. For inter-subject comparison, we normalize the deformation by the minimum disc height. Table 15 shows the normalized deformation in percentage. The posterior region shows more deformation than

the anterior and center regions. Similar to the disc height data, the fusion subject shows more deformation than the control subject.

4.3.3 Disc Size

In addition to the disc height, the size of the disc in other dimension is important for overall disc geometry. In Table 16 we show the disc diameters computed from the end-plate point cloud models in both lateral and anterior-posterior direction. We can see that for C3-C7 segments disc radius in the lateral direction is greater than the anterior-posterior direction.

Disc Diameters(mean, stdDev) in mm				
	Control Subject		Fusion Subject	
	Lateral	Anterior-Posterior	Lateral	Anterior-Posterior
C3-C4	(20.32, 0.09)	(15.49, 0.16)	(21.50, 0.08)	(16.41, 0.31)
C4-C5	(18.88, 0.08)	(14.45, 0.13)	(21.95, 0.20)	(17.46, 0.32)
C6-C7	(22.52, 0.04)	(15.77, 0.12)	(24.93, 0.03)	(16.89, 0.17)

Table 16: Disc diameters from our models in the lateral and anterior-posterior direction. The lateral diameter is greater than the anterior-posterior diameter for all C3-C7 segments.

4.3.4 Validation

In addition to the disc-height comparison with the literature data, we presented our models and the result analysis to two spine surgeons, one orthopaedic research and one biomechanical engineer. We also inquired about the clinical significance and potential application of the our method. The domain experts commented that our result analysis agrees with the hypothesis about fusion and its impact on the neighboring joints. A generic application of the tool for spine would be to gain better understanding of inter-vertebral discs and their dynamic geometry. One of the surgeons remarked that the our method can help to compare, track and understand the effectiveness of two treatment methodologies for disc degeneration - disc replacement and fusion. Even though fusion is much more common than

disc replacement, some studies show that the disc replacement works as well and often better than spinal fusion surgery [30]. The experts suggested another potential application can be for the bio-engineer for designing artificial discs. The geometric information of the minimum height disc can be used to design subject-specific artificial discs. At present the discs are manufactured in pre-specified sizes which may not be compatible for every subject. The experts are looking forward to applying the tool in a large-scale experiment on both healthy and symptomatic spine joints.

4.4 DISCUSSION AND CONCLUSION

We proposed a semi-automatic computational approach for subject-specific modeling of the inter-vertebral disc. The novel contribution of the method is achieving automation while allowing dynamic modeling and analysis with high anatomic accuracy of the structure's geometry. The method generates a point cloud model based on the disc contact area on the vertebrae and a minimum-height surface model of the disc. We designed anatomically relevant measurements for analyzing the models. We extracted and compared our results with published results from the literature. The measurements are in general agreement with reports from in-vitro studies, despite anatomical variation. We also performed inter-subject comparison to identify the impact of a surgical procedure on the spine.

The rich geometry of the reconstructed models is a big advantage compared to the traditional manually created simplified models. As shown in this chapter, the reconstructed models can be used to automatically extract anatomically relevant geometric features. The surface model has further application in the FE analysis.

The automation of the method is a big advantage compared to a manual approach for the disc modeling. The manual region identification process requires approximately 10 min per region which is significantly lower than a fully manual approach requiring hours for creating an accurate disc geometry. Due to the automation, the accuracy of the method is also operator independent.

Our method successfully handles geometric variations of different vertebral bodies and the

geometric changes due to fusion. In terms of limitations, dependency on the accurate motion information is a limitation of our proposed method. Inaccurate motion information can lead to an inaccurate disc models. The hierarchical model-based motion reconstruction method has shown sub-millimeter accuracy for *in vivo* cervical spine studies. Using alternative, lower accuracy motion reconstruction methods may affect the quality of the mesh model reconstruction.

In future, we would like to validate our method using cadaver data. However validation of the reconstructed models against in-vitro data would be problematic because the inter-vertebral disc structures deform significantly after dissection due to the change in loading conditions. Thus, in-vitro validation would lead to inaccurate measurements.

In conclusion, we have designed and developed a semi-automatic method to reconstruct geometric models of the inter-vertebral disc from static and dynamic images of the spine. The method allows subject-specific dynamic analysis of inter-vertebral discs. Normalized measurements based on the reconstructed models enable inter-subject comparison.

Because the method is mostly automatic and non-invasive, it can be applied in large scale experiments for better understanding of spine injuries and diseases. The generated mesh models can be used as geometry inputs to FE analyses of spine. Because the manual processing is not significant, the tool has potentials for real clinical scenarios. The tool can also be very useful for biodynamics and orthopedic research.

5.0 SPINAL CANAL MODELING

In this chapter, we present a modeling technique for a passive soft-tissue structure specific to the spine—the spinal canal. The spinal canal provides a pathway and protection for the spinal cord—a soft-tissue structure of the spine which acts as the conduction pathway for nerve impulses between the brain and the rest of the body. Shrinkage of the spinal canal due to injuries or degenerative conditions can cause serious neurological problems. For example, many cervical fusion patients develop adjacent segment disease [31] in which segments adjacent to the surgery require further intervention due to pain. The disease is linked with degenerative conditions in the adjacent segments causing nerve compression and pain.

A subject-specific and non-invasive method for automated modeling of the spinal canal with dynamic motion can provide insight into spine-related disorders. Such a method would enable large scale experiments to obtain a better understanding of healthy spine motion and how the spinal cord is affected by motion. However, due to technological limitations, it is practically impossible to capture 3D dynamic images of the spinal cord soft-tissues during normal, loaded movements.

The most common in-vivo approach for computing subject-specific spinal canal measurements is to manually select landmarks in static 3D medical images [23, 45]. This manual process is time-consuming and is generally used to compute one or a few specific measurements of the canal. It is impractical to construct a detailed geometric model of the canal—which would require hundreds of points—using this approach.

We propose an automated method for constructing a 3D, subject-specific geometric model of the spinal canal using computed tomography (CT) images and reconstructed bone motion information. The novelty of the modeling process is achieving three key characteristics at

the same time — automation while enabling dynamic analysis with high accuracy. Because the spinal canal is constrained by the surrounding vertebrae, we reconstruct and measure geometric features of the spinal canal using the surface geometry, position and orientation of bones over time. This approach builds on recent advances in motion tracking technology, which enable us to reconstruct accurate bone motion automatically from in-vivo images. The resulting subject-specific geometric models of the spinal canal can help domain practitioners to observe the impact of motion on the spinal canal. These models also help surgeons compare subjects with different conditions, and gain a better understanding of the underlying conditions.

5.1 RELATED WORK

The most common technique for in-vivo analysis is extracting anatomical measurements directly from captured images such as Computed Tomography (CT), Magnetic Resonance (MR) or Radiographs [2, 45, 26]. Anatomical features are measured from the captured images by manually selecting landmarks in the images. Due to the manual processing steps, the method is time consuming. In addition, geometric details of the spinal canal cannot be obtained in this approach. For example, an in-vivo method based on manually selected landmarks on bone boundaries has been developed to compute the cross-sectional area bounded by the landmark positions [4]. The method directly uses the manually placed landmark positions to compute the cross-sectional area. Reconstructing 3D geometric models of the spinal canal using this method would require manually placing hundreds of landmarks positions, making the process impractical.

Because the spinal canal deforms significantly during motion, the model needs to be recomputed across the entire range of motion. A geometric model which is constructed by manually selected landmarks and then transformed across the motion, cannot capture the deformation realistically. Therefore, a computational method is essential for accurate modeling and analysis of the spinal canal during motion.

In addition to the in-vivo techniques, accurate spinal canal measurements can be com-

puted directly [56, 16] through in-vitro experiments on cadaver specimens. Detailed 3D models of the canal can be generated using foam fillings and then digitizing the resulting cast [39]. However, because of significant subject-specific variations of the spinal canal features, in-vitro experimental measurements cannot be used to build in-vivo subject-specific geometric models.

In conclusion, no semi-automated or automated technique exists for modeling and analyzing spinal canals during motion from in-vivo medical images, that would also provide sufficient geometric detail.

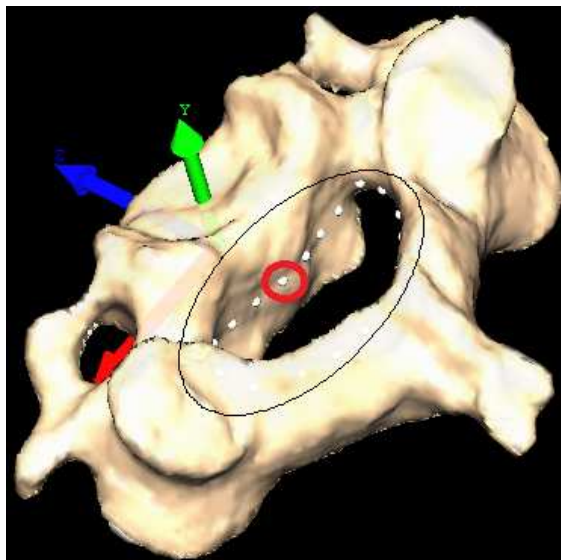


Figure 26: The spinal foramen region (marked in black) and the automatically placed landmarks within it.

5.2 MATERIALS AND METHODS

We present an automated computational method to build subject-specific dynamic models of the spinal canal. The spinal canal contains the spinal cord and the surrounding protective layers. The canal is mainly constrained by the vertebral bodies and two ligament bands (the Posterior Longitudinal Ligament and the Ligament Flavum) along the spinal column.

Because vertebral bodies directly constrain the spinal canal, we use the bone models and their accurate position and orientation information to reconstruct the spinal canal. The dynamic motion information allows us to reconstruct the geometric model of the canal and to capture the changes of the canal during motion.

To generate geometric models of the spinal canal, we first capture 3D volumetric images of bones with a static imaging technique. We then reconstruct the motion information of bones by applying an in-vivo non-invasive model-based method. The method utilizes dynamic 2D X-ray images captured during motion and the bone models generated from the static volumetric images. Next, we compute hybrid representations—meshes and distance-fields—of the 3D bone geometry; these representations have complementary strengths and facilitate fast computation of inter-bone space measurements. We reconstruct spinal canal models during a complete movement sequence using the hybrid representations and motion information of the bones. Finally, we propose geometric features to analyze the spinal canal structure. We describe each step of the pipeline in detail below.

5.2.1 Data Acquisition and Motion Reconstruction

As mentioned above, the proposed modeling method leverages vertebrae geometry and dynamic motion information to reconstruct the spinal canal geometry. We use in-vivo conditions and real clinical data for the spinal canal modeling. We obtain 3D images of the vertebrae with a high-resolution CT scanner and then segment the CT images using a medical imaging software. 3D dynamic motion of vertebrae is reconstructed using the method described in chapter 2. The motion reconstruction method uses dynamic radiographs captured from a stereo X-ray (DSX) system (Fig. 7a). The DSX system can capture high resolution radiographs (1800x1200 pixel) at up to 500 frames/sec. The dynamic radiographs are captured by two X-ray cameras at a certain angle during motion. Section 2.2.5 describes further details of the data acquisition system.

To reconstruct 3D motion information, we applying a hierarchical model-based method (chapter 2) which has shown high accuracy and robustness for spine data. The basic concept of the model-based method is 3D-2D registration i.e. matching the X-ray images

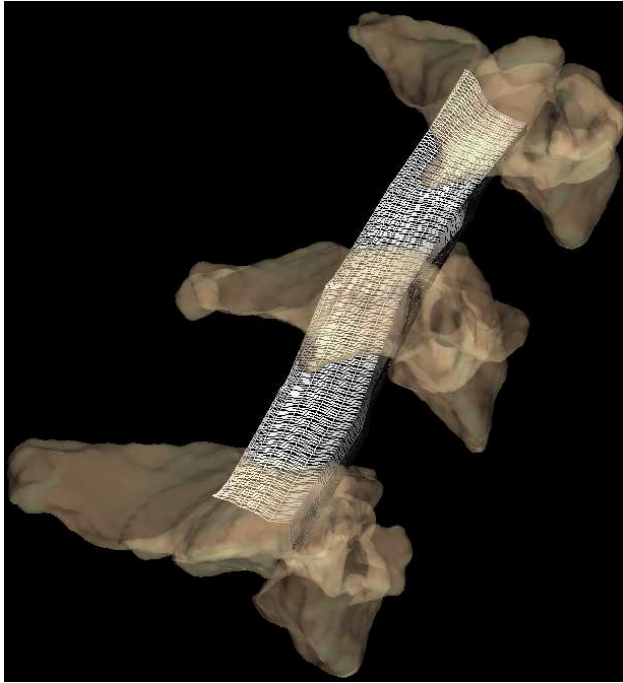
with projected images of 3D vertebrae model. In this approach, a virtual model of the DSX imaging system is simulated from the precise specification of the lab DSX setup. Computer graphics techniques such as ray casting is used to simulate X-rays through the bone models to produce a pair of digitally reconstructed radiographs (DRRs). By manipulating the bone models within the virtual DSX system, we can generate pairs of DRRs for any bone position and orientation. A multi-phase optimization method finds the optimal position and orientation from the search space. The method uses a weighted average of cross-correlation and gradient correlation as the image similarity metric. This process is repeated for each pair of the images in the motion sequence, and repeated again for each bone of interest to yield the 3D position of the joint for the entire movement.

5.2.2 Bone Geometry Representations

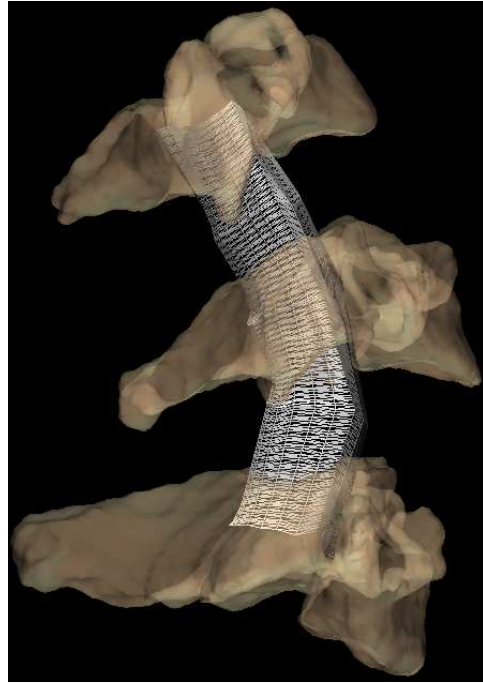
To enable computational modeling of the spinal canal, we compute two representations—explicit mesh representation and implicit distance-field representation—of the 3D bone geometry. The 3D volume images of the spine are segmented with high accuracy by domain experts. We generate the mesh representation by applying the marching cube algorithm on the segmented volume images. The resulting mesh models have 10k-20k vertices and 20k-50k faces per vertebra. The explicit mesh representation (Fig. 15a) is used for automatic landmark selection (as discussed in the next section), visualization and, to validate the correctness of the generated canal models. The implicit distance-field (Fig. 15b) representation enables fast computation of joint-space distances (Fig. 15c) such as the distance between an arbitrary point in the spinal canal and the nearest bone surface.

5.2.3 Spinal Canal Geometry Reconstruction

From the bone representations and the reconstructed motion information, our method reconstructs the 3D geometry of the spinal canal. Because the spinal canal is constrained by the vertebral foramen (vertebral region which constructs the spinal canal as shown in Fig. 26), we place a few (approximately 20) landmark points on the vertebral foramen to model these constraints. we developed an automated method to uniformly place the landmark points



(a)



(b)

Figure 27: The reconstructed spinal canal meshes at two extreme rotations of the neck—full flexion (a) and full extension (b)—during the captured motion sequence. To avoid visual clutter we only show three vertebrae—C3,C5 and C7.

along the vertebral foramen inner circumference. First, we compute the geometric center and the three principal axes of a vertebra from its vertices. The three principal axes (three principal eigenvectors of the covariance matrix of the mesh vertices) align in the lateral, anterior-posterior and the superior-inferior direction. We then compute the intersection of a ray starting from the geometric center and rotating at equal angular interval in the lateral-anterior-posterior plane (ZX plane). Finally, we compute uniformly distributed (~ 2 mm apart) landmark points along the circumference by interpolating intersection points, starting from the anterior-side center of the vertebral body (red circle in Fig. 26). A straight-line visual correspondence is sketched during this step between corresponding landmarks on adjacent vertebrae, to help ensure that the correspondence does not lead to crossings. The spinal canal geometry is then automatically constrained to pass through the landmark points and restricted to not penetrate the vertebral foramen.

To compute the 3D spinal canal geometry, we generate a constrained path between two landmark points of two neighboring vertebrae. First, we identify the starting and the ending landmark points of a path. The constrained path is assumed to be the shortest path between the two landmark points restricted by the bone structures. The constrained path can be thought of as a fiber between the two landmark points. Following [46], we compute the constrained fiber path using an optimization method that exploits the distance field representations of the bones for computational efficiency, as described below.

The method first generates uniformly spaced intermediate points ($p_1 \dots p_{n-1}$) between the two landmark points (p_0 and p_n) of a fiber path. The optimal path of the fiber is computed by transforming the problem into an optimization problem as described in section 3.2.3. We assume that the optimal path is the minimum length path through all intermediate points under the constraint that no point is inside any bone model. The optimization problem reduces to the same problem described in equation 3.1 and 3.2.

Because the interior bone surfaces are smooth, the shortest path approximates well the bounding surface: all shortest path approximation points are less than 0.75 mm (averaged over vertebrae and frames) away from the bone surface and a further 85% of these points are less than 0.5 mm from the bone surface.

To construct the spinal canal model, we first construct multiple interconnected fibers.

Individual fiber paths are computed following the approach described above. Then we generate a uniformly distributed equal number of points along all computed fiber paths. We perform a custom triangulation on the points to generate the mesh model of the spinal canal (Fig. 27). Because the canal structure deforms significantly during motion, we generate mesh models for each frame across the motion using the automated method described above.

5.2.4 Quantitative Analysis

The geometric model of the spinal canal can be used to analyze the effect of motion on the spinal column and the spinal cord. We show how quantitative analyses on the meshes can be used to extract useful measurements for comparative analysis.

To enable quantitative analysis, we compute the volume of the canal and the volume of each functional segment (i.e. C3-C4, C4-C5, C5-C6 and C6-C7) of the canal. We also compute average deflection or bending of the canal for all frames. Volume and deflection analysis during motion may indicate a potential unhealthy condition of the spinal column. In addition, to quantify the change in spinal canal diameter, we compute a center line through the spinal canal mesh and measure the average distances from the centerline to the mesh surface.

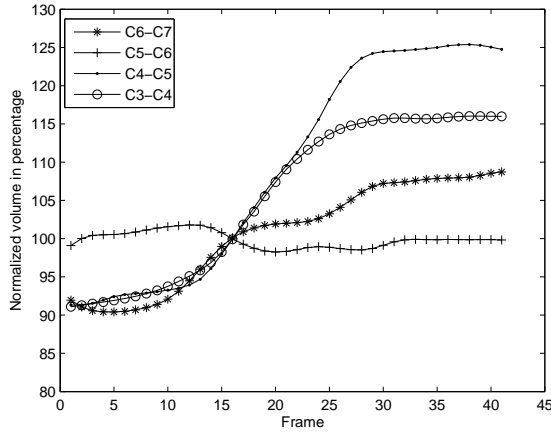
To compensate for subject-specific variation, we compute normalized measurements. We first identify a frame which is the most resembling to the neutral posture. The identification is done manually, since due to subject variability the neutral frame is neither located mid-range of motion nor trivial to detect computationally. To compensate for human error in selecting the reference frame, we take three consecutive frames around the selected frame. We compute volume, radius and deflection for each of these frames, and the mean and standard deviation over this set of frames. We normalize the measurements of the remaining frames (of the motion range) with respect to the measurement of the reference frame. The normalized measurement indicates a change in the spinal canal in percentage rather than in absolute value, and thus enables comparative analysis among subjects.

Selected Frames	Volume(CC)	
	Fusion Subject	Healthy Subject
Reference frames	14.45 \pm 0.15	16.99 \pm 0.11
Entire range of motion	14.99 \pm 0.11	16.89 \pm 0.95

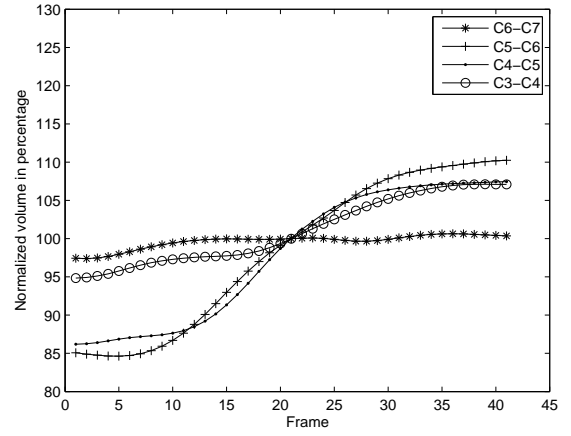
Table 17: Spinal canal volume in the cervical spine (C3-C7) for the healthy and the fusion subject (not normalized). The change in volume is due to subject variation.

Segment	Range of normalized volume change (% of the reference volume)	
	Fusion Subject	Healthy Subject
C3-C4	25%	12%
C4-C5	34%	21%
C5-C6	3%	26%
C6-C7	18%	3%

Table 18: Normalized volume changes for the spinal canal segments. The subjects show different patterns due to the fusion surgery: The fusion subject has significantly lower volume change in C5-C6 region than the healthy patient. The analysis indicates that in the fusion subject the segments adjacent to C5-C6 are compensating for this difference.



(a)



(b)

Figure 28: Normalized volume analyses across the dynamic motion range (from full extension to full flexion) for each segment of the spinal canal for a fusion and a healthy subject. C5-C6 is the least changing volume segment in the fusion patient (a). In contrast, C5-C6 is the most changing segment in the healthy patient (b). Other spinal canal segments of the two subjects are affected differently by the motion.

5.3 RESULTS

We applied the canal modeling method on real clinical data captured from two subjects. We selected one healthy and one fusion patient to validate that the method allows inter-subject comparison—despite subject-specific geometric variations of the spinal canal—and to test whether the fusion surgical procedure affects the spinal canal deformation during motion. One of the two datasets is a healthy cervical spine (47 years old male); the other dataset is a single level anterior fusion in vertebrae C5-C6 (40 years old female). The fusion patient was tested around 6 months post surgery. We reconstruct the spinal canal segment between vertebrae C3 and C7 so that we can see the impact of the fusion surgery.

We compare the spinal canal models of our subjects in terms of volume, radius, and deflection over the range of motion.

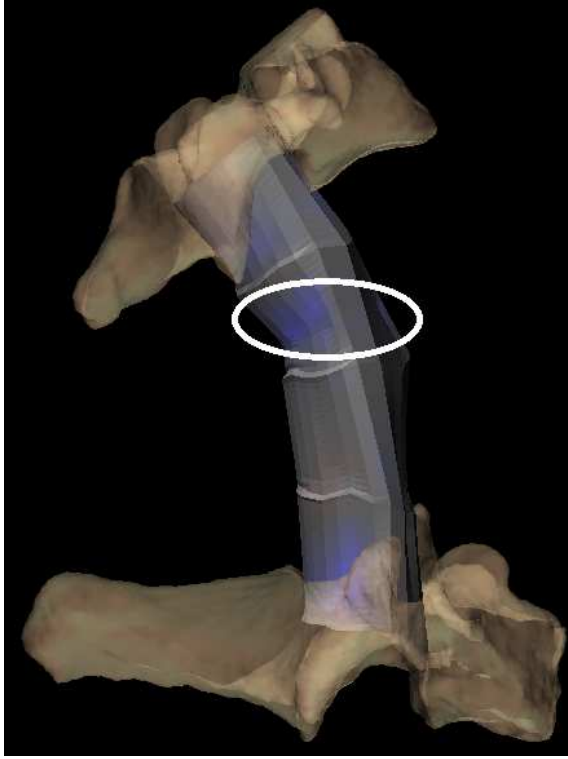
5.3.1 Volume analysis

Table 17 shows the computed volume of the canal models from the two subjects. Average volume for both reference frames and the full range of motion differs significantly between the two subjects indicating the subject-specific variations of the two models.

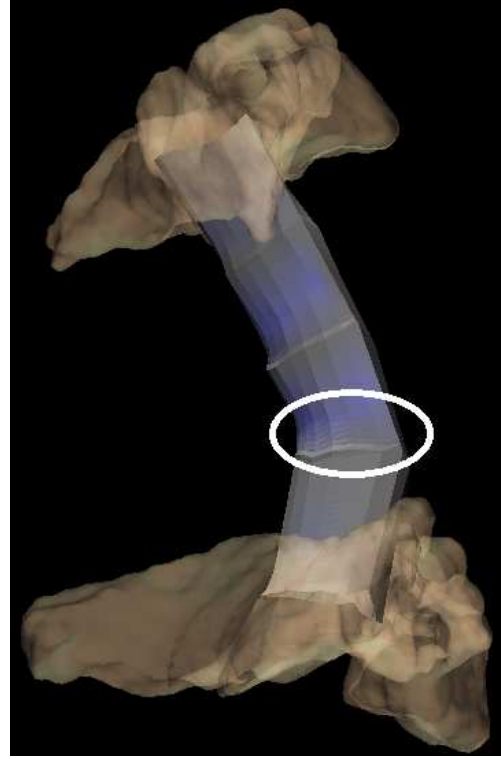
Normalized volume analysis for each segment of the spinal column shows an interesting pattern (Table 18): For the healthy subject, the C5-C6 segment shows a maximum change in volume during motion (Fig. 28); the change of volume decreases for the surrounding segments C4-C5, C3-C5 and C6-C7. In contrast, for the fusion subject C5-C6 shows the minimum change of volume. This significantly affects the volume change pattern for the other segments. C3-C4, C4-C5 and C6-C7 show significantly different change in volume than the healthy subject.

5.3.2 Deflection Analysis

We compute the deflection of the spinal canal model across the range of motion. Analysis shows that the deflection of the fusion patient ($4.2 \pm 0.8 \text{ mm}$) is smaller than the deflection of the healthy subject ($6.3 \pm 1.1 \text{ mm}$). More importantly, visualization of the models shows



(a)



(b)

Figure 29: The difference in the deflection region for the two subjects' spinal canals. For the fusion subject (a), the canal bends towards the top of the spinal column and for the healthy subject (b), the canal bends towards the middle of the spinal column. The change in the spinal canal radius is mapped to the hue (from blue to red; blue for increase and red for decrease in radius) on the canal surface.

the deflections in the two models are at different locations along the canal (Fig. 29). The deflection analysis along with our volume analysis confirms that the effects of motion on the spinal canal of the two subjects are significantly different.

5.3.3 Spinal Canal Radius Analysis

We analyze the radius of the spinal canal to see whether significant shrinkage can be identified in either of the subjects. In addition, we visualize the narrowing of the canal on the spinal canal surface (Fig. 29). We find that the change of radius with respect to the neutral frame is within the range of $\pm 1\text{mm}$ for both subjects. We consider this change insignificant because of the limited resolution of the bone surface models (the CT image resolution is 0.3mm-0.5mm). Our findings agree with the fact that neither of the subjects had symptoms of spinal canal narrowing (spinal stenosis).

5.3.4 Domain-Expert Feedback

To evaluate the clinical significance of our tool, we presented the tool and the results to a bio-engineer and two spine surgeons. The domain-experts stated that the tool could be employed to gain better understanding of spine related conditions such as myelopathy (compression of the spinal cord due to degenerative conditions) and congenital stenosis (compression of the spinal cord due to congenital narrow spinal canal). Spine surgeons generally diagnose these conditions by computing two measurements—the canal diameter, and the ratio between the canal diameter and the vertebral body diameter (Torg ratio [72]) — from the sagittal plane X-ray or volumetric images of the spine. However, these simple measurements are not always effective to understand the complex dynamic nature of the spinal canal and the underlying conditions. The surgeons remarked that the reconstructed geometric models of the spinal canal will facilitate more detailed analyses and thus help the design of effective and accurate measures to diagnose and understand the conditions. The surgeons are looking forward to applying the tool in a large scale experiment on both healthy and symptomatic spine joints.

5.4 DISCUSSION AND CONCLUSION

The result analysis shows that the spinal canal geometric models we generate are capable of capturing subject-specific features of the spinal canal. The method is also capable of handling geometric variations of different vertebral bodies and the geometric changes due to fusion. Additionally, comparative analysis between a healthy and a fusion patient shows interesting patterns in the spinal canal volume and deflections; these patterns capture the effect of fusion and the difference between a normal and a fused spinal canal movement. We did not find any significant narrowing of the spinal canal indicating no spinal stenosis for the subjects.

Because we create the spinal canal models automatically from non-invasive in-vivo medical images, the method can be applied in large scale control group studies to gain insight into spinal canal related diseases and injuries. For example, a large scale experiment with spinal stenosis and healthy subjects can lead to insight into spinal stenosis and its effect on the spinal column during motion.

The optimization algorithm we use to find the constrained fiber path is fully automatic and requires approximately 10 minutes per frame in a standard PC (2 GHz processor, 4.00 GB RAM). We pre-compute the geometric models of the spinal canal and then load for real-time visualization and analysis. Parallel computation can significantly reduce the runtime of the optimization method.

In terms of limitations, we did not validate our results against in-vitro data. However, validation of the reconstructed models against in-vitro data would be problematic because the spinal canal deforms significantly when dissected due to the change in loading conditions. Thus, in-vitro validation would lead to inaccurate measurements.

Furthermore, we used a hierarchical model-based motion reconstruction method which has been previously reported to achieve sub-millimeter accuracy for in-vivo cervical spine studies [28]. Using alternative, lower accuracy motion reconstruction methods may affect the quality of the mesh model reconstruction.

In conclusion, we have designed and developed an automatic method to reconstruct the geometric model of the spinal canal from captured images of joints. The method is in-vivo

and non-invasive, and it allows subject-specific dynamic analysis of the spinal canal. The method, for the first time, meets all these key requirements for the modeling and analysis of the spinal canal. Due to the automation of the method, we do not require any manually placed landmark points. The method generates detailed geometrical models and enables comparison between different subjects.

Because the method uses in-vivo data, it can be applied in large scale experiments for validating hypotheses related to spine injuries and diseases. The tool has potential for real clinical scenarios and can also be very useful for biodynamics and orthopedic research.

6.0 CONCLUSION

In this research, we present a dynamic image-based computational approach for in-vivo modeling and analysis of the human spine. The proposed set of tools allows us to reconstruct the soft-tissue models of the spine from in-vivo images and analyze their geometry during motion. The modeling process is semi-automatic for ligaments and inter-vertebral discs and automatic for the spinal canal. We designed anatomically relevant measurements for each soft-tissue model. We also designed normalized measurements that enable inter-subject comparisons.

The proposed soft-tissue modeling tools are based on accurate dynamic motion information and geometry of vertebrae. The dynamic motion information is reconstructed from static volumetric and dynamic X-ray images.

Automation of the spine soft-tissue modeling process is a significant contribution of our research. Existing soft-tissue modeling and analysis techniques are mostly manual, requiring significant user interaction and human labor. The automation of our tools reduces human labor significantly (e.g., for the ligament and the intervertebral disc space) and in some cases (e.g., for the spinal canal), the method is fully automatic. This automation will allow large scale application of the tools.

One of the principal contributions of our soft-tissue modeling methods is capturing the dynamic geometric deformation of the soft-tissue structure of the spine. Existing imaging technologies such as CT or MR do not allow capturing the dynamic 3D structure of the soft-tissue. Our methods avoid this limitation by reconstructing the geometry using dynamic motion information.

In addition to the modeling, we show how to analyze the reconstructed soft-tissue models. For each soft-tissue model, we compute anatomically relevant measurements. Comparison

with existing literature results based on in-vitro studies shows strong agreement, providing a simple validation of our models.

For inter-subject comparison and analysis of the soft-tissue models, we design and compute normalized measurements. These normalized measurements reveal interesting features and patterns that are not directly observable from the absolute measurements. Our soft-tissue models thus enable us to extract interesting geometric features as necessary.

All of our proposed tools are non-invasive. We use dynamic X-ray and CT images, both captured non-invasively. Due to non-invasiveness, the tools have potentials for a real clinical application or a large-scale study. Such applications would improve our understanding of the spine and spine-related diseases.

Automated motion reconstruction of the spine with sub-millimeter accuracy is a significant contribution of our approach. Existing state of the art spine motion reconstruction technique requires extensive expert operator interaction to produce valid and accurate results. Our proposed hierarchical multi-bone model-based method makes the motion reconstruction operator-independent while achieving the same accuracy as the expert operator. Our motion reconstruction method can serve as a very useful tool for the orthopaedic researchers for understanding spine injuries and disorders by examining the vertebrae motion.

Our motion reconstruction and soft-tissue modeling datasets have three subjects and two subjects respectively. To define normal variation, large scale studies are required. The proof of concept shown here based on two or three subjects should not be interpreted as conclusive from a statistical point of view.

Our proposed soft-tissue models can be complementary to the finite element approach. Constructing accurate geometric models for the finite element method is a challenging task. Our automated tools with the accurate geometrical models of the soft-tissues can thus provide the basis for the finite element method and can save significant human labor. The geometrical models have the potential to significantly contribute to 3D printing-based implant design and prototyping.

The lack of a direct validation technique for soft-tissue models is a drawback for in-vivo modeling and analysis. Direct observation of the soft-tissue structure is practically impossible without dissection. However, indirect validation using another imaging modality

is a possibility. For example, the reconstructed soft-tissue models can be validated using in-vivo MR images of the same subject. However, multi-modal image registration, resolution difference between imaging modalities, and different loading conditions and posture between experiments are some significant challenges for the multi-modal in-vivo validation technique.

Our soft-tissue modeling methods may require some anatomic knowledge in the modeling processes e.g., we need ligament insertion sites as input parameters for the ligament modeling. However, these features may vary significantly between subjects and they are practically impossible to determine accurately in-vivo for the spine. Therefore, we depend on human expertise for identifying these anatomic landmarks. However, our methods significantly reduce the required number of manual landmarks compared to the existing modeling techniques, which are mostly manual. The impact of selected landmarks on the generated models can be examined in future studies.

Dependency on the accurate dynamic motion is a limitation of our soft-tissue modeling methods. With inaccurate motion information, the modeling process will generate anatomically inaccurate soft-tissue geometry. Therefore, we emphasize the need of an accurate motion reconstruction method for the soft-tissue modeling. The motion reconstruction method should be validated for the joint of interest prior to applying the soft-tissue modeling method.

In addition to the direct analysis of the soft-tissue models, these models can serve as input to joint simulation techniques such as the FE method or the multibody simulation. These simulation techniques generally use manually-created and simplified soft-tissue models that typically do not represent the anatomical accuracy of the complex soft-tissue geometry. Because of the geometric accuracy and the automation, our soft-tissue modeling tools can contribute significantly to these simulation techniques in their model building process.

Even though we did our experiments on the spine, our proposed tools can be expanded to other joints. In terms of anatomical complexity, the spine is more complex and more difficult to image than many other joints in the human body. Application to other joints may not be trivial if the joint structure has significantly different hierarchy, e.g. the wrist joint. We are looking forward to applying the method to different joints in the future.

The automated motion reconstruction and spine soft-tissue modeling tools have signifi-

cant impact in the orthopaedic research and musculoskeletal modeling and simulation of the joint in biomechanics research. Due to automation and operator independence, the tools have potential for real clinical application. Large-scale studies using these tools can improve our understanding of the spine and spine-related diseases.

7.0 BIBLIOGRAPHY

- [1] (1996). ASTM: Standard Practice for Use of the Terms Precision and Bias in ASTM Test Methods. West Conshohockent, PA.
- [2] Aly, T. and Amin, O. (2013). Geometrical dimensions and morphological study of the lumbar spinal canal in the normal egyptian population. *Orthopedics*, 36(2):e229–34.
- [3] Anderson, F., Delp, S., John, C., Seth, A., and Habib, A. (2010). Opensim user’s guide: Release 2.0.1.
- [4] Anderst, W. (2011). Automated measurement of neural foramen cross-sectional area during in vivo functional movement. *Comput Methods Biomech Biomed Engin.*
- [5] Anderst, W., Zauel, R., Bishop, J., Demps, E., and Tashman, S. (2009). Validation of three-dimensional model-based tibio-femoral tracking during running. *Medical Engineering & Physics*, 31(1):10–16.
- [6] Anderst, W. J., Baillargeon, E., Donaldson, W. F., Lee, J. Y., and Kang, J. D. (2011). Validation of a noninvasive technique to precisely measure in vivo three-dimensional cervical spine movement. *Spine*, 36(6):E393–E400.
- [7] Bah, M., Nair, P., and Browne, M. (2009). Mesh morphing for finite element analysis of implant positioning in cementless total hip replacements. *Med Eng Phys*, 31(10):1235–43.
- [8] Baldwin, M., Langenderfer, J., Rullkoetter, P., and Laz, P. (2010). Development of subject-specific and statistical shape models of the knee using an efficient segmentation and mesh-morphing approach. *Comput Methods Programs Biomed*, 97(3):232–40.

- [9] Banks, S. A. and Hodge, W. A. (1996). Accurate measurement of three-dimensional knee replacement kinematics using single-plane fluoroscopy. *IEEE Trans. Biomed. Eng.*, 43(6):638–649.
- [10] Behnam, A. J., Herzka, D. A., and Sheehan, F. T. (2011). Assessing the accuracy and precision of musculoskeletal motion tracking using cine-pc mri on a 3.0t platform. *Journal of Biomechanics*, 44(1):193–197.
- [11] Bey, M. J., Zauel, R., Brock, S. K., and Tashman, S. (2006). Validation of a new model-based tracking technique for measuring three-dimensional, in vivo glenohumeral joint kinematics. *Journal of Biomechanical Engineering*, 128(4):604–609.
- [12] Brainerd, E. L., Baier, D. B., Gatesy, S. M., Hedrick, T. L., Metzger, K. A., and Crisco, J. J. (2010). X-ray reconstruction of moving morphology (xromm): Precision, accuracy and applications in comparative biomechanics research. *Journal of Experimental Zoology*, 313A(5):262–279.
- [13] Brekelmans, W. A. M., Poort, H. W., and Slooff, T. J. J. H. (1972). A new method to analyse the mechanical behaviour of skeletal parts. *Acta orthop Scandinav*, 43:301–317.
- [14] Brodin, K. and Halldin, P. (2004). Development of a finite element model of the upper cervical spine and a parameter study of ligament characteristics. *Spine*, 29(4):376–385.
- [15] Carrigan, S. D., Whiteside, R. A., Pichora, D. R., and Small, C. F. (2003). Development of a three-dimensional finite element model for carpal load transmission in a static neutral posture. *Annals of Biomedical Engineering*, 31(6):718–725.
- [16] Chang, D., Tencer, A., Ching, R., Treece, B., Senft, D., and Anderson, P. (1994). Geometric changes in the cervical spinal canal during impact. *Spine (Phila Pa 1976)*, 19(8):973–80.
- [17] Chen, B. H., Natarajan, R. N., An, H. S., and Andersson, G. B. (2001). Comparison of biomechanical response to surgical procedures used for cervical radiculopathy: poste-

- rior keyhole foraminotomy versus anterior foraminotomy and discectomy versus anterior discectomy with fusion. *Journal Of Spinal Disorders*, 14(1):17–20.
- [18] Christophy, M., Faruk Senan, N. A., Lotz, J. C., and O'Reilly, O. M. (2011). A musculoskeletal model for the lumbar spine. *Biomechanics and Modeling in Mechanobiology*, 11(1989):19–34.
- [19] Damsgaard, M., Rasmussen, J., Christensen, S., Surma, E., and Dezee, M. (2006). Analysis of musculoskeletal systems in the anybody modeling system. *Simulation Modelling Practice and Theory*, 14(8):1100–1111.
- [20] Delp, S. L., Anderson, F. C., Arnold, A. S., Loan, P., Habib, A., John, C. T., Guendelman, E., and Thelen, D. G. (2007). Opensim: Open-source software to create and analyze dynamic simulations of movement. *IEEE Transactions on Biomedical Engineering*, 54(11):1940–1950.
- [21] El-Rich, M., Shirazi-Adl, A., and Arjmand, N. (2004). Muscle activity, internal loads, and stability of the human spine in standing postures: combined model and in vivo studies. *Spine*, 29(23):2633–2642.
- [22] Erleben, K., Sporring, J., Henriksen, K., and Dohlman, K. (2005). *Physics-based Animation (Graphics Series)*. Charles River Media, Inc., Rockland, MA, USA.
- [23] Fang, D., Cheung, K., Ruan, D., and Chan, F. (1994). Computed tomographic osteometry of the asian lumbar spine. *J Spinal Disord*, 7(4):307–16.
- [24] Gardiner, J. C. and Weiss, J. A. (2003). Subject-specific finite element analysis of the human medial collateral ligament during valgus knee loading. *Journal of Orthopaedic Research*, 21(6):1098–1106.
- [25] Gattton, M. L., Percy, M. J., and Pettet, G. J. (2011). Computational model of the lumbar spine musculature: implications of spinal surgery. *Clinical Biomechanics*, 26(2):116–122.

- [26] Gilad, I. and Nissan, M. (1985). Sagittal radiographic measurements of the cervical and lumbar vertebrae in normal adults. *Br J Radiol*, 58(695):1031–4.
- [27] Haque, A., Anderst, W., Tashman, S., and Marai, G. (2012). Validation of a non-invasive automated hierarchical method to precisely measure lumbar spine movement. *2012 Annual Meeting of the Orthopaedic Research Society*.
- [28] Haque, M., Anderst, W., Tashman, S., and Marai, G. E. (2013). Hierarchical model-based tracking of cervical vertebrae from dynamic biplane radiographs. *Medical Engineering & Physics*, 35(7):994–1004.
- [29] Heimann, T., Chung, F., Lamecker, H., and Delingette, H. (2009). Subject-specific ligament models: Towards real-time simulation of the knee joint. pages 107–119. Asclepios Project, INRIA, Sophia Antipolis, France.
- [30] Heller, J. G., Sasso, R. C., Papadopoulos, S. M., Anderson, P. A., Fessler, R. G., Hacker, R. J., Coric, D., Cauthen, J. C., and Riew, D. K. (2009). Comparison of bryan cervical disc arthroplasty with anterior cervical decompression and fusion: clinical and radiographic results of a randomized, controlled, clinical trial. *Spine*, 34(2):101–107.
- [31] Hilibrand, A., Carlson, G., Palumbo, M., Jones, P., and Bohlman, H. (1999). Radiculopathy and myelopathy at segments adjacent to the site of a previous anterior cervical arthrodesis. *J Bone Joint Surg Am*, 81(4):519–28.
- [32] Hill, A. V., Series, L., and Sciences, B. (1938). The heat of shortening and the dynamic constants of muscle the heat of shortening and the dynamic constants of niucle. *Society*, 126(843):136–195.
- [33] Holden, J. P., Orsini, J. A., Siegel, K. L., Kepple, T. M., Gerber, L. H., and Stanhope, S. J. (1997). Surface movement errors in shank kinematics and knee kinetics during gait. *Gait & Posture*, 5(3):217–227.
- [34] Kurtz, S. and Edidin, A. (2006). *Spine Technology Handbook*. Biomedical engineering. Elsevier Science & Technology Books.

- [35] Kwak, S. D., Blankevoort, L., and Ateshian, G. A. (2000). A mathematical formulation for 3d quasi-static multibody models of diarthrodial joints. *Comput Methods Biomech Biomed Engin*, 3(1):41–64.
- [36] Lambrecht, J. M., Audu, M. L., Triolo, R. J., and Kirsch, R. F. (2009). Musculoskeletal model of trunk and hips for development of seated-posture-control neuroprosthesis. *Journal of rehabilitation research and development*, 46(4):515–528.
- [37] Langrana, N. A., Harten RD, R. D., Lin, D. C., Reiter, M. F., and Lee, C. K. (2002). Acute thoracolumbar burst fractures: a new view of loading mechanisms. *Spine*, 27(5):498–508.
- [38] Li, G., Van De Velde, S. K., and Bingham, J. T. (2008). Validation of a non-invasive fluoroscopic imaging technique for the measurement of dynamic knee joint motion. *Journal of Biomechanics*, 41(7):1616–1622.
- [39] Li, Z., Tang, J., Chakan, M., and Kaz, R. (2009). Carpal tunnel expansion by palmarly directed forces to the transverse carpal ligament. *Journal of biomechanical Engineering*, 131(8):1–18.
- [40] Liu, Y. K., Ray, G., and LAB, T. U. N. O. L. B. (1973). A finite element analysis of wave propagation in human spine.
- [41] Lorensen, W. E. and Cline, H. E. (1987). Marching cubes: A high resolution 3d surface construction algorithm. *Computer*, 21(4):163–169.
- [42] Lu, J., Ebraheim, N. a., Yang, H., Rollins, J., and Yeasting, R. a. (1999). Anatomic bases for anterior spinal surgery: surgical anatomy of the cervical vertebral body and disc space. *Surgical and radiologic anatomy : SRA*, 21(4):235–9.
- [43] Lu, T. W. and O’Connor, J. J. (1999). Bone position estimation from skin marker coordinates using global optimization with joint constraints. *Journal of Biomechanics*, 32:129–134.

- [44] Mahfouz, M. R., Hoff, W. A., Komistek, R. D., and Dennis, D. A. (2003). A robust method for registration of three-dimensional knee implant models to two-dimensional fluoroscopy images. *IEEE Trans. Med. Imag.*, 22(12):1561–1574.
- [45] Malghem, J., Willems, X., Vande Berg, B., Robert, A., Cosnard, G., and Lecouvet, F. (2009). Comparison of lumbar spinal canal measurements on mri and ct. *J Radiol*, 90(4):493–7.
- [46] Marai, G. E. (2007). *Data-Driven Predictive Modeling of Diarthrodial Joints*. PhD thesis, Brown University.
- [47] Marai, G. E., Laidlaw, D. H., and Crisco, J. J. (2006). Super-resolution registration using tissue-classified distance fields. *IEEE Trans. Med. Imag.*, 25(2):177–187.
- [48] Mauch, S. (2000). A fast algorithm for computing the closest point and distance transform. *SIAM J Sci Comput submitted*, pages 1–17.
- [49] McDonald, C. P., Bachison, C. C., Chang, V., Bartol, S. W., and Bey, M. J. (2010). Three-dimensional dynamic in vivo motion of the cervical spine: assessment of measurement accuracy and preliminary findings. *The spine journal official journal of the North American Spine Society*, 10(6):497–504.
- [50] Mciff, T. B. R. A. (2008). Preliminary validation of mri-based modeling for evaluation of joint mechanics. *Journal of Musculoskeletal Research*, 11(4):161–171.
- [51] Muggleton, J. M. and Allen, R. (1997). Automatic location of vertebrae in digitized videofluoroscopic images of the lumbar spine. *Medical Engineering & Physics*, 19(1):77–89.
- [52] Muller, M., Teschner, M., and Gross, M. Physically-based simulation of objects represented by surface meshes. *Proceedings Computer Graphics International 2004*, 2004(6236):26–33.
- [53] Nealen, A., Mller, M., Keiser, R., Boxerman, E., and Carlson, M. (2006). Physically based deformable models in computer graphics. *Computer Graphics Forum*, 25(4):809–836.

- [54] Nesme, M., Kry, P. G., Jer(bkov, L., and Faure, F. (2009). Preserving topology and elasticity for embedded deformable models. *ACM Transactions on Graphics*, 28(3):1.
- [55] of Orthopaedic Surgeons, A. A. (2008). *Burden of Musculoskeletal Diseases in the United States: Prevalence, Societal and Economic Cost*. American Academy of Orthopaedic Surgeons.
- [56] Panjabi, M., Goel, V., Oxland, T., Takata, K., Duranceau, J., Krag, M., and Price, M. (1992). Human lumbar vertebrae. quantitative three-dimensional anatomy. *Spine (Phila Pa 1976)*, 17(3):299–306.
- [57] Pauly, M., Pai, D. K., and Guibas, L. J. (2004). Quasi-rigid objects in contact. *Proceedings of the 2004 ACM SIGGRAPH Eurographics symposium on Computer animation SCA 04*, page 109.
- [58] Przybylski, G., Patel, P., Carlin, G., and Woo, S. (1998). Quantitative anthropometry of the subatlantal cervical longitudinal ligaments. *Spine*, 23(8):893–8.
- [59] Rohlmann, A., Zander, T., and Bergmann, G. (2005). Comparison of the biomechanical effects of posterior and anterior spine-stabilizing implants. *European spine journal*, 14(5):445–453.
- [60] Russakoff, D. B., Rohlfing, T., Ho, A., Kim, D. H., Shahidi, R., Adler, J. R., and Maurer, C. R. (2003). Evaluation of intensity-based 2d-3d spine image registration using clinical gold-standard data. *Image Registration*, pages 151–160.
- [61] Seifert, S., Wachter, I., Schmelzle, G., and Dillmann, R. (2009). A knowledge-based approach to soft tissue reconstruction of the cervical spine. *IEEE Transactions on Medical Imaging*, 28(4):494–507.
- [62] Seisler, A. R. and Sheehan, F. T. (2007). Normative three-dimensional patellofemoral and tibiofemoral kinematics: a dynamic, in vivo study. *IEEE Trans. Biomed. Eng.*, 54(7):1333–1341.

- [63] Sherman, M. A., Seth, A., and Delp, S. L. (2011). Simbody: multibody dynamics for biomedical research. *Procedia IUTAM*, 2:241–261.
- [64] Shirazi-Adl, A., El-Rich, M., Pop, D. G., and Parnianpour, M. (2005). Spinal muscle forces, internal loads and stability in standing under various postures and loads—application of kinematics-based algorithm. *European spine journal*, 14(4):381–392.
- [65] Sigal, I., Hardisty, M., and Whyne, C. (2008). Mesh-morphing algorithms for specimen-specific finite element modeling. *J Biomech*, 41(7):1381–9.
- [66] Sigal, I., Yang, H., Roberts, M., and Downs, J. (2010). Morphing methods to parameterize specimen-specific finite element model geometries. *J Biomech*, 43(2):254–62.
- [67] Stokes, I. A. F. and Gardner-Morse, M. (1995). Lumbar spine maximum efforts and muscle recruitment patterns predicted by a model with multijoint muscles and joints with stiffness. *Journal of Biomechanics*, 28(2):173–186.
- [68] Teo, E. C. and Ng, H. W. (2001). First cervical vertebra (atlas) fracture mechanism studies using finite element method. *Journal of Biomechanics*, 34(1):13–21.
- [69] Teyhen, D. S., Flynn, T. W., Bovik, A. C., and Abraham, L. D. (2005). A new technique for digital fluoroscopic video assessment of sagittal plane lumbar spine motion. *Spine*, 30(14):E406–E413.
- [70] The Numerical Algorithms Group (NAG), Oxford, U. K. The nag c library (2013). <http://www.nag.co.uk/numeric/fl/manual/pdf/E04/e04ccf.pdf>.
- [71] Thelen, D. G. (2003). Adjustment of muscle mechanics model parameters to simulate dynamic contractions in older adults. *Journal of Biomechanical Engineering*, 125(1):70.
- [72] Tierney, R., Maldjian, C., Mattacola, C., Straub, S., and Sitler, M. (2002). Cervical spine stenosis measures in normal subjects. *J Athl Train*, 37(2):190–193.
- [73] Tomazevic, D., Likar, B., Slivnik, T., and Pernus, F. (2003). 3-d/2-d registration of ct and mr to x-ray images. *IEEE Trans. Med. Imag.*, 22(11):1407–16.

- [74] Un, K. and Spilker, R. L. (2006). A penetration-based finite element method for hyperelastic 3d biphasic tissues in contact. part ii: finite element simulations. *Journal of Biomechanical Engineering*, 128(6):934–942.
- [75] Weiss, J. A., Gardiner, J. C., Ellis, B. J., Lujan, T. J., and Phatak, N. S. (2005). Three-dimensional finite element modeling of ligaments: technical aspects. *Medical Engineering & Physics*, 27(10):845–861.
- [76] Yoganandan, N., Kumaresan, S., and Pintar, F. A. (2001). Biomechanics of the cervical spine part 2. cervical spine soft tissue responses and biomechanical modeling. *Clinical Biomechanics*, 16(1):1–27.
- [77] Zajac, F. E. (1989). Muscle and tendon: properties, models, scaling, and application to biomechanics and motor control. *Critical Reviews in Biomedical Engineering*, 17(4):359–411.
- [78] Zee, M. d., Hansen, L., Wong, C., Rasmussen, J., and Simonsen, E. B. (2007). A generic detailed rigid-body lumbar spine model. *Journal of Biomechanics*, 40(6):1219–1227.